Multi-phase flow through complex geometry caused by fire involving radioactive materials

Dissertation
zur Erlangung des akademischen Grades

Doktoringenieur
(Dr.-Ing.)

von Michael Plagge, M.Sc.

geb. am 01. Februar 1984 in Hannover

genehmigt durch die Fakultät für Verfahrens- und Systemtechnik
der Otto-von-Guericke-Universität Magdeburg

Promotionskomission:	JProf. Dr.-Ing. Benoît Fond (Vorsitz) Prof. Dr.-Ing. habil. Ulrich Krause (Gutachter) Prof. Dr. Enrico Da Riva (Gutachter) Prof. Dr. rer. nat. Christoph Schäfer (Gutachter)
eingereicht am:	12. Mai 2017
Promotionskolloqium am:	10. November 2017

Kurzreferat

Seit 1954 entwirft, baut und unterhält die Europäische Organisation für Kernforschung (CERN) Teilchenbeschleuniger und Experimente für verschiedene Grundlagen- und Anwendungsforschung. Ein Großteil der Teilchenbeschleuniger- und Teilchendetektorinstallationen entfällt dabei auf einzigartige Anlagen, welche in unterirdischen Kavernen und Tunnel untergebracht sind. Innerhalb dieser Anlagen entsteht während des Betriebes ionisierende Strahlung, beispielweise durch Teilchenkollisionen, Teilchenstrahlverluste in Bauteilen oder durch physikalische Phänomene wie die Synchrotronstrahlung.

Um die Auswirkungen eines Schadenfeuers in einer untertägigen Anlage in Gegenwart radioaktiven, brennbaren Materials besser beurteilen zu können, wird in dieser Arbeit eine neue, vereinfachte Berechnungsmethode für brandinduzierte Aerosolfreisetzung und -kontamination vorgestellt. Dazu werden bestehendes Fachwissen und bereits vorhandene Hilfsmittel neu verknüpft, um das Schadensausmaß eines solchen Ereignisses besser abschätzen zu können.

Als repräsentative Anlage wird die Experimentalkaverne des Compact Muon Solenoid Experimentes am großen Hadronen-Teilchenbeschleuniger des CERN untersucht. Kaverne und der zugehörige Zugangsschaft umfassen dabei jeweils ein Volumen von etwa $25.000\,\mathrm{m}^3$. Ausgehend vom existierenden Brandschutzkonzept werden weitere Brandszenarien erarbeitet und mittels numerischer Strömungsmechanik berechnet. Eine modifizierte Version des fireFoam Lösers von FM Global zusammen mit der OpenFOAM Programmbibliothek wird hierbei für die Modellierung verwendet. Lagrangsche Partikel ermöglichen die Charakterisierung des Aerosoltransportes. Zur Erzeugung der zugrundeliegenden Auftriebsströmung wird ein einfacher Diffusionsbrenner modeliert. Basierend auf individuellen Testfällen für jede verwendete Teilroutine der Anwendung wird eine Verifizierungsstudie durchgeführt. Die resultierende Fehlermatrix wird zusammen mit den Ergebnissen diskutiert.

Mittels der vorgestellten Methodik kann der auftriebsinduzierte Aerosoltransport von einer untertägigen Anlage zur Erdoberfläche durch den Zugangsschacht bestimmt werden. Die im Rahmen dieser Arbeit vorgestellten fundierten oberen Freisetzungswerte sind dabei weniger konservativ als die vorheriger Studien. Des Weiteren werden Aufenthaltswahrscheinlichkeiten für Aerosole verschiedener Durchmesser auf Oberflächen ermittelt. Diese ermöglichen eine erste Abschätzung einer Kontamination im Brandfall. Sowohl die Ergebnisse der Aerosolfreisetzung als auch die Resultate der Aerosoloberflächenkontaminierung werden für weitere Analysen durch die Strahlenschutzgruppe des CERN verwendet. Die Ergebnisse können jedoch auch für alle weiteren Risikoanalysen herangezogen werden, die auf Aerosolausbreitung beruhen.

Abstract

Since 1954 the European Organization for Nuclear Research (CERN) designs, constructs and maintains particle accelerators and experiments for a broad variety of fundamental research topics and applications. A large part is made up of unique underground installations, mainly caverns and tunnels, housing accelerator and particle detector infrastructure. Ionizing radiation occurs in this premises by design, e.g. due to particle collisions, losses of particle beams to the present material or physical phenomena such as synchrotron radiation.

The present thesis covers a new approach in fire safety engineering in order to provide a better understanding of the environmental impact of a fire incident in a subterranean facility involving combustible materials with radioactive nuclides. Existing knowledge and principles are merged to provide a universal tool facilitating estimations on aerosol release and deposition due to the usual emerging thermal plume and flows originating from a fire.

An exemplary complex large-scale geometry was chosen: the Compact Muon Solenoid experimental cavern at CERN's Large Hadron Collider, featuring a cavern of about 25,000 m^3 with an access shaft of equal volume. Taking into account the present state of fire safety, adequate fire scenarios have been developed. Computational fluid dynamics calculations have been carried out with a modified version of FM Global's fireFoam solver and the OpenFOAM toolbox, contributing a Lagrangian particle framework to represent differently sized aerosols carried along a plume-induced flow originating from a simple diffusion burner. A model verification study is discussed in detail. It uses individual test cases for each chosen sub model of the code and provides a relative error matrix.

Compared to earlier assessments, a more reliable upper limit for aerosol release due to a fire-driven flow from the underground installations towards the surface could be obtained. Further, residence probabilities for each aerodynamic particle diameter and individually defined surface allow a better estimation of aerosol deposition in case of fire. Release percentages and deposition probabilities are used for further assessments by CERN's radiation protection group, i.e. for dose rate estimations or contamination assessments. Aerosol results are universal and thus can be used for any other risk analysis involving dispersion and spread of aerosols.

Résumé

Depuis 1954 l'organisation européenne pour la recherche nucléaire (CERN) développe, construit et entretient des accélérateurs et des expériences de particules. L'ensemble est utilisé pour la recherche fondamentale et appliquée. Une grande partie des installations se trouve en souterrain. En particulier les accélérateurs et les détecteurs de particules sont basés dans plusieurs tunnels et grandes cavernes. Dedans le rayonnement ionisant est produit en raison des collisions de particules, des pertes des faisceaux des particules ou en raison des phénomènes physiques comme le rayonnement synchrotron.

Cette thèse couvre une nouvelle méthode de l'ingénierie incendie pour améliorer l'évaluation d'impact environnemental d'un feu dans les installations sous-sol qui se déroule dans la présence du matériel radioactif. L'état et formules existant sont réassocié pour créer un outil plus adapté au calcul de rejet et de contamination d'aérosol en cas de feu.

La caverne expérimentale de l'expérience Solénoïde (CMS) compact pour muons est choisie comme exemple, qui fait partie du grand collisionneur de hadrons au CERN. Il s'agit d'un volume d'environ 25,000 m^3, avec un puit d'accès qui se présente avec un volume équivalent. En suivant le concept de protection incendie initial, quelques scénarios sont créés en plus. Pour en calculer, le logiciel fireFoam de l'entreprise FM Global est utilisé en combinaison avec OpenFOAM, une caisse à outils du domaine de calculs tridimensionnel. Elle offre une partie dédie aux particules Lagrange qui est utilisée avec un modèle d'un brûleur à diffusion simple. Chaque sous-programme est vérifié par un test adapté. Les vérifications résultent dans une matrice d'erreurs qui est associé aux réxsultats.

La nouvelle méthode proposée offre des résultats plus réaliste concernant un rejet d'aérosols en cas du feu en comparaison avec des rapports anciens. Puis elle met à disposition des probabilités de présence sur une ou plusieurs surfaces en fonction de diamètres des particules calculée. Les valeurs permettent une évaluation du rejet et de la contamination causée par un incendie. Ils sont utilisés pour autre analyse de risque fait par le groupe de la radioprotection du CERN. Par contre, les résultats sont aussi exploitable dans une manière interdisciplinaire pour chaque sujet qui touche le transport et la dispersion d'aérosols.

Schriftliche Erklärung

Ich erkläre hiermit, dass ich die vorliegende Arbeit ohne unzulässige Hilfe Dritter und ohne Benutzung anderer als der angegebenen Hilfsmittel angefertigt habe. Die aus fremden Quellen direkt oder indirekt übernommenen Gedanken sind als solche kenntlich gemacht.

Insbesondere habe ich nicht die Hilfe einer kommerziellen Promotionsberatung in Anspruch genommen. Dritte haben von mir weder unmittelbar noch mittelbar geldwerte Leistungen für Arbeiten erhalten, die im Zusammenhang mit dem Inhalt der vorgelegten Dissertation stehen.

Die Arbeit wurde bisher weder im Inland noch im Ausland in gleicher oder ähnlicher Form als Dissertation eingereicht und ist als Ganzes auch noch nicht veröffentlicht.

Magdeburg, den 12. Mai 2017

Michael Plagge

Publication acknowledgments

A part of this thesis work has been published in the following journals and proceedings:

Michael Plagge, Ulrich Krause and Christoph Schäfer. CFD Calculations of Design Fire Scenarios for Experimental Underground Installations at CERN. In *3. Magdeburger Brand- und Explosionsschutztag / 2. vfdb Workshop Brandschutzforschung*, March 2013.

Michael Plagge, Ulrich Krause, Enrico Da Riva, Christoph Schäfer and Doris Forkel-Wirth (2017). An Alternative Method for Thermal Plume–Induced Aerosol Release and Deposition Calculations in Large Geometries Using fireFoam. *Nuclear Technology*, 198:1, 43-52, http://dx.doi.org/10.1080/00295450.2017.1291227

This work was supported with a three-year scholarship at the European Organization for Nuclear Research (CERN), funded by the Wolfgang-Gentner-Programme of the Federal Ministry of Education and Research (BMBF) of the Federal Republic of Germany.

Contents

1 Introduction **1**
- 1.1 CERN, the LHC and CMS . . . 2
- 1.2 Motivation . . . 5

2 Fire risk analysis and fire scenarios **7**
- 2.1 Initial concept . . . 7
  - 2.1.1 Civil engineering . . . 7
  - 2.1.2 Fire prevention . . . 9
  - 2.1.3 Fire protection systems . . . 10
  - 2.1.4 Fire brigade intervention procedures . . . 13
  - 2.1.5 Means of escape . . . 13
- 2.2 New fire Scenarios . . . 14
  - 2.2.1 Smoldering cable fire . . . 15
  - 2.2.2 Electrical cabinet fire . . . 17
  - 2.2.3 Mobile elevated work platform fire . . . 20
- 2.3 Conclusions and recommendations . . . 21

3 Fire modeling with fireFoam **23**
- 3.1 State of the art . . . 23
- 3.2 Goals and objectives . . . 24
- 3.3 Model setup . . . 25
  - 3.3.1 Simplified geometry and meshing . . . 27
  - 3.3.2 Combustion sub model . . . 30
  - 3.3.3 Lagrangian sub model . . . 31
  - 3.3.4 Thermal radiation sub model . . . 34
  - 3.3.5 Turbulence sub model . . . 37
  - 3.3.6 Initial and boundary conditions . . . 38
  - 3.3.7 Numerical solver choices . . . 39

4 Verification and Validation **41**
- 4.1 Mesh independence . . . 42
- 4.2 Compliance of initial and boundary conditions . . . 46
- 4.3 Combustion sub model . . . 48
- 4.4 Lagrangian parcel sub model . . . 53
- 4.5 Thermal radiation sub model . . . 54
- 4.6 Verification matrix and conclusions . . . 56

5 Results and discussion **58**
5.1 Fire-induced flow results for the CMS experimental cavern 58
5.1.1 Closed cavern - air management system use 58
5.1.2 Open access shaft 63
5.1.3 Open access shaft and connection to neighboring service cavern . 65
5.2 Fire-induced aerosol results for the CMS experimental cavern 70
5.2.1 Local interaction unlimited rebound sub model 71
5.2.2 Local interaction limited rebound sub model 87
5.2.3 Local interaction sub model 99
5.2.4 Comparison of interaction sub model configurations in terms of release 100

6 Conclusions and further investigations **105**

A Tables **119**

B Mathematical model **140**
B.1 Conservation of mass 141
B.2 Conservation of momentum 141
B.3 Conservation of energy 142
B.4 Transport of species 142
B.5 Turbulence sub models 142
B.5.1 One-Equation-Eddy-Dissipation-Model 143
B.6 Combustion sub models 144
B.6.1 Infinite fast chemistry 146
B.7 Thermal radiation sub models 146
B.7.1 fvDOM 147
B.7.2 P1 148
B.7.3 Absorption emission models 149
B.8 Lagrangian parcel sub model 150
B.9 Equations of state 151
B.9.1 Transport coefficients 152
B.10 Initial and boundary conditions 153
B.10.1 Pressure and Velocity 154
B.10.2 Temperature 157
B.10.3 Concentrations of chemical reactants and products 158
B.10.4 Turbulent kinetic energy, viscosity and diffusivity 158
B.10.5 Incident radiation and radiative intensity 159

List of Figures

1.1 Overview of CERN's particle accelerator complex. 3
1.2 Compact Muon Solenoid Experiment in exploded view. 4
1.3 Schematic representation of a worst case fire scenario with respect to radiation protection. 5

2.1 Overview of the underground installations at access point 5 of the LHC particle accelerator. 8
2.2 Labeled drawing of the CMS Experiment and its inner detector. 12
2.3 Example event tree for a smoldering fire scenario in a CERN facility. . . 15
2.4 Example cable tray in UXC55. 16
2.5 Forward calorimeter part of the CMS detector. 19
2.6 Mobile elevated work platform on rubber wheels. 20

3.1 STL geometry of the CMS experimental cavern, access shaft and detector without and with air management system. 28
3.2 Detailed view of the joint between the round shaped cavern ceiling and round shaped access shaft. 29
3.3 Longitudinal cross-section of the used computational grid. 30
3.4 Sketch of a thermal plume including Lagrangian particle injection cone. . 32
3.5 Visualization of ideal spherical diffusion by thermal radiation originating from a modeled diffusion burner. 35
3.6 Plots of mean temperature without and with the fvDOM thermal radiation sub model. 36
3.7 Distribution of streamlines caused by fire-induced buoyant flow inside the experimental cavern part. 38

4.1 Visualization of 2D sub mesh used for mesh independence testing. 42
4.2 Time-averaged mean velocity magnitude plots for 5, 10 and 20 cm uniform cell size. 44
4.3 Mean velocity magnitude versus coordinate component at $y = 6.325\,\mathrm{m}$ and $z = 4.0975\,\mathrm{m}$. 45
4.4 Cavern geometry with pressure relief box. 47
4.5 Mass inflow versus time t through an outflow-only defined surface. 48
4.6 Plume equation test mesh with 31 sampling points. 50
4.7 Comparison plot between computed and equation derived plume velocities for differently sized plume region cells using a convective HRR of 1 MW. 51

4.8 Comparison plot between computed and equation derived plume temperatures for differently sized plume region cells using a convective HRR of 1 MW. 52
4.9 Influence of time step size on particle spray cones in ideal conditions. . . 55
4.10 Thermal radiative heat flux as a function of uniform mesh size and total number of solid angles. 56

5.1 Instantaneous temperature contours inside the closed experimental cavern volume. 59
5.2 Instantaneous velocity magnitude contours inside the closed experimental cavern volume. 60
5.3 Instantaneous temperature contours inside the closed experimental cavern volume modeling low and medium extraction mode of the air management system. 61
5.4 Instantaneous velocity magnitude contours inside the closed experimental cavern volume modeling low and medium extraction mode of the air management system. 62
5.5 Instantaneous temperature and velocity magnitude contours inside the closed cavern volume (1.5 MW, 28 min; without air management system). 63
5.6 Instantaneous temperature contours for the cavern volume open towards the surface level (1 MW, 20 min and 1.5 MW, 14 min). 64
5.7 Instantaneous velocity magnitude contours for the cavern volume open towards the surface level (1 MW, 20 min and 1.5 MW, 14 min). 65
5.8 Instantaneous temperature contours for the cavern volume open towards the surface level and the neighboring cavern (1 MW, 20 min and 1.5 MW, 14 min). 66
5.9 Instantaneous velocity magnitude contours for the cavern volume open towards the surface level and the neighboring cavern. 67
5.10 Velocity fields inside the experimental cavern volume for two different fire positions. 68
5.11 Instantaneous temperature and velocity magnitude contours for the cavern volume open to the surface level and the neighboring cavern (0.5 MW, 40 min). 69
5.12 Illustration of the different patch groups: Floor, cavern -, cavern +, detector, and cavern ceiling. 71
5.13 Overview on 1, 10 and 100 μm particles having hit no, one or multiple patches (1.5 MW, 14 min, cavern open to the surface level, unlimited rebounds). 72
5.14 Percentages of total patch hits (1.5 MW, 14 min, cavern open to the surface level, unlimited rebounds). 73
5.15 Percentages of single and multiple patch hits (1.5 MW, 14 min, cavern open to the surface level, unlimited rebounds). 74

5.16 Percentages of 1, 10 and 100 μm particles hitting exactly two different patches (1.5 MW, 14 min, cavern open to the surface level, unlimited rebounds). 76
5.17 Percentages of 1, 10 and 100 μm particles hitting exactly three different patches (1.5 MW, 14 min, cavern open to the surface level, unlimited rebounds). 77
5.18 Overview on 1 and 10 μm particles having hit no, one or multiple patches (1.5 MW, 24 min, cavern open to the surface level, unlimited rebounds). . 79
5.19 Percentages of single and multiple patch hits (1.5 MW, 24 min, cavern open to the surface level, unlimited rebounds). 80
5.20 Percentages of total patch hits (1.5 MW, 24 min, cavern open to the surface level, unlimited rebounds). 81
5.21 Percentages of 1 and 10 μm particles hitting exactly two different patches (1.5 MW, 24 min, cavern open to the surface level, unlimited rebounds). . 82
5.22 Percentages of 1 and 10 μm particles hitting exactly three different patches (1.5 MW, 24 min, cavern open to the surface level, unlimited rebounds). . 83
5.23 Number of particles versus number of rebounds n_{reb} (1.5 MW, 24 min, cavern open to the surface level, unlimited rebounds). 85
5.24 Instantaneous velocity y-component contours inside the experimental cavern volume 86
5.25 Settling of a 10 μm particle inside the access shaft, expressed as change of its y-coordinate over time. 87
5.26 Overview on 1, 10 and 100 μm particles having hit no, one or multiple patches after (1.5 MW, 24 min, cavern open to surface level, $n_{\mathrm{reb}} = 100$). . 88
5.27 Percentages of single and multiple patch hits (1.5 MW, 24 min, cavern open to the surface level, $n_{\mathrm{reb}} = 100$). 89
5.28 Percentages of total patch hits (1.5 MW, 24 min, cavern open to the surface level, $n_{\mathrm{reb}} = 100$). 90
5.29 Percentages of 1, 10 and 100 μm particles hitting exactly two different patches (1.5 MW, 24 min, cavern open to surface level, $n_{\mathrm{reb}} = 100$). 91
5.30 Overview on 1, 10 and 100 μm particles having hit no, one or multiple patches (1.5 MW, 24 min, cavern open to the surface level, $n_{\mathrm{reb}} = 10,000$). 92
5.31 Percentages of single and multiple patch hits (1.5 MW, 24 min, cavern open to the surface level, $n_{\mathrm{reb}} = 10,000$). 93
5.32 Percentages of total patch hits (1.5 MW, 24 min, cavern open to the surface level, $n_{\mathrm{reb}} = 10,000$). 94
5.33 Percentages of 1, 10 and 100 μm particles hitting exactly two different patches (1.5 MW, 24 min, cavern open to the surface level, $n_{\mathrm{reb}} = 10,000$). 95
5.34 Percentages of 1, 10 and 100 μm particles hitting exactly three different patches (1.5 MW, 24 min, cavern open to the surface level, $n_{\mathrm{reb}} = 10,000$). 96

5.35 Particle release percentages over time for cavern geometry open to the surface using different particle surface interaction models (1.5 MW, 24 minutes). 103
5.36 Particle release percentages over time for cavern geometry open to the surface and neighboring cavern using different particle surface interaction models (1.5 MW, 24 minutes). 104

List of Tables

A.1 Inner dimensions of the underground experimental cavern UXC55. 119
A.2 Comparison of literature data on open electrical cabinet fires. 119
A.3 Derived fire load values for electrical cabinets based on literature data. . 119
A.4 Relative error values for 5 and 10 cm uniform grid sizes. 120
A.5 Relative error values for 10 and 20 cm uniform grid sizes. 120
A.6 Influence of mesh size on particle positions. 120
A.7 Thermal radiation heat flux depending on number of solid angles and uniform mesh size obtained by the fvDOM sub model. 121
A.8 Pressure, turbulent kinetic energy and velocity iteration data for 5, 10 and 20 cm uniform grid sizes. 121
A.9 Mean and maximum Courant number for 5, 10 and 20 cm uniform grid sizes. 121
A.10 Numerical schemes. 122
A.11 Numerical solvers. 122
A.12 Verification matrix. 122
A.13 Patch counts for UXC case open to the surface level, 1.5 MW, 14 minutes, unlimited rebounds. 123
A.14 Total patch hit values for UXC case open to the surface level, 1.5 MW, 14 minutes, unlimited rebounds. 123
A.15 Patch counts for UXC case open to the surface level, 1.5 MW, 24 minutes, unlimited rebounds. 124
A.16 Total patch hit values for UXC case open to the surface level, 1.5 MW, 24 minutes, unlimited rebounds. 124
A.17 Patch counts for UXC case open to the surface level, 1.5 MW, 24 minutes, rebounds limited to 100. 125
A.18 Total patch hit values for UXC case open to the surface level, 1.5 MW, 24 minutes, rebounds limited to 100. 125
A.19 Patch counts for UXC case open to the surface level, 1.5 MW, 24 minutes, rebounds limited to 10,000. 126
A.20 Total patch hit values for UXC case open to the surface level, 1.5 MW, 24 minutes, rebounds limited to 10,000. 126
A.21 Release percentages for closed UXC case, 1 MW, 31 minutes, rebounds limited to 100. 127
A.22 Deposition percentages for closed UXC case, 1 MW, 31 minutes, rebounds limited to 100. 127

A.23 Release percentages for closed UXC case, 1.5 MW, 24 minutes, rebounds limited to 100. 127
A.24 Deposition percentages for closed UXC case, 1.5 MW, 24 minutes, rebounds limited to 100. 128
A.25 Release percentages for closed UXC case, 1.5 MW, 24 minutes, rebounds limited to 100, low extraction mode. 128
A.26 Deposition percentages for closed UXC case, 1.5 MW, 24 minutes, rebounds limited to 100, low extraction mode. 128
A.27 Release percentages for closed UXC case, 1.5 MW, 24 minutes, rebounds limited to 100, medium extraction mode. 129
A.28 Deposition percentages for closed UXC case, 1.5 MW, 24 minutes, rebounds limited to 100, medium extraction mode. 129
A.29 Release percentages for closed UXC case, 1.5 MW, 37.5 minutes, rebounds limited to 100. 129
A.30 Deposition percentages for closed UXC case, 1.5 MW, 37.5 minutes, rebounds limited to 100. 130
A.31 Release percentages for UXC case open to the surface level, 1 MW, 31 minutes, rebounds limited to 100. 130
A.32 Deposition percentages for UXC case open to the surface level, 1 MW, 31 minutes, rebounds limited to 100. 130
A.33 Release percentages for UXC case open to the surface level, 1.5 MW, 24 minutes, rebounds limited to 100. 131
A.34 Deposition percentages for UXC case open to the surface level, 1.5 MW, 24 minutes, rebounds limited to 100. 131
A.35 Release percentages for cavern case open to the surface level and neighboring cavern, 1 MW, 31 minutes, rebounds limited to 100. 131
A.36 Deposition percentages for UXC case open to the surface level and neighboring cavern, 1 MW, 31 minutes, rebounds limited to 100. 132
A.37 Release percentages for cavern case open to the surface level and neighboring cavern, 1.5 MW, 24 minutes, rebounds limited to 100. 132
A.38 Deposition percentages for UXC case open to the surface level and neighboring cavern, 1.5 MW, 24 minutes, rebounds limited to 100. 132
A.39 Release percentages for cavern case open to the surface level and neighboring cavern, 0.5 MW, 40 minutes, rebounds limited to 100. 133
A.40 Deposition percentages for UXC case open to the surface level and neighboring cavern, 0.5 MW, 40 minutes, rebounds limited to 100. 133
A.41 Release percentages for UXC case open to the surface level, 1.5 MW, 24 minutes, rebounds limited to 100, 50,000 particles. 133
A.42 Deposition percentages for UXC case open to the surface level, 1.5 MW, 24 minutes, rebounds limited to 100, 50,000 particles. 134
A.43 Release percentages for UXC case open to the surface level, 1.5 MW, 24 minutes, rebounds limited to 100, 100,000 particles. 134

A.44 Deposition percentages for UXC case open to the surface level, 1.5 MW, 24 minutes, rebounds limited to 100, 100,000 particles. 134
A.45 Release percentages for UXC case open to the surface level and neighboring cavern, 1.5 MW, 24 minutes, rebounds limited to 100, aerodynamic diameters of 1, 5, 10, 50, 75 and 100 μm. 135
A.46 Deposition percentages for UXC case open to the surface level and neighboring cavern, 1.5 MW, 24 minutes, rebounds limited to 100, aerodynamic diameters of 1, 5, 10, 50, 75 and 100 μm. 135
A.47 Release percentages for closed UXC case, 1 MW, 31 minutes, standard local interaction particle sub model. 135
A.48 Deposition percentages for closed UXC case, 1 MW, 31 minutes, standard local interaction particle sub model. 136
A.49 Release percentages for closed UXC case, 1.5 MW, 24 minutes, standard local interaction particle sub model. 136
A.50 Deposition percentages for closed UXC case, 1.5 MW, 24 minutes, standard local interaction particle sub model. 136
A.51 Release percentages for UXC case open to the surface level, 1 MW, 31 minutes, standard local interaction particle sub model. 137
A.52 Deposition percentages for UXC case open to the surface level, 1 MW, 31 minutes, standard local interaction particle sub model. 137
A.53 Release percentages for UXC case open to the surface level, 1.5 MW, 24 minutes, standard local interaction particle sub model. 137
A.54 Deposition percentages for UXC case open to the surface level, 1.5 MW, 24 minutes, standard local interaction particle sub model. 138
A.55 Release percentages for cavern case open to the surface level and neighboring cavern, 1 MW, 31 minutes, standard local interaction particle sub model. 138
A.56 Deposition percentages for UXC case open to the surface level and neighboring cavern, 1 MW, 31 minutes, standard local interaction particle sub model. 138
A.57 Release percentages for cavern case open to the surface level and neighboring cavern, 1.5 MW, 24 minutes,standard local interaction particle sub model. 139
A.58 Deposition percentages for UXC case open to the surface level and neighboring cavern, 1.5 MW, 24 minutes, standard local interaction particle model. 139

B.1 Initial conditions for a model of the CMS experimental cavern open to the the surface level and neighboring cavern. 153
B.2 Boundary conditions for a model of the CMS underground experimental cavern open to the surface level and neighboring cavern. 154

List of Symbols

Latin characters

Symbol	SI-Unit	Definition
a	-	Absorption coefficient
c_k	-	LES constant
c_ϵ	-	LES constant
c_Δ	-	LES constant
c_p	$\mathrm{J{\cdot}(kg \cdot K)^{-1}}$	Specific heat capacity at constant pressure
c_v	$\mathrm{J{\cdot}(m^3 \cdot K)^{-1}}$	Specific heat capacity at constant volume
d_i	m	Average direction vector
g_i	$\mathrm{m{\cdot}s^{-2}}$	Gravity vector
e	-	Emission coefficient
h	$\mathrm{J{\cdot}kg^{-1}}$	Enthalpy
h	m	Height
k	$\mathrm{m^2{\cdot}s^{-2}}$	Turbulent kinetic energy
m_p	kg	Particle mass
n	-	Number of products
n_prod	-	Total number of product moles
n_reb	-	Number of particle rebounds
p	Pa	Pressure
p_0	Pa	Ambient pressure
$\dot{q}''$	$\mathrm{W{\cdot}m^{-2}}$	Thermal radiative heat flux
s_air	-	Stoichiometric air-fuel ratio
s_{O_2}	-	Stoichiometric oxygen-fuel ratio
t	s	Time
u_i	$\mathrm{m{\cdot}s^{-1}}$	Velocity vector
$u_{i,\mathrm{p}}$	$\mathrm{m{\cdot}s^{-1}}$	Particle velocity vector
x_i	m	Position vector
A_s	$\mathrm{s^{-1}}$	Transport coefficient

C_d	-	Drag coefficient
D_eff	$\mathrm{m^2 s^{-1}}$	Effective mass diffusion coefficient
E	-	Emission fraction / wall function constant
$\mathrm{E_{HRR}}$	-	HRR fraction converted to thermal radiation
F	$\mathrm{kg{\cdot}m{\cdot}s^{-2}}$	Force
F_{1-2}	-	View factor
G	$\mathrm{W{\cdot}m^{-2}}$	Incident radiation
ΔH_c	$\mathrm{J{\cdot}kg^{-1}}$	Heat of combustion
$\Delta H_\mathrm{c,P}$	$\mathrm{J{\cdot}kg^{-1}}$	Chemical product enthalpy
$\Delta H_\mathrm{c,R}$	$\mathrm{J{\cdot}kg^{-1}}$	Chemical reactant enthalpy
I	$\mathrm{W{\cdot}m^{-2}}$	Thermal radiation intensity
I_b	$\mathrm{W{\cdot}m^{-2}}$	Black body emission
I	-	Identity tensor (equal to δ_{ij})
M_f	$\mathrm{g{\cdot}mol^{-1}}$	Molar mass of fuel
M_i	$\mathrm{g{\cdot}mol^{-1}}$	Molar mass of specie i
$\overline{M}$	$\mathrm{g{\cdot}mol^{-1}}$	Weighted molar mass
M_prod	$\mathrm{g{\cdot}mol^{-1}}$	Total molar mass of all products
$\mathrm{Pr_t}$	-	Turbulent Prandtl number
$\dot{Q}$	W	Heat release rate
R	$\mathrm{kg{\cdot}s^{-1}}$	Reaction rate
R	-	Thermal radiation source term component
S	-	Source term
S_comb	-	Combustion source term
S_thermrad	-	Thermal radiation source term
S_f	-	Face area vector
Sc	-	Schmidt number
T	K	Temperature
T_s	K	Transport coefficient
V	$\mathrm{m^3}$	Volume
X_i	-	Mole fraction of specie i
Y_i	-	Mass fraction of specie i
$\mathfrak{R}$	$\mathrm{J{\cdot}(mol \cdot K)^{-1}}$	Universal gas constant

Greek characters

Symbol	SI-Unit	Definition
α	$\mathrm{m{\cdot}s^{-2}}$	Laminar thermal diffusion coefficient
α_{eff}	$\mathrm{m{\cdot}s^{-2}}$	Effective thermal diffusion coefficient
α_{t}	$\mathrm{m{\cdot}s^{-2}}$	Turbulent thermal diffusion coefficient
κ	-	Von Kármán constant
χ	-	Combustion efficiency
μ	Pa·s	Laminar dynamic viscosity
μ_{eff}	Pa·s	Effective dynamic viscosity
μ_{t}	Pa·s	Turbulent dynamic viscosity
ν	$\mathrm{m^2{\cdot}s^{-1}}$	Laminar kinematic viscosity
ν_{eff}	$\mathrm{m^2{\cdot}s^{-1}}$	Effective kinematic viscosity
ν_{t}	$\mathrm{m^2{\cdot}s^{-1}}$	Turbulent kinematic viscosity
ν_i	-	Stoichiometric factor of specie i
$\overline{\rho}$	$\mathrm{kg{\cdot}m^{-3}}$	Averaged density (by mass-fraction)
ρ	$\mathrm{kg{\cdot}m^{-3}}$	Density
σ	-	Stefan-Boltzmann constant
τ_{ij}	-	Viscous stress tensor
Δ	-	LES model constant
Θ	-	Polar angle
Φ	-	Azimuthal angle
Ω	-	Solid angle

Nomenclature

^{36}Cl	Chloride-36, radioactive isotope emitting β^-, β^+ radiation
^{60}Co	Cobalt-60, radioactive isotope emitting β^-, γ radiation
2D	Two-dimensional
3D	Three-dimensional
AD	Antiproton Decelerator
AFD	Automatic Fire Detection
ALICE	A Large Ion Collider Experiment
ASN	Autorité de sûreté nucléaire
ATLAS	A Toroidal LHC Apparatus
AWAKE	Advanced Wakefield Experiment
CAD	Computer-aided design
CCC	CERN Control Center
CDD	CERN drawing directory
CERN	Conséil européen pour la recherche nucléaire
CFD	Computational Fluid Dynamics
CMS	Compact Muon Solenoïd
CNGS	CERN Neutrinos to Gran Sasso
CSAM	CERN Safety Alarm Monitoring System
CTF3	Clic Test Facility
DIC	Diagonal incomplete-Cholesky
DILU	Diagonal incomplete-LU

EDMS	CERN Engineering & Equipment Data Management Service
FOAM	Field Operation and Manipulation
FRS	Fire and rescue service
fvDOM	Finite volume discrete ordinate model
FVM	Finite volume method
GAMG	Geometric-algebraic multi-grid solver
GIS	Geographic information system
HCl	Hydrochloride
HD-PE	High-density polyethylene
HiRadMat	High-Radiation to Materials
HSE	Health, Safety and Environment
ISOLDE	Isotope Separator Online Device
LD-PE	Low-density polyethylene
LEIR	Low Energy Ion Ring
LEP	Large Electron-Positron Collider
LES	Large-Eddy simulation
LHC	Large Hadron Collider
LHCb	Large Hadron Collider Beauty Experiment
LINAC	Linear Collider
LS0H	Low-smoke zero halogen
n-ToF	Neutrons Time of Flight
NFPA	National Fire Protection Association
NIST	National Institute of Standards and Technology
OECD	Organisation for Economic Co-operation and Development
PBiCG	Preconditioned bi-conjugate gradient solver

PCB	Printed circuit board
PCG	Preconditioned conjugate gradient solver
PDE	Partial differential equation
PE	Polyethylene
PISO	Pressure implicit splitting of operators
PMMA	Polymethyl methacrylate
PRISME	Propagation d'un incendie pour des scénarios multi-locaux élémentaires
PS	Proton Synchrotron
PVC	Polyvinyl chloride
RANS	Reynolds-averaged Navier-Stokes
RP	Radiation protection
SFPE	Society of Fire Protection Engineers
SIMPLE	Semi-implicit method for pressure-linked equations
SPS	Super Proton Synchrotron
STL	Stereolithography
SX5	Experiment surface building at LHC access point no. 5
UL	Underground liaison gallery
USC	Underground service cavern
UXC	Underground experimental cavern
XLPE	Cross-linked polyethylene

1 Introduction

In 1945 the first nuclear bomb test was set up in New Mexico in the United States of America. The so called "trinity test" was one of the early major incidents involving artificially created radioactivity. Even today, scientists are looking back to understand what was going on, and how it influenced our society on to now [1].

Radioactivity as such is a phenomena that cannot be recognized by humans using their ears, eyes or noses. Following the bombing on Hiroshima and Nagasaki in 1945, incidents in Chernobyl in 1986 or more recently Fukushima in 2011, scientists and engineers, collaborating world-wide, created and continuously develop the subject of radiation protection.

Today, radiation is used in a lot of industrial and medical processes, e.g. using electromagnetic X-ray technology to ensure material quality in mechanical engineering or treating patients in hospital with certain radioactive isotopes to reveal, exclude and treat illnesses such as cancer. Due to this commonly accepted use of radioactive isotopes for various purposes, radioactive materials and devices are wide-spread across the world.

Installations, ranging from a general practitioner's X-ray device to hospital laboratories to nuclear power plants and laboratories, have to undergo adapted risk assessments. Depending on the overall radioactive inventory, the amount of sources of radioactivity and their intended use, assessments are highly regulated, and generally supervised by governmental institutions.

Radioactivity as such poses a risk. So do environmental or climate conditions, accidents and intended or non-intended misuse. Fire, accidentally or intentionally caused, is one of the other risks, usually encountered in most types of above mentioned installations. A risk assessment has therefore to relate one risk with another, to evaluate possible scenarios and how to prevent them.

In this thesis, existing risk assessment procedures and computational fluid dynamics (CFD) technologies are merged to create a new engineering tool. It allows to quantitatively assess the outcome of fire scenarios involving radioactive materials towards an

integrated fire and radiation protection approach.

The following section will introduce the European Organization of Nuclear Research, its accelerators and large-scale experiments, giving already a first reason for the use of CFD in risk assessment. It is followed by the initial motivation to carry out this thesis work.

1.1 CERN, the LHC and CMS

After the second world war, several European scientists started to think about a joined research in nuclear sciences. In 1949 a first proposal was brought up by Louis de Broglie participating at the European Cultural Conference in Lausanne, Switzerland, followed by another in 1950 by the American Isidor Rabi on the 5$^{\text{th}}$ UNESCO General Conference in Florence, Italy. Still it took another year until 11 countries signed an agreement for a temporary council on European Nuclear Research in Paris. The "Conséil européen pour la recherche nucléaire", CERN, was born. The acronym survived the time of the council and is still used today. For more details on the history of CERN as an international organization the reader is referred to the organization's main web site [2].

Since 1954 several different particle accelerators have been built. One of the oldest still in use is the Proton Synchrotron (PS) from 1959, followed by the Super Proton Synchrotron (SPS) erected in 1976. Today, the Large Hadron Collider (LHC) is housed in the tunnel of the former Large Electron-Positron Collider (LEP, started in 1989, decomissioned in 2000), cf. figure 1.1. The reader is referred e.g. to the original LHC paper for more information [3, 4].

With a circumference of 27 km, the LHC particle accelerator is currently the world's largest circular collider. Usually proton-proton and ion-ion collisions take place, but at the end of the first LHC operation period, also ion-proton collisions have been successfully tested. To create proton-proton collisions, hydrogen atoms are stripped from their electrons, leaving only the protons behind, followed by a first linear acceleration in CERN's second built linear accelerator (LINAC 2). Then, particles are injected into a first short circular collider named BOOSTER. From there, the particle clouds pass through the PS accelerator, the SPS accelerator and finally they are transferred into the LHC accelerator. While passing through the different accelerators, each particle's energy level is increased, up to 7 TeV. Ion clouds start at the third built linear accelerator

(LINAC 3) and pass through the low energy ion ring (LEIR) before continuing similarly through the accelerator chain, as described for the protons.

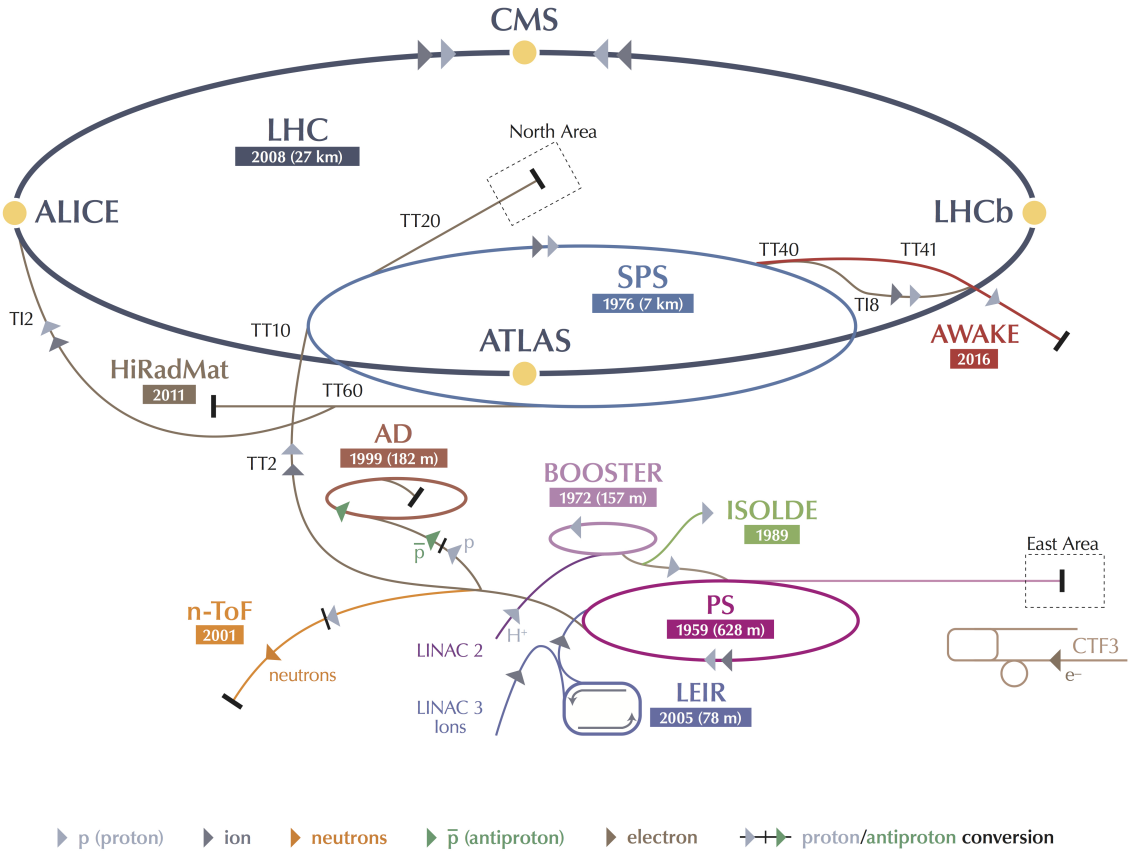

Figure 1.1: Overview of CERN's particle accelerator complex [5].

Around the LHC accelerator, four large-scale experiments [6, 7, 8, 9] and several small scale experiments [10, 11] are installed. Most of the equipment has been installed in the former LEP underground facilities. But for the "A Toroidal LHC Apparatus" experiment (ATLAS) and the "Compact Muon Solenoïd" experiment (CMS) new underground caverns had to be built. While the ATLAS experiment is based in Meyrin, Switzerland, facing the main site of CERN, the CMS experiment is on an opposing position next to the village of Cessy in France. Thus, the large-scale CMS experiment has to be autonomous from the two main sites, e.g. in terms of supplies but also in terms of safety and security.

The CMS experiment is a cylindrical shaped particle detector with a diameter of about

15 m and a length of approximately 21 m, cf. fig. 1.2. It consists of five wheel parts and two end caps. Four wheels and both end caps can be moved, the central wheel bearing the magnet coil is fixed. Included in its weight of 14,500 tons are 12,000 tons of steel to act as a yoke for the supra-conducting magnet coil. The remaining weight is made of electronics, cabling, sensors and other parts of the five installed sub detection systems.

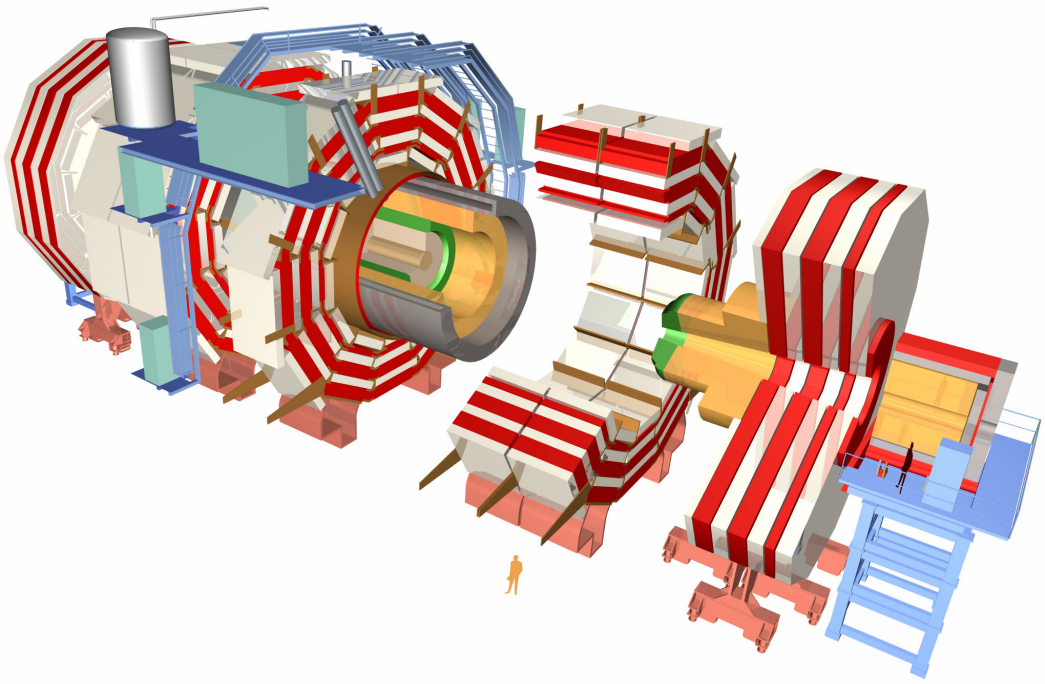

Figure 1.2: Compact Muon Solenoid Experiment in exploded view [12].

Wrapped around a beam pipe, multiple layers of sensors and two different calorimeters are placed within the aperture of the magnet-coil (the green-yellow-grey part in fig. 1.2). The outer part is split into layers of steel (red) and another particle sub-detection system, the Muon chambers (white). On top of the detector a 5000 liter vessel for liquid helium guarantees a cooling supply of the solenoid. Other support facilities are installed around the detector, mainly on technical galleries (only partly shown).

The detector and its supplying installations are mainly installed in two big underground caverns of about 50,000 m^3 each.

1.2 Motivation

So far, risk assessments for the French nuclear authorities "Autorité de sûreté nucléaire" (ASN) and the Swiss equivalent "Office fédéral de la santé publique" (OFSP) have been summed up in technical reports, e.g. such as the one for the ASN concerning the SPS particle accelerator, the CERN Neutrinos to Gran Sasso (CNGS) experiment and the LHC particle accelerator in 2008 [13, 14]. It covers main aspects with respect to safety and security of the named installations. Therein a part is dedicated to studies on probable accident scenarios, including the possibility of a fire incident involving a radioactive fire load.

One scenario imagined in a part of a facility with, comparatively, high dose rates and thus a high yield of activated material, takes into account a fire consuming all combustible materials present, leading to a hundred percent release of radioactive isotopes included in the fire load, cf. figure 1.3 for a schematic.

(a) Activated fire load (b) Fire incident (c) Release

Figure 1.3: Schematic representation of a worst case fire scenario with respect to radiation protection.

In this case 100% release means, that all radioactivity present under ground (in a part of the accelerator tunnel) is released to the surface where then the public would be exposed to the resulting dose. So far, this scenario represents the worst case that could

happen. However, a 100% release of radioactivity is a very conservative value and could lead to a misinformation of authorities and the public.

To provide one possibility to overcome the conservative way of considering fire scenarios including radioactive fire loads, a computational fluid dynamics model will be used in this thesis. Currently there is no possibility to carry out real fire experiments in the underground installations, as the LHC accelerator and its experiments are operating since 2008. Due to the nature of being a sophisticated, uniqe and complex device, the LHC accelerator and its experiments cannot be used for artificial smoke tests either, as conflicts of artificial smoke with measurement devices such as parts of particle detectors cannot be fully excluded. Other means, such as the use of a physical model including scaling has been proven to be difficult [15]. On the contrary, using only simulations makes an analysis prone to various code-related problems and errors [16]. Thus, a balance between a reality-based model and a decent verification in terms of error cross-checking has to be found. Finally, this model shall take into account the most important characteristics of the real underground experimental cavern while still being suitable for application.

Chapter 2 introduces the reader to the Compact Muon Solenoid Experiment, its fire safety concept and additional fire scenarios provided by the author. Scenarios with radiation protection aspects are modeled, using the open source solver fireFoam [17, 18]. Chapter 3 covers the state of the art of such applications, the different model setups and run time characteristics. A detailed cross-check in terms of verification and validation of the numerical results is given in chapter 4, followed by the simulation results in chapter 5. Finally, conclusions are summarized in chapter 6 and recommendations for further research are given.

2 Fire risk analysis and fire scenarios

At the time the author joined the CMS collaboration in September 2011, the CMS experiment was already operating. All safety systems and safety-related system based on prior risk assessments had been put in place. Section 2.1 summarizes briefly the current fire safety concept of the CMS particle detector, while in section 2.2 the new derived fire scenarios are discussed. Conclusions are summarized in section 2.3.

2.1 Initial concept

To protect the CMS particle detector in case of a fire incident, a modular fire safety concept has been put in place. Section 2.1.1 introduces shortly to the underground civil engineering aspects, followed by fire prevention (sec. 2.1.2), fire protection (sec. 2.1.3 and fire intervention concept parts (sec. 2.1.4). Section 2.1.5 provides details on the available means of escape.

2.1.1 Civil engineering

The principle structure of the CMS underground installations are two caverns of different size and position, both with its own access shaft connecting each cavern individually to the surface level. Figure 2.1 shows the new underground structures for the CMS experiment at access point 5 of the LHC acelerator (grey-shaded). The non-shaded parts belong to the former LEP tunnel installations. One cavern is dedicated to house the particle detector and its immediate supply systems inside, referred to as underground experimental cavern (UXC), cf. [19]. It has a length of 53 m, a width of 26.6 m, and a height of 24 m (approximate values). Its ceiling is round shaped. At one cavern end, a round access shaft of 74 m length, with a diameter of 20.5 m, is connecting the cavern to the surface. A volume of about 50,000 m^3 was estimated for the experimental cavern and its access shaft, based on the as-built civil engineering drawings. Both, experimental cavern and its access shaft contribute almost equally. Inside the experimental cavern

steel based galleries provide access to the particle detector and serve as supply structure, hosting electrical and electronic cabinets, cooling installations etc.

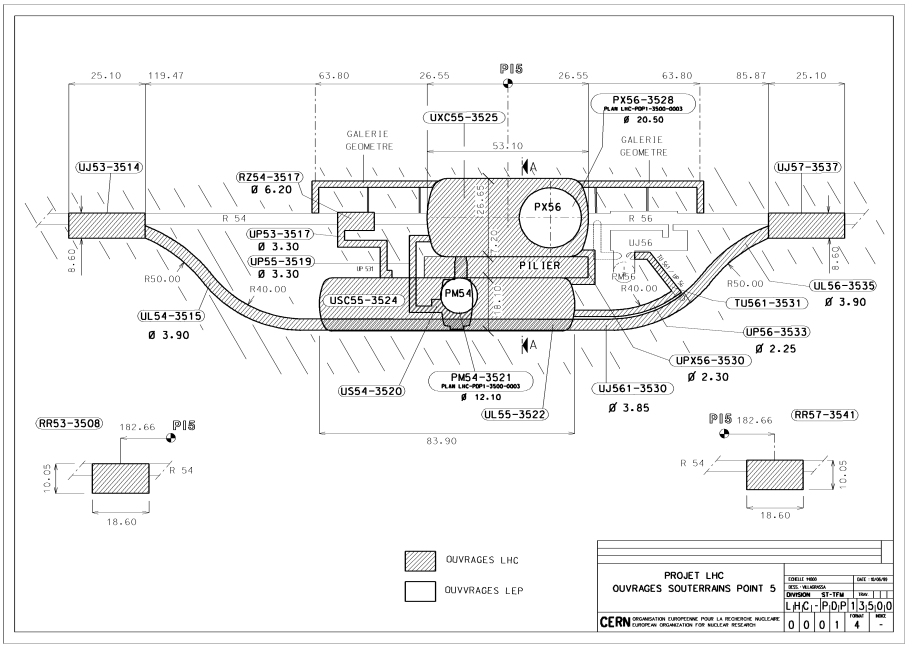

Figure 2.1: Overview of the underground installations at access point 5 of the LHC particle accelerator.

All other underground supply systems, including a large computing center, are installed in an underground service cavern (USC) in the direct vicinity. Both caverns are connected by two pedestrian tunnels and a rectangular cross-section of 4.1 m x 7 m on the far side of UXC's access shaft. Thus both sides of the detector are covered in terms of material supply and removal. Both caverns and interconnections are made out of steel reinforced concrete.

The two caverns are separated by a seven meter thick pillar, also made of steel reinforced concrete (cf. the area including the French word "Pilier" in fig. 2.1). Inside this block six additional cavern-to-cavern connections are present, referred to as underground liaison galleries (UL). They provide power, water, gases, signal processing etc. from the service cavern to the experimental one.

2.1.2 Fire prevention

At CERN internal rules are issued in the framework of a corporate safety concept. Fire prevention is covered within the safety code (French "Code de Securité") E [20]. Safety codes are supported by safety instructions (French "Instruction de Securité (IS)"), regulating e.g. the use of cables and the use of plastics at CERN [21, 22]. In case of the latter, both list materials for which their underground use and installations is forbidden by default, e.g. low-density polyethylene (LD-PE), polyvinyl chloride (PVC) and polymethyl methacrylate (PMMA). These materials must not be used for cable parts such as sheathing, too.

Cables represent a major fire load in CERN's underground installations. Due to the regulations stated above, their hazard potential in terms of fire safety could be already reduced, compared to standard industrial installations. Cables must be low-smoke producing (in terms of obscuration of a light source) and halogen free (LS0H). About 99% of all cables installed in the CMS epxeriment underground premises possess this improved reaction to fire, compared to standard industry grade cables. For some prohibited materials a synergy effect exists in the sense of enhancing both, fire safety and radiation protection, e.g. a cable containing chlorides would produce hydrochloride (HCl) in case of fire, while a cable containing chlorides could change to Chloride-36 (^{36}Cl) in case of irradiation. While HCl has hazardous and corrosive effects to humans and installations, Cl-36 is a radioactive isotope emitting beta radiation, with a half-life of about 301,000 years. Thus, depending on the variety and concentration of isotopes, activated material has to be declared as radioactive waste, to be stored safely and later to be disposed accordingly [23].

For certain materials, the use within the experiment is unavoidable. To provide enhanced neutron shielding in both end caps of the CMS detector, in total about 30 tons of polyethylene (PE) had to be installed. Fire tests have been carried out in order to identify the fire risk and investigate on compensatory measures. In the case of the PE shielding it was decided to cover each shielding wedge made of PE by an intumescent paint [24]. Also for neutron shielding reasons, additional 140 kg of paraffin had to be installed next to the inner parts of the detector. Based on its material characteristics (e.g. low melting point) the use is conditional to the use of aluminum enclosures for the material, being in return also covered with intumescent paint, and the presence of a melt cable, signaling upon receiving a critical amount of thermal radiation [25].

Beside reducing the amount of combustible material in its underground installations, the CMS experiment uses state-of-the-art fire prevention measures, such as fire doors, seals and dampers. Both caverns form fire compartments, extending up to the surface level (in case of the USC even beyond) due to their individual access shafts. Between the caverns all tunnels are closed by appropriate doors or fire seals, no active or passive fire dampers are used.

2.1.3 Fire protection systems

As CMS being a remote experiment with respect to CERN's main site, its is partially relying on automatically triggered actions. In all underground areas an automatic fire detection (AFD) system is installed. This system is an aspiration detection system. Different volumes are covered by grouped lines. Each line is equipped with its own aspiration device composed of two independent detectors. If both are triggered at the same time by the entrained air sample, the device will cause an alarm [26]. For certain installations, automatic interlocks exists, cutting e.g. automatically power or other supplies upon confirmed smoke detection.

A fiber optical system (FOS) has been installed in and around the CMS particle detector. It provides temperature, strain and humidity information by embedding appropriate sensors along a glass fiber. Currently 70 fibers are used with a total length of approximately 5 km, connecting about 1,000 sensors in total [27].

To cover the inner parts and the endcaps of the detector, another detection system, the SNIFFER was introduced. It follows the same principle as an aspiration detection system, but additional sensors for various gases are available. The number of detection tubes per analysing unit as well as their maximum length are increased, compared to the normal AFD system [28]. SNIFFER tubes are installed at both end caps and inside the inner detector part, cf. figure 2.2.

Fire alarms as well as evacuation alarms are transmitted in a dedicated fail-safe network, also referred to as CERN Safety Alarm Monitoring System (CSAM). These type of alarms are always forwarded to the CERN control center (CCC) and invoke automatically a notification of CERN's fire and rescue service (FRS) [29].

A medium-pressure water mist system is covering mainly the cable tray installations between the service and the experimental cavern. Ten extinguishing zones are defined in total, five in each cavern. Every zone can be triggered manually in situ by pressing

a button or by triggering remotely from the surface control room of the experiment. An additional autonomous mode exists, where the system is triggered by automatic fire detection providing a signal to the detector safety system [30].

About 180 electric and electronic cabinets have been installed in the experimental cavern, housing low- and high-voltage power supplies and other electric or electronic equipment. Cabinets crucial for the operation of the detector are equipped with carbon dioxide (CO_2) extinguishing systems. These systems include a release nozzle, a smoke detector at the top of each protected volume and a melt cable therein. Each cabinet is equipped with its own CO_2-bottle. Only if both, the smoke detector and the melt cable provide an alarm signal, the system is triggered automatically. A manual activation is possible [31].

Additional mobile and fixed fire-fighting equipment has been installed throughout the CMS underground installations. Mobile fire extinguishers inside the experimental cavern are made from non-ferromagnetic material to avoid handling problems in the stray field of the CMS magnet. Fixed fire hose reels are fed by a fire water network supplied along the LHC accelerator tunnel. It is sourced at LHC access point 1 by a direct underground pipe connection to the lake of Geneva.

The experimental cavern's air is regularly exchanged by an air management system, relying on 12 inlets and outlets. Its volume flow varies depending on the set condition from 22,500 $m^3 \cdot h^{-1}$ during normal operation up to 90,000 $m^3 \cdot h^{-1}$ in case of a confirmed oxygen deficiency or fire incident [32]. Air is recirculated during operation and extracted to the surface level during an incident, where it is released to the environment. Although not designed as a smoke extraction system according to the usual standards, the system is built to sustain operation for two hours, being exposed to a temperature of up to 400°C [33]. During operation of the LHC accelerator the air management system extracts more volume than it entrains and thus provides a pressure difference of about -20 Pa w.r.t. the ambient pressure level. Inside the LHC accelerator tunnel, a pressure difference of about -40 Pa w.r.t. the ambient is maintained. This pressure cascade (dynamic confinement) ensures a containment of dust inside the tunnel. Contamination of experiments by dust, activated due to ionizing radiation, is a possibility that has to be taken into account.

Being the most important parts, the inner detector inside the superconducting solenoïd (cf. figure 2.2) is permanently inertized. During operation 500 $m^3 \cdot h^{-1}$ of hypoxic air (a mixture of 95% nitrogen and 5% oxygen [34, 35]) flush the volume. The supply is ensured by a membrane plant at surface level. For the outer detector parts, i.e. the

muon detectors, a temporary nitrogen inertization system is installed. It allows to flush each gap between two wheels, independently from the others. Two storage vessels of about 80 m^3 each at 1.4 MPa provide nitrogen supply at surface level.

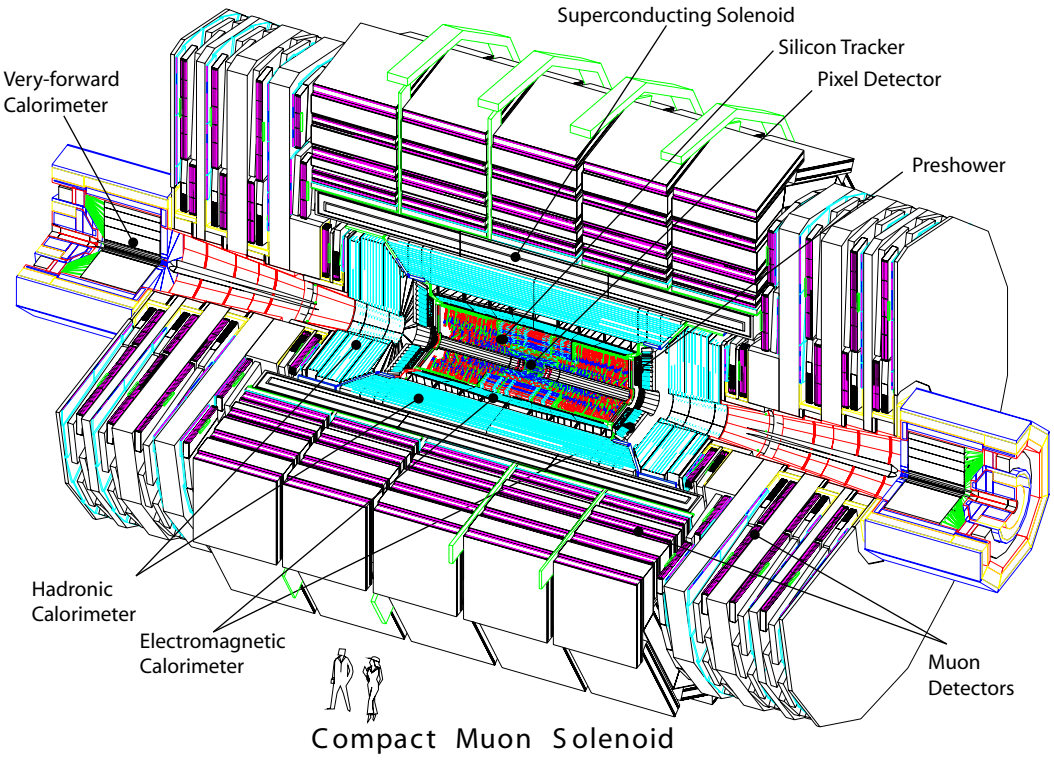

Figure 2.2: Labeled drawing of the CMS Experiment and its inner detector [12].

A high expansion foam extinguishing system is installed inside the CMS experimental cavern, in addition to all other systems described above. It shall protect the load-bearing structure of the cavern, the CMS detector and all its ancillary installations. Twelve high expansion foam generators are supplied by 130 m^3 of water stored and permanently available at the surface level. The mandatory foam concentrate (5 m^3) and mixture system is located inside the underground service cavern. Due to the difference of about 98 m between surface level and experimental cavern floor level, a static pressure of about 1 MPa is provided to the system. It allows a passive design of the system and ensures its operation for about 40 minutes. Being designed according to NFPA 11, a submergence time of ten minutes results in a rate of discharge of about 55 $m^3 \cdot s^{-1}$ of

high expansion foam [36]. Contrary to normal use (and French standards) the system is operated manually only.

2.1.4 Fire brigade intervention procedures

CERN's own FRS is based at Meyrin, Switzerland. The average intervention time between the fire department and access point 5 of the LHC accelerator is about 25 minutes, despite using the exclusive rights of a fire brigade. External effects such as seasonal weather conditions or frequent local traffic jams may influence this time frame significantly. Therefore the CMS experiment must aim for being autonomous in case of safety-related incidents that require the intervention of the organization's FRS.

To simplify and ease each intervention, incident-depending flow charts have been established. Together with centralized databases, e.g. such as a geographic information system (GIS), most necessary information is present and kept up to date.

2.1.5 Means of escape

At the CMS experiment no direct mean of escape exists between the underground experimental cavern and the surface level. All evacuating personnel must pass through the underground service cavern, to reach one out of three available safe areas. Each safe area is placed in front of the personnel elevator inside the service cavern which serves also as primary mean of escape. To guarantee the availability of the elevator in case of a power cut, it is put on a secured power network that is fed by a Diesel generator on surface level. Behind the elevator an emergency staircase provides a second secured mean of escape. Elevator and secured staircase are installed within steel-reinforced concrete modules. Both volumes are protected by a pressure difference of 20 Pa w.r.t. the ambient in order to avoid intake of smoke or asphyxiating gases.

All safe areas are equipped with means of communication, a fire extinguisher and a first aid kit. Doors leading from the cavern to safe areas have a minimum fire resistance of 120 minutes. Each safe area is provided with a pressure difference of 20 Pa w.r.t. the ambient due to the fact that they are open towards the elevator shaft.

Evacution distances exceed the maximum distance prescribed by French law (40 m) [37]. As this underground site is used for work only by trained and accordingly equipped personnel, a derogation was issued. Evacuation exercises have been carried out in the

past, proving an evacuation time of about 3 minutes for the entire experimental cavern, being occupied by about 100 persons. Evacuation from remote mobile working platforms, frequently used inside the experimental cavern, has been taken into account [38].

2.2 New fire Scenarios

A development of credible fire scenarios is part of a fire risk assessment. Scenarios have to take into account a variety of aspects, such as fire load density, ventilation conditions and available ignition sources. Further information has to be provided on the expected operational state of the target. Whether analyzing a batch reactor in a chemical industry plant or a particle detector, most installation use is divided into operational, short and and long-term maintenance periods.

Event trees provide a deeper understanding of possible sequences of actions. Their application allows an optimization of safety systems to avoid certain chain of events. Figure 2.3 gives an example for a smoldering cable fire incident in an arbitrary CERN facility.

Here, the author assumes a probability of 100%, that a fire incident will occur. Then, the course of actions depend on the presence and availability of technical safety systems such as fire detection, automatic power cut upon confirmed fire detection, water mist suppression system or similar and of the type of cable material. Answering the presence and availability of such systems with yes or no provide a sceanrio state at the end: either the fire will extinguish itself, or, it will continue.

If available, statistics combined with event trees allows to assign scenario probabilities, e.g. apartment buildings in Australia, Canada and the Unites states show a probability of about 20% to reach only the smoldering phase in case of a fire incident [39]. However, at the time of the investigation detailed statistics on fire incidents in particle physics laboratories have not been available. An exception was found in the work of Harrison, providing a probability value for a fire incident based on electric fault in the LHC accelerator tunnel [40].

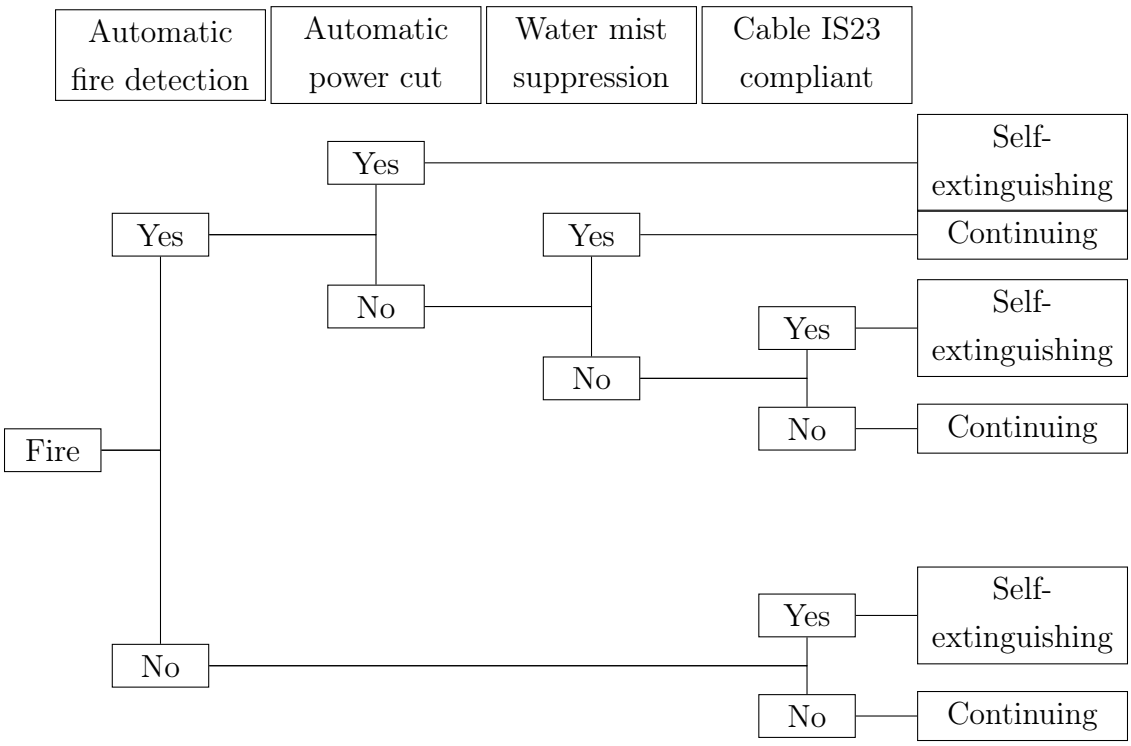

Figure 2.3: Example event tree for a smoldering fire scenario in a CERN facility.

This section presents three different fire scenarios that have been identified by the author, discussed in subsections 2.2.1, 2.2.2 and 2.2.3. Two of them are independent of the operational state of the experiment and the LHC accelerator. One is based on mobile fire load, while two are dealing with fixed combustible materials. Despite the exposure of the particle detector to ionizing operation, at the time of the investigation only one fire scenario could be found which has to seriously take into account the presence and participation of activated material in case of fire.

2.2.1 Smoldering cable fire

From the history of fire incidents at CERN it is known to have at least one minor incident (smoldering, glowing, small flaming fire) per year of operation of the LHC accelerator. Some of these minor incidents are related to faulty connectors, cables or sockets. Several hundred kilometers of cables are installed in the CMS experimental cavern e.g. to supply sub detection systems with electricity or connect detector parts by optical fibers with their post-processing hardware. Different types of cables and fibers

are used, concentrated in cable trays. Electricity is the primary ignition source during operation, followed by hot work during maintenance periods.

Information on the maximum load of cable trays following the French or Swiss regulations is scarce. A good example is found in article 392 of the US National Electric code [41]. However, densely packed cable bunches on overcrowded cable trays are not uncommon. Figure 2.4 gives an example of a typical cable tray found at CERN. The more dense the cables are placed, the less exposed is their surface to an external ingition source. Dense cable bundles have been found harder to ignite with an external heat source such as a propane burner [42]. On the contrary, once cable bundles ignite e.g. by sparks or hot spheres dripping from hot work on a tray, a higher fire load density leads to a larger heat release and smoke production.

Figure 2.4: Example cable tray in UXC55 (Picture taken in February 2015).

CERN asks for strict requirements with respect to cables [21]. As mentioned earlier in subsection 2.1.2, some material choices e.g. for cable sheathing or insulation are completely forbidden. Cable products have to comply with a broad range of standardized fire tests i.e. horizontal and vertical fire tests, cone calorimetry and smoke density chamber tests. A test according to IEC 60332-3-24 [43] is one of them. It prescribes a minimum

volume of non-metal material of 1.5 liter per meter of cable to be tested. Further, "The maximum extent of the charred portion measured on the sample shall not have reached a height exceeding 2.5 m above the bottom edge of the burner" [43] denotes clearly the condition to fail or pass this fire test. Thus, cables compliant to the use at CERN must be self-extinguishing within a certain length.

Assuming a maximum vertical cable propagation length of 2.5 m results in a volume of 3.75 liter of combustible cable material according to IEC 60332-3-24. With a reference density of 1152 $kg \cdot m^{-3}$ for a low smoke emitting halogen free cross-linked polyethylene (XLPE) cable jacket [44] one calculates a mass equivalent of 4.3 kg. Taking into account a heat of combustion of about 36.8 $MJ \cdot kg^{-1}$, as has been found by cone calorimetry for similar material [24], a XLPE cable with a length of 2.5 m could release up to approximately 158 MJ of energy.

Cables are categorized as slow burning material. To calculate the rate of heat release of such a type of fire one could use the t^2-model [39], cf. equation 2.1:

$$\dot{Q} = \left(\frac{t}{t_{1000}}\right)^2 \cdot Q_0 \tag{2.1}$$

In eq. 2.1 $\dot{Q}$ denotes the rate of heat release in kW, t the time in seconds, t_{1000} the time to reach 1 MW (600 s for slow propagating material) and Q_0 is a constant (1000 kW). Integrating eq. 2.1 from $t_0 = 0$ to $t_1 = 600$ s gives the amount of energy released within the first ten minutes, which is 200 MJ. Comparing the latter to the 158 MJ estimated above, it is evident that a single cable being compliant to IEC 60332-3-24 would not reach a HRR of 1 MW, but would rather smolder on a lower rate.

Taking into account a bundle of 10 cables with the same characteristics discussed above, the theoretical maximum energy is about 1580 MJ. Considering again a low propagation and 200 MJ for the initial 600 s, about 1380 MJ remain for the developed fire phase. Further, assuming a peak heat release rate of 1 MW, the fire incident could last more than 30 minutes (including the initial 600 s slow fire growth period).

2.2.2 Electrical cabinet fire

Electrical and electronic cabinets are widely used, from a small company housing a few servers up to large scale industrial installations, using cabinets for various purposes such as electric distribution, installation of printed circuit boards (PCB), servers etc. Regard-

ing fire safety of cabinets, little research has been done, mainly driven by the nuclear industry. The reasons are manifold, starting from fire load composition to ventilation conditions and the probability and force of ignition, usually by electricity. Electrical cabinets pose a difficult research topic in terms of setup, measurements and reproduction.

Back in 1987 Chavez and Nowlen issued two large reports on fire tests with cabinets, driven by the U.S. Nuclear Regulatory Comission and the Sandia National Laboratories. Part one covers cabinets in a "free" environment, part two deals with cabinets in a mechanically controlled environment. During phase one, cabinets have been tested in various conditions, e.g. with different ignition sources, ventilation conditions and fire load. Using a configuration open to the ambient, a peak heat release rate of about 1 MW was observed during a fire test, lasting 15 minutes and consuming all fire load available inside the cabinet [45].

In 2003 Mangs et al. published their results on smale and full-scale closed electric cabinet fire experiments. Real fire load consisting of e.g. circuit boards, cables, relays and connectors etc. was used. The material was ignited by a dedicated propane burner, noting the minimum power and energy necessary to set a cabinet on fire depending on its configuration. One of their worst cases was a cabinet loaded with about 91 kg of combustibles, mainly PVC and PE. The following fire lasted about 120 minutes providing an average heat release rate of about 100 kW (about 707 MJ in total, 43% mass loss). Fire spread to adjacent cabinets was observed after 10 to 16 minutes in some configurations. Fire growth in an electronic cabinet according to ISO/TR 13387-2 [46] was categorised as "slow" [42].

More experiments on closed cabinets have been carried out by William Plumecocq et al., using closed cabinet configurations featuring differences in geometry, ventilation and fire load. In most of the cases the maximum heat release rate was observed in the range from 25 to 575 kW. Tests lasted a few 100 seconds up to about 33 minutes. A linear propane burner was used to represent electrictiy as ignition source [47].

Further tests on well-confined but also under-ventilated electrical cabinets have been published by Coutin et al. Cabinets have been configured either with PMMA, or real electrical distribution equipment. The latter was judged to be mainly made up from polyethylene vinyl acetate (32%), PVC (30%), polyamide (26%), PE (9%) and others. A maximum heat release rate of 404 and 593 kW for the PMMA-loaden and electrical cabinet, respectively, has been estimated [48].

In the framework of the project PRISME (French acronym for "Fire propagation in elementary multi-room scenarios") in total 35 large-scale fire tests have been carried out from 2006 to 2011. Focusing merely on confined, mechanical ventilated volumes this approach satisfied merely requirements based on typical geometries found in nuclear installations. Additional experiments have been carried out, e.g. to measure the heat release rate of free burning cable configurations and electric cabinets. The latter show the slow fire propagation behaviour already pointed out by Mangs et al. in 2002. Open atmosphere electric cabinet fires reached peak heat release rates (HRR) of up to 1.6 MW [49].

Inside the CMS experimental cavern, mainly electric or electronic devices are installed within cabinets along the support structure placed on both sides of the particle detector (parallel to the LHC accelerator beam line). A part are also installed on top of the particle detector, or next to the forward calorimeter part as shown in figure 2.5.

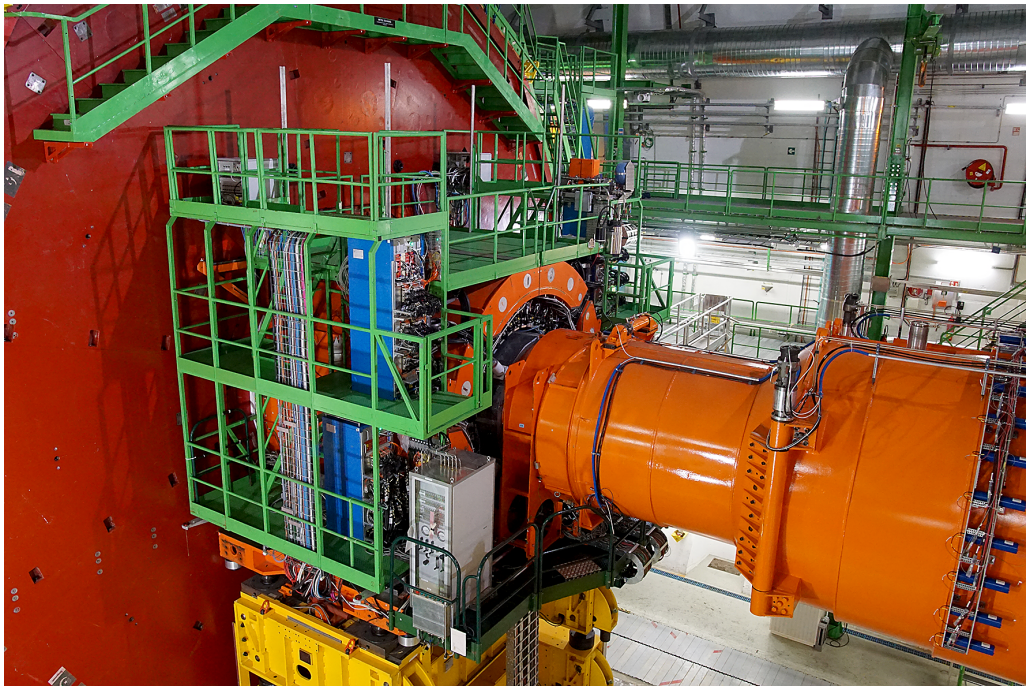

Figure 2.5: Forward calorimeter part of the CMS detector.

Cabinets in the forward calorimeter region are in the direct vicinity of the LHC accelerator beam line and therefore have been exposed to higher levels of ionizing radiation than e.g. the cabinets on the support structure. Measurements by the CMS safety unit

and CERN's radiation protection group have confirmed an activation of the present material. Both are monitoring the change of activity levels with continued operation.

Based on the available electrical cabinet fire data presented above (summarized in table A.2), a design fire of 1200 MJ with a peak heat release rate of 1500 kW represents a credible fire scenario. Caused e.g. by an electrical fault, it could take place in the foward calorimeter region of the CMS particle detector, during LHC accelerator operation as well as during short and long-term maintenance periods.

2.2.3 Mobile elevated work platform fire

During construction, commissioning and maintenance of the CMS experiment hydraulic work platforms have been used cf. fig. 2.6. Today, they are still in use to provide access to remote detector parts during short and long-term maintenance periods. For this purpose they are lowered from the surface level down to the experimental cavern.

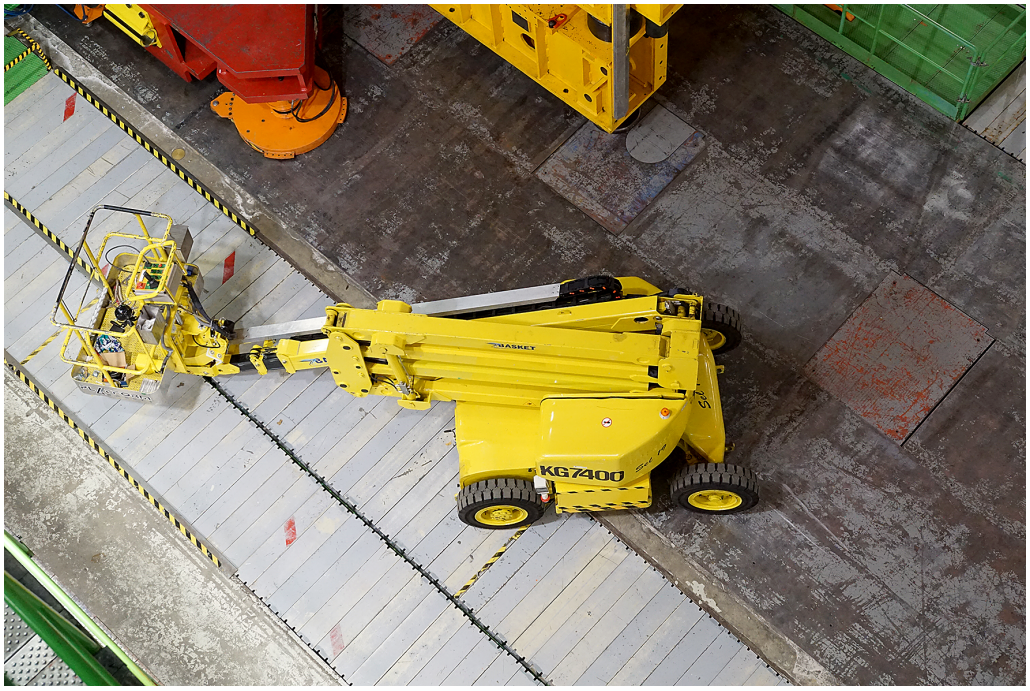

Figure 2.6: Mobile elevated work platform on rubber wheels (Type Marangoni Eltor E3 7.5-17/6.5, about 70 kg per tire).

All mobile elevated work platforms are equipped with lead-acid batteries. A battery caused already an incident in the past, where one elevated work platform's battery run

dry and started to smolder. Due to manual intervention, the incident could be limited and the ignition source in question was put out. However, as elevated work platforms are wheel-based, equipped with four rubber tires each, they impose a mobile fire load with its own ignition source which is not under supervision of a technical safety system. Thus these devices represent a valid threat in terms of fire safety.

Values for the heat of combustion could be found in the literature for rubber products, e.g. about 31.3 $MJ \cdot kg^{-1}$ in [50] or a range of 27.7 to 42.3 $MJ \cdot kg^{-1}$ [51]. Thus one tire, with a weight of about 70 kg, is in the order of magnitude of about 2400 MJ. This represents two times the energetic value of an electrical cabinet, cf. table A.3. A tire exposed to energy, e.g. of a dry run battery or ongoing hot work in the vicinity of the work platform is a scenario that has to be taken into account during maintenance periods. However, due to their short stays inside the underground experimental cavern, mobile elevated working platforms do not get activated.

2.3 Conclusions and recommendations

A modular concept of fire prevention measures, fire protection systems and operational procedures has been set up for the experimental underground installations of the CMS experiment. It relies on stopping any fire incident at its early stage. Despite the concept, fire load in the vicinity of the CMS particle detector is unavoidable and present. Electricity and hot work are the most likely ignition sources found, with respect to operation and maintenance periods of the LHC accelerator and its attached experiments.

Fire incidents in particle physics laboratories are in general not well communicated to the fire safety community, e.g. in journal papers or regular annual symposiums. One is tempted to look for comparable events in the scientific neighborhood such as the nuclear industry. However, fire scenarios drawn up for the latter focus often on confined volumes, relying on forced ventilation, thus merely representing under-ventilated fire scenarios. Their driving effects are analysed in various studies, e.g. in [48], [52] or [53]. But these installations usually do not feature the degree of freedom frequently found in the large-scale experiments along the LHC accelerator.

Although the fire safety concept covers well the experimental cavern housing the CMS particle detector, initially it was not based on well described fire scenarios. Three incidents likely to occur have been identified and described in section 2.2. While the

scenarios covering smoldering cables and electrical cabinets could take place anywhere in the experimental cavern (presuming sufficient cables or a cabinet present), the mobile elevated work platform is the only mobile and temporary fire load, as it is not present during LHC accelerator operation. All scenarios offer the same magnitude of energy release, while peak heat release rate or duration might vary.

As discussed in subsection 2.2.2, the electrical cabinets housing electrical and electronic components in the forward calorimeter region, next the the LHC accelerator beam line, are already radioactive. With respect to the foreseen operation time of the LHC accelerator and the CMS particle detector, an increase in terms of material activity is expected. It is the opinion of the author, that these electrical cabinets represent currently the worst case fire load with respect to radiation protection aspects within the experimental cavern of the CMS experiment. Therefore the elctrical cabinet scenario is modeled in the following chapter 3.

3 Fire modeling with fireFoam

One possible tool to identify fire safety improvements for the CMS experimental cavern is a CFD model. It can take into account also radiation protection aspects like release of aerosols and smoke from supervised areas. The author has chosen OpenFOAM as principal tool due to its open and modifiable source code, its flexibility and computational scalability. Next, the fireFoam solver is a natural choice, as it has already been proven to provide the means to calculate fire-induced thermal plumes. In addition, it includes already a Lagrangian particle framework.

The following section 3.1 covers shortly the historical origin and the current state of FM Global's fireFoam solver in terms of publications. To represent the fire scenario of an electrical cabinet, concluded in section 2.3, goals and objectives have been defined in section 3.2. Next a simplified modeling approach deemed to fulfill these objectives is described in section 3.3. It details which configuration of fireFoam and available sub models and libraries is chosen, e.g. in terms of geometry and meshing, combustion, Lagrangian parcels, thermal radiation and turbulence.

For a detailed description of the used system of partial differential equations (PDE) the reader is referred to appendix B. Necessary changes to the source code of OpenFOAM and fireFoam have been carried out by members of Wikki Limited, London, UK, or, by the author based on their suggestions.

3.1 State of the art

Simulation as a fire engineering tool was evidently accelerated by the publication of the Fire Dynamics Simulator, designed and maintained by the National Institute of Standards and Technology [54]. But also other tools have been developed and used before. A good overview can be found in the book of Yeoh and Yuen [55]. For application purposes of (fire) simulation the reader is referred to "usual suspects" such as the Handbook of the Society of Fire Protection Engineers (SFPE) [56] or national equivalents [50].

Following a wide acceptance of CFD for fire engineering a lot of different subjects have been modeled and analysed, such as compartment fires, wildland fires [57, 58, 59], tunnel fires [60], car park fires, etc. The current cutting edge is to link fire applications to generic algorithms, which offer an interesting improvement of model properties due to aleatoric extraction from real fire experiments [61].

FM Global, responsible for the fireFoam development, started in 2009 a series of annual workshops. Beside the presentation of the general evolution of the solver and the work done by FM Global personnel, several collaborating institutes are contributing each year, cf. [18, 62].

In 2010 Trouvé and Wang [63] published a general paper about large eddy simulation with respect to compartment fires. They presented two different open source solvers: FDS and fireFoam. Although results of both applications are shown, it is more a side-by-side presentation than a comparison. This is well suited, as the principal goals differ. The fireFoam research was initiated on a five year basis, to provide a toolbox for FM Global's fire engineers to better understand und enhance fire testing for their client's needs [64, 65]. As a start point, the management has chosen the quite complex topic of rack storage facilities, their fire dynamics and behavior, including the interaction with sprinkler or water mist suppression systems.

Wang et al. showed in 2011 a good agreement between their simulations of diffusion flames using large eddy simulation with fireFoam, and the well known plume equations by Heskestad et al. [66, 67]. Due to this work, the ability to use fireFoam for a diffusion flame and its thermal effects was proven. This work was extended by Chatterjee et al. in 2014 with respect to the ceiling jet [68]. Further papers from FM Global discuss interaction of water with solid surfaces during fire suppression [69], material property optimization schemes relying on bench-scale pyrolysis tests [70] and its application [71], thermal radiative heat transfer [72], thermal radiation of soot [73], thin water-film transport on solids [74], spray interaction with application to surface film wetting [75] or sprinkler suppression of rack storage fires [76].

3.2 Goals and objectives

For the CMS experiment the primary goal of this study is a gain in knowledge on the versatility of its air management in case of a fire incident. Notably its capabilities to

prevent a submergence of the detector and the supporting technical installations within a smoke layer shall be analyzed in detail. In case of a fire incident occurring in parts of the cavern where radioactive material has been identified, a suitable model shall be used to assess the release and deposition of aerosols to the surface buildings and the internal surfaces in the underground experimental area. Thus, this thesis touches fire safety and radiation protection principles towards a more joined approach for future use.

Following these two main goals, the following objectives have been defined by the author :

- Submergence time of the detector in a thermal layer of more than 60°C[1]; to be compared with the minimum intervention time of CERN's fire and rescue service
- Influence of the air management system in case of fire on the extraction of hot air and smoke
- Influence of the air management system on the thermal stratification in terms of stability of single layers or their mixing, possibly leading to an undesired state of local temperature rise etc.
- Estimation of the thermal load on cavern ceiling structures, in particular the high expansion foam extinguishing system and the crane rails
- Release of aerosols through the air management system
- Release of aerosols through the access shaft to the surface level and into the experiment surface building (SX5)
- Deposition of aerosols inside the underground installation, especially on the detector surface

3.3 Model setup

For each OpenFOAM model a minimum of information has to be provided, i.e. which geometry to be used with what kind of solver using how many and which libraries etc.

[1]Temperature threshold chosen based on findings of Purser and McAllister for a tolerance time for human exposure to convective heat equal to 30 minutes [77].

Further, user-defined stability criteria and numerical schemes influence the quality of results.

Based on the objectives presented in the previous section, three different model geometries have been identified for further use:

- Cavern closed; representing the operational state,
- Cavern open to the surface level; concrete plug on top of the access shaft removed, e.g. during short maintenance periods,
- Cavern open to the surface level and neighboring cavern; concrete plug on top of the access shaft and concrete block (towards the neighboring cavern) removed, only during long-term shutdown periods.

Their generation is discussed in section 3.3.1.

To represent the designated fire load containing radioactive materials, cf. fig. 2.5, a simple diffusion burner is used. The latter shall not (and cannot) model a flame or the exact combustion process. It shall rather act as a tool to produce the buoyant thermal plume that is representative of a given fire and its transport phenomena. Heat release rates for the burner are prescribed by the user, cf. section 3.3.2.

Lagrangian particles (synonymously used: parcels) are employed to represent the aerosols in case of fire. Modeled as ideal spheres, different aerodynamic diameters are taken into account to represent aerosols. These parcels are injected in the upper part of the induced thermal plume region, where temperature and velocity show a user-defined compliance with fire engineering expertise.

In fires normally thermal radiation plays a role, being one of the main heat transfer mechanisms. It can be modeled in different ways, by ideal spheres or individual rays emerging from a discrete surface. Two different thermal radiation sub models have been subjected to small-scale simulations, prior to any use with the full-scale underground experimental cavern model. For various reasons, no thermal radiation sub model is employed in the final cases, cf. section 4.5.

As all other solvers in OpenFOAM, fireFoam is a versatile one, also in terms of turbulence sub modeling. Various compressible and in-compressible Large-Eddy-Simulation (LES) and Reynolds-Averaged Navier-Stokes (RANS) turbulence sub models are available, such as the One-equation-Eddy or the dynamic Smagorinsky sub model for LES

and k-ϵ and k-ω sub models for RANS. Throughout this thesis work, only the One-equation-Eddy sub model has been used, following FM Global's example cases.

Environmental conditions within a large-scale physics experiment are kept very stable, i.e. during operation the air volume of the underground premises is kept as dry as possible with an average temperature of about 20°C. Due to the thick concrete walls and the surrounding stable soil layers, ideal conditions can be assumed in terms of initial and boundary conditions for fire simulations, cf. section 3.3.6.

To solve the set of partial differential equations described in annex B, several mathematical schemes (preconditioner and solver) have been used, cf. section 3.3.7.

3.3.1 Simplified geometry and meshing

In order to break down an entire operating large-scale physics experiment to a configuration suitable for CFD modeling, assumptions are made. First of all, the geometry to be used for calculations consists only of the underground experimental cavern, its access shaft and the particle detector, represented as a cylindrical shaped object. Based on the values provided by the as-built drawings, cf. table A.1, the author has used AutoCAD Inventor 2013, a commercial computer-aided design (CAD) tool to recreate a three-dimensional (3D) model. The model has been exported as a stereolithography (STL) file, as STL files can be read by OpenFOAM's mesh generating algorithm snappyHexMesh.

Apart from the detector and the air management system, no other internal installation or equipment such as the technical galleries, the forward calorimeter garages or the connections towards the LHC accelerator have been taken into account. As the technical galleries are made up from a steel framework and metal sheets at both sides of the cavern, their influence on a submergence of the detector into a smoke layer is negligible. Further, the two forward calorimeter garages may be open or closed. However, as their gates are not air tight, their volume will participate in any case. Finally the connection to the LHC accelerator tunnel is sealed by a huge pure steel shielding, acting equally as fire and radiation protection barrier. Thus, there is no open direct connection between the experimental cavern and the LHC accelerator tunnel. Further, the cavern walls towards the LHC accelerator tunnel could be treated as closed. In addition, also the volume covered by the LHC accelerator beam line and its steel shielding does not contribute in terms of submergence of the detector and has therefore been neglected.

Figure 3.1 gives an impression of the STL surface file created for the CMS experimental cavern, with and without air management system. With its supplying and extracting ducts being placed in the access shaft and below the cavern ceiling, it alters significantly the otherwise round shaped cavern ceiling and its round shaped access shaft. Therefore an approximation (subtraction) of its volume is included in the computational grid.

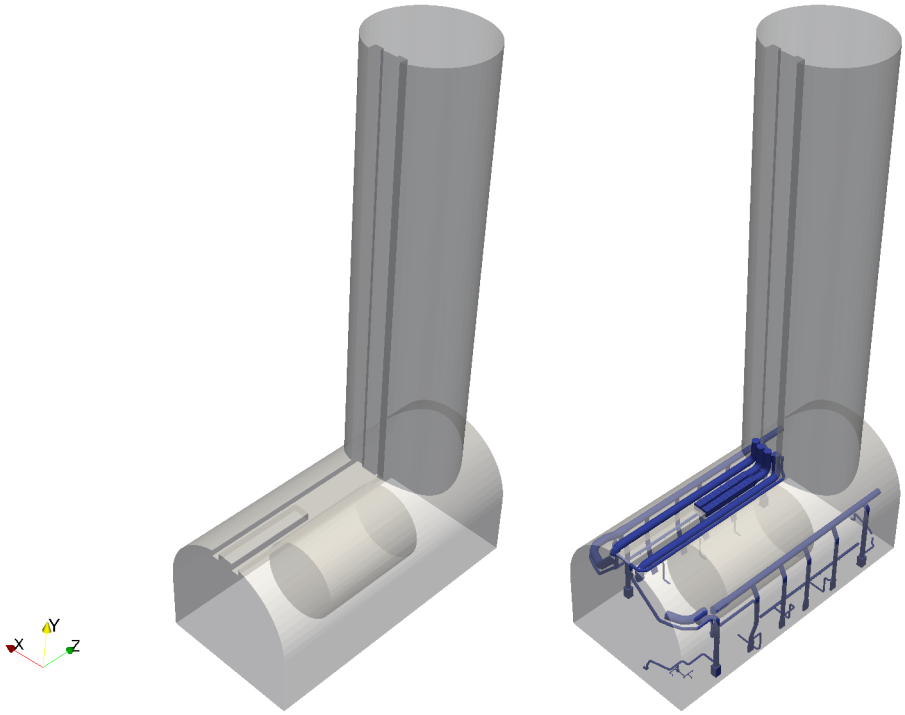

Figure 3.1: STL geometry of the CMS experimental cavern, access shaft and detector without (left) and with air management system (right).

Being a complex geometry, the snappyHexMesh tool [78, 79] has been used to create a computational grid of the CMS experimental cavern. It starts from a user-defined structured rectilinear mesh and treats the cells along the given STL geometry in a certain way to create cells that finally adapt ("snap") to it. Thus this algorithm is able to capture the complex joint between the round-shaped ceiling of the CMS experimental cavern and its access shaft, cf. fig. 3.2.

For all cases, a structured mesh (blockMesh) based on 40 cm x 40 cm x 40 cm uniform cells has been used as initial basis. Local refinements have been added, especially in the plume region, around the extraction outlet of the air management system, and the

corner between cavern ceiling and access shaft (20 cm cell size). In addition, the volume around the modeled diffusion burner has been refined to improve the formation of the buoyant thermal plume (10 cm cell size, cf. section 4.3. Refinements are justified by a series of verification simulations, cf. chapter 4, section 4.1.

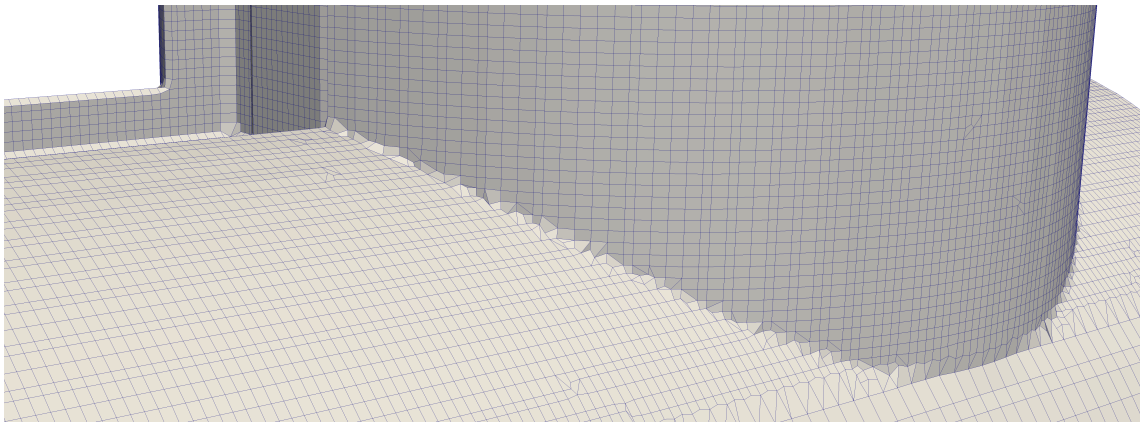

Figure 3.2: Detailed view of the joint between the round shaped cavern ceiling and round shaped access shaft.

Figure 3.3 shows a longitudinal cross-section of the mesh used to compute flow and Lagrangian particle dispersion inside the CMS experimental cavern open to the surface and the neighboring cavern. The transparent part in 3.3 gives an idea of the full extent. Therein, the block in the lower left part of the figure represents the connection to the neighboring cavern, while a huge representative volume is added on top of the access shaft (at surfacel level). For the closed cavern case, the volume ends at the cross-section equivalent to the surface level. No block is extruded towards the neighboring cavern. Instead, a pressure relieve box is attached, which is discussed below in section 4.2.

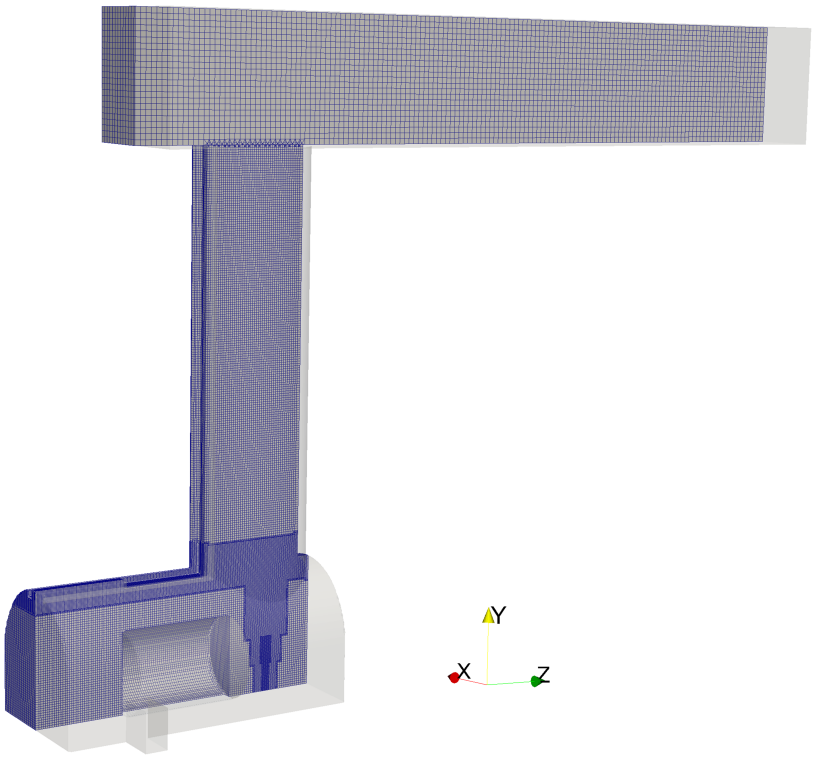

Figure 3.3: Longitudinal cross-section of the used computational grid.

3.3.2 Combustion sub model

To represent the diffusion burner already mentioned, the infinitely fast chemistry combustion sub model is used. Included in the standard OpenFOAM libraries, it allows to treat combustion of gaseous fuel in a basic approach. Where fuel and oxidizer are present, ideal combustion occurs by replacing the reactants with its products plus energy release according to the fuel chosen, cf. eq. 3.1:

$$\nu'_{\mathrm{f}}\,\mathrm{f} + \nu'_{\mathrm{O_2}}\,\mathrm{O_2} + \nu'_{\mathrm{N_2}}\,\mathrm{N_2} \rightarrow \nu''_{\mathrm{CO_2}}\,\mathrm{CO_2} + \nu''_{\mathrm{H_2O}}\,\mathrm{H_2O} + \nu''_{\mathrm{N_2}}\,\mathrm{N_2} + \Delta H_c \tag{3.1}$$

Here, ν'_{f} denotes the required number of moles of fuel (f), $\nu'_{\mathrm{O_2}}$ the required number of moles of oxygen (O_2) necessary for the ideal reaction, $\nu'_{\mathrm{N_2}}$, the number of required moles of nitrogen (N_2; if air is used as oxidizer), $\nu''_{\mathrm{CO_2}}$, $\nu''_{\mathrm{H_2O}}$ and $\nu''_{\mathrm{N_2}}$, denote the resulting number of moles of carbon dioxide (CO_2), water vapor (H_2O) and nitrogen, respectively.

The energy released during the reaction is represented by the heat of combustion, ΔH_c.

By design, this sub model does not take into account different time scales of the chemical combustion processes or the physical flow. Its idealized combustion is limited by the minor concentration - either by fuel or oxidizer. As it takes into account the concentrations in each discrete volume (mesh cell) inside the computational grid, this combustion process is mesh dependent, cf. section 4.3.

Choosing a simple approach for combustion such as the infinitely fast chemistry combustion sub model allows to model the outcome of a fire, i.e. its emerging thermal plume. Relying on ideal, complete combustion and neglecting a more complex incomplete combustion model is considered as conservative approach, as an ideal combustion provides more thermal energy e.g. for Lagrangian particle transport in a thermal plume than would be available due to incomplete combustion. Using a thermal plume as carrier, there is no particular interest in the combustion process itself, its related chemical species or its efficiency.

3.3.3 Lagrangian sub model

Originally the Lagrangian particle library of OpenFOAM was developed for spray modeling in Diesel combustion engines [80]. Today it is intensively used to model sprinkler or water mist nozzles, being one of the development goals of FM Global (cf. section 3.1).

The Lagrangian particle library allows the user to inject Lagrangian particles e.g. through a cross-section (boundary patch) or at a fixed position in a computational grid. The type of injection can also be user-defined, e.g. a cone representing a sprinkler head, as frequently used by FM Global's fire research division (a conical spray cone is shown in figure 4.9 in section 4.4).

In this thesis, Lagrangian parcels are also injected as a conical spray. However, compared to a sprinkler nozzle, the spray cone is inverted, and the origin is placed into the buoyant part of a thermal plume, induced by the modeled diffusion burner discussed in the previous section 3.3.2. Figure 3.4 shows a sketch of the used configuration. Parcels of different aerodynamic diameters d are injected into the upper, upward flow part of a thermal plume, carrying and dispersing particles along its flow. Particles are tracked by the Lagrangian library and their interaction with any kind of surface, as discussed in section 3.3.1, is recorded.

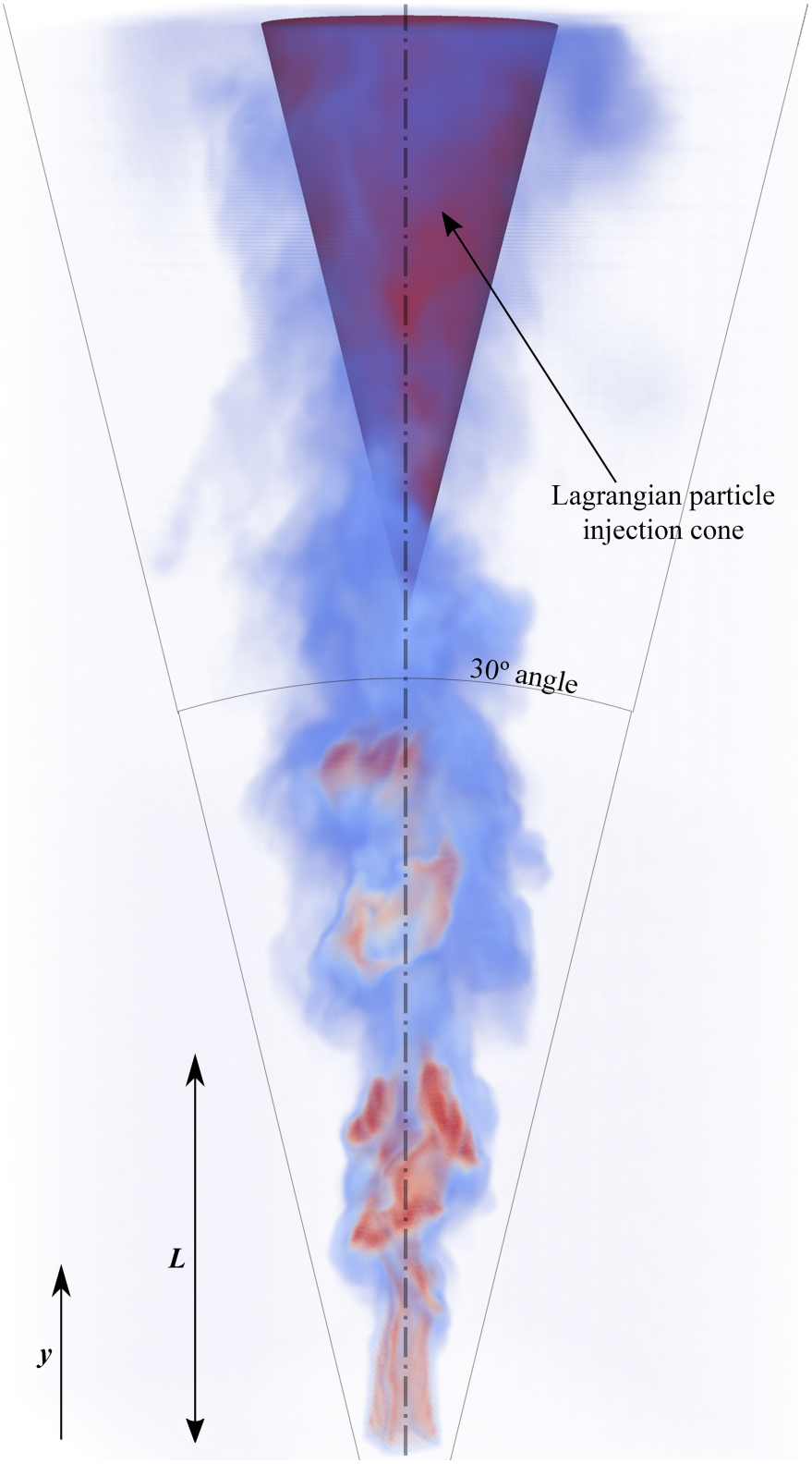

Figure 3.4: Sketch of a thermal plume including Lagrangian particle injection cone (L denotes the mean flame height, y the defined upward axis [67].

For particles different properties can be set e.g. which acting forces to take into account, dispersion, heat transfer, how to allow a phase change, thermal radiation, the formation of a fluid surface film, or, their interaction with surfaces and boundaries. In this thesis the author decided to use gravity and sphere drag, both forces taking into account the aerodynamic diameter of a particle. Only one single phase of particles is assumed, thus no phase change occurs. Parcels are treated as inert and adiabatic. No additional dispersion sub model is used, cf. section 4.4.

Interaction of particles with boundaries such as walls or patches can be set in a rudimentary way:

- local interaction; for each wall or patch an individual condition is chosen, either to stick, to rebound or to escape the domain
- multiple interaction; combination of at least two interaction sub models
- rebound; particles are pushed back upon boundary contact in a user-defined way
- standard wall interaction; a global condition is chosen, either to stick, to rebound or to escape the domain, without differing between different boundaries

None of these interaction mechanisms is able to represent the physical interaction of aerosols with surfaces or obstacles they hit or touch while they are dispersed in a gaseous flow e.g. in air. In reality, aerosols would be receptive to surface adhesion forces (e.g. Van-der-Waals-force), agglomeration, turbulent dispersion, gravitational settling, thermophoresis etc. [81, 82]. Some of these mechanisms can be modeled by other commercial or open source software [83, 84].

Being aware of the difficulties and assumptions discussed above, another simplified approach is proposed as follows. Upon each interaction of a particle with a solid geometry surface i.e. a wall, the surface interaction ID is noted, its interaction time and velocity vector or position is memorized. Particles are allowed to rebound from a surface (ideal elastic rebound), to stick to a surface and to escape from the computational grid (domain) by being dragged along the gaseous flow through a patch open to the environment. By recording and processing this data for each individual particle, one is able to provide information on where, when and how often particles hit a certain surface and in case of escape, where, when and how they leave the domain.

Particle information obtained in the above described way is interpreted towards the radiation protection definitions of surface contamination and release of possibly radioactive aerosols into the environment. The following different particle behaviors are possible

- Particle rebounds always from the same surface up to a user-defined maximum of rebounds, and, its position does not change within user-defined limits: particle is attached to this surface, i.e. contaminating it,
- Particle moves along the flow and reaches, without any rebounding, a volume or a boundary defined for escape: particle is treated as transported to the ambient, i.e. it is released,
- Particle rebounds from more than one surface up to a user-defined maximum of rebounds: particle is traced and attached to the last hit surface, i.e. contaminating it,
- Particle rebounds from more than one surface while moving along the flow until it reaches a volume or a boundary defined for escape: particle is treated as transported to the ambient, i.e. it is released.

Using 10,000 or more arbitrary injected particles, and, based on the four categories of particle behavior defined above, the user is able to qualify and quantify flow-driven aerosol surface contamination and aerosol release to the ambient for a given geometry. By defining the number of particles and the maximum number of rebounds per particle, the user can provide statistical data on the frequency of rebounds, the position of rebounds or the particle velocity vector at rebound time.

3.3.4 Thermal radiation sub model

In general, heat transfer occurs by conduction, convection and thermal radiation. In this thesis only convection and thermal radiation are considered. To model thermal radiation for CFD application, usually a spherical diffusion or a sphere-discretizing ray diffusion, both originating from a heat source, is assumed. it is depending on the emissivity of the emitting surface (e.g. flame), the transmissivity of the medium (e.g. air or smoke) and the absorptivity characteristics of the target surface. Figure 3.5 shows an example adapted to the chosen experimental cavern geometry. A large part of the second sphere is

blocked by the volume of the CMS particle detector, showing the limitation of spherical expansion in this case.

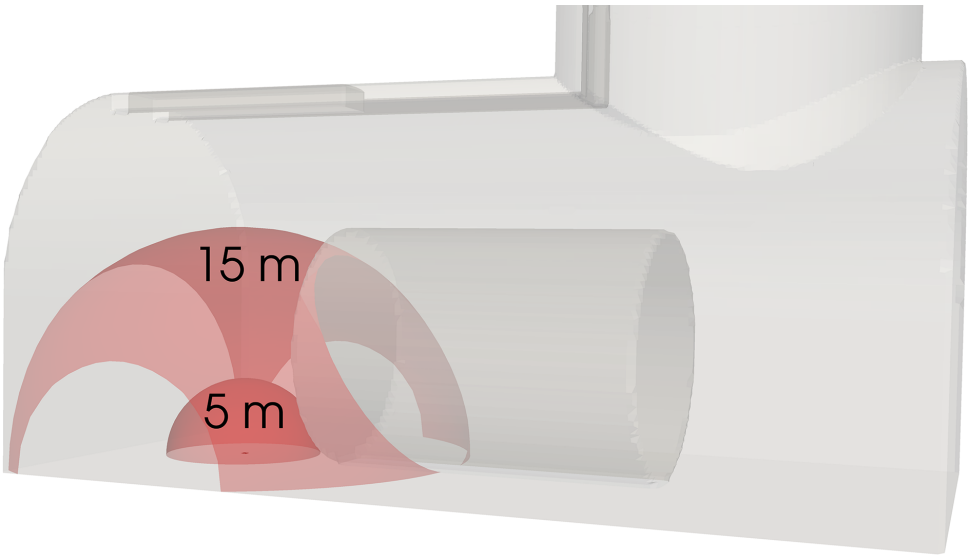

Figure 3.5: Visualization of ideal spherical diffusion by thermal radiation originating from a modeled diffusion burner.

OpenFOAM offers in its default library a few thermal radiation sub models. For application in fire engineering, merely the P1 (based on spherical harmonics) and the finite volume discrete ordinate model (fvDOM) approach are used, [85, 55]. Below, a comparison is shown for the distribution of mean temperatures, averaged over 30 s, of a small two-dimensional (2D) pool fire [86], omitting and using the fvDOM thermal radiation sub model together with a grey mean emission absorption approach, cf. fig. 3.6. Neglecting the thermal radiation sub model results in much higher combustion temperatures. Methane is used in this tutorial case, as idealized fuel following the ideal chemical reaction equation 3.1, cf. section 3.3.2. By omitting the thermal radiative part, temperatures approach the adiabatic flame temperature of methane of about 1950°C. On the contrary, using the fvDOM sub model with a heat release coefficient E_{HRR} of 0.3, 30% of the energy of a diffusion burner is transferred as thermal radiation. This results in a difference in temperature, cf. figures 3.6(a) and 3.6(b).

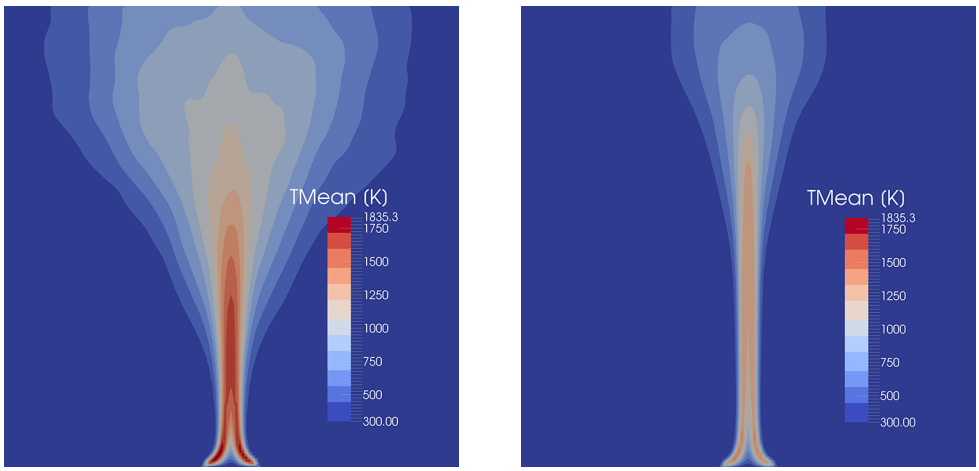

(a) Thermal radiation omitted.

(b) fvDOM sub model used (E_{HRR} = 0.3).

Figure 3.6: Plots of mean temperature without and with the fvDOM thermal radiation sub model.

Thermal radiation emitted from a flame, or in a model from a representation of a flame, is diffusing with distance. To get a quick estimate of the loss between two distanced surfaces of the same size (representing two cell surfaces in a computational grid), one can use the view factor approach [85]. Assuming two equal surfaces, $A_1 = A_2$ with a radiative heat flux $\dot{q}_1''$ set to 100 kW·m^{-2}, the radiative heat flux for the second area $\dot{q}_2''$ is calculated as, cf. eq. 3.2:

$$\dot{q}_1'' = F_{1-2} \cdot \dot{q}_2'' \tag{3.2}$$

where F_{1-2} is the view factor between two limited identical areas. F_{1-2} is expressed in equation 3.4:

$$\begin{aligned} F_{1-2} \;=\; & \frac{2}{\pi XY}\left\{\ln\left[\frac{(1+X^2)\,(1+Y^2)}{1+X^2+Y^2}\right]^{1/2} + X\sqrt{1+Y^2}\tan^{-1}\frac{X}{\sqrt{1+Y^2}}\right. \\ & \left. +Y\sqrt{1+X^2}\tan^{-1}\frac{Y}{\sqrt{1+X^2}} - X\tan^{-1}X - Y\tan^{-1}Y\right\} \\ & \text{with} \qquad X = \frac{a}{c} \qquad \text{and} \qquad Y = \frac{b}{c} \end{aligned} \tag{3.3}$$

Here, a and b denote the length and width of the identical surfaces and c is the distance in-between. Assuming two quadratic areas of 0.4 m x 0.4 m, and a distance of 10 m, F_{1-2} is estimated with $5.1 \cdot 10^{-4}$. Thus $\dot{q}''_2$ is about $0.051\,\mathrm{kW \cdot m^{-2}}$. The calculation leading to this value assumes an ideal environment (e.g. perfect vacuum and black body emitters).

Inside the CMS experimental cavern model, the cavern walls are more than 10 m away from the fire position (i.e. from the diffusion burner inlet). In addition, the massive detector is blocking a direct line of sight to the other end of the cavern and towards the access shaft, cf. fig. 3.5.

Taking into account the geometric limitation of thermal radiation in the chosen model and the computational time frame, the author decided to omit a use of a thermal radiation sub model for the CMS experimental cavern simulations. Additional open questions concerning the accuracy of the fvDOM sub model are discussed in section 4.5. This results in a conservative approach, as the HRR fraction normally converted into thermal radiation is contributing to thermal convection, thus resulting in higher plume velocities and temperatures.

3.3.5 Turbulence sub model

Reviewing the literature on the development and use of fireFoam, cf. section 3.1, one turbulence sub model has been used: the one-equation-eddy approach. It is based on a single equation to solve for the turbulent energy k. Eddies smaller than the used cell size, i.e. sub-grid scale (SGS) eddies are modeled instead of being resolved within the computational grid.

Throughout the thesis calculations, the same turbulence sub model has been used. Figure 3.7 shows an example of the complex flow inside the experimental cavern part illustrated by streamlines , couloured by velocity magnitude $|u_i|$. A thermal plume hits the cavern's ceiling and is deflected towards the cavern walls and the volume between the detector and the ceiling. This configuration has been subjected to further testing by the author, cf. section 4.1. However, the chosen way of modeling turbulence is only one possibility. The reader is referred to e.g. the books of Pope and Grinstein et al. for further discussion on LES modeling [87, 88].

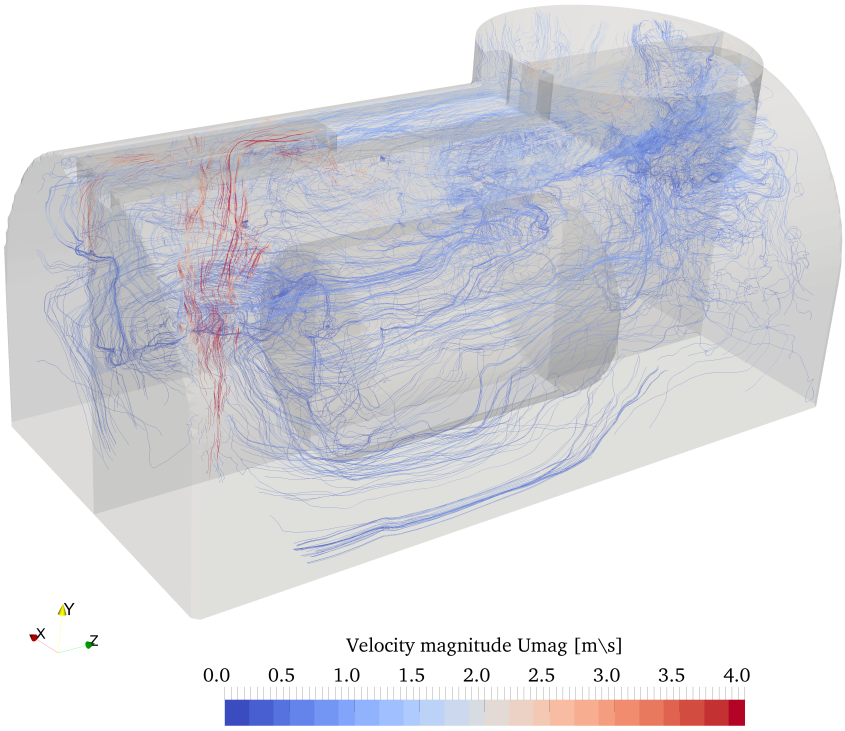

Figure 3.7: Distribution of streamlines caused by fire-induced buoyant flow inside the experimental cavern part.

3.3.6 Initial and boundary conditions

A full set of initial and boundary conditions is given and discussed from mathematical point of view in appendix B.10, including a table giving an overview on the used boundary conditions and surfaces. Their application in order to represent the existing subterranean and surface environment is described below. In case of modeling the air management system or open boundaries, the used conditions are discussed together with the results in chapter 5.

Being permanently vented during operation, the experimental cavern volume is kept at a temperature of about 20° Celsius. This value is taken as initial temperature for the entire volume. All temperature wall boundaries are set to a zero gradient condition. This way the experimental cavern is treated as adiabatic, which is considered as conservative approach.

Besides the species of O_2 and N_2, only CH_4, CO_2 and H_2O are considered. CH_4, CO_2 and H_2O are set to zero as initial condition throughout the geometry. The cavern

is initially filled up with dry air, consisting of 23.3% O_2 and 76.7% N_2. CH_4 is only provided at the inlet patch of the diffusion burner, neglecting the diffusion part at the inlet, cf. section 4.3. CO_2 and H_2O are generated by the combustion process discussed in section 3.3.2 and can only leave the domain by patches open to the ambient. For all five species a zero gradient boundary condition is applied on all walls. On cross-sections modeled open to the ambient, all chemical species are set to a zero gradient condition for out-flowing gas mixture (i.e. gaseous flow leaving the computational domain). Inflow through these cross-sections is modeled by entraining fresh air, i.e. concentrations of 23.3% O_2 and 76.7% N_2 and a mass percentage equal to zero for all other species have been defined.

If not otherwise stated, only the diffusion burner inlet has a set velocity to model a flow of fuel with respect to the chosen heat release rates in section 2.2. All wall cells velocity vectors are set to equal the zero vector, thus no exchange of gaseous fluid between the geometry and the ambient takes place through walls.

For turbulent thermal diffusivity, viscosity and kinetic energy wall functions have been used. For turbulent kinetic energy next to the wall a zero gradient condition is enforced. Turbulent thermal diffusivity α_t next to a surface is modeled by dividing the turbulent viscosity by the turbulent Prandtl coefficient. Finally for the turbulent viscosity Spalding's law is applied [89].

3.3.7 Numerical solver choices

OpenFOAM provides a variety of discretization schemes and numerical solvers to approximate a mathematical model, consisting of one or more partial differential equations (PDE) [79]. A system of partial differential equations has been selected by the author, deemed to be able to provide input on the goals and objectives raised in section 3.2. It is presented in detail in annex B.

In OpenFOAM, the finite volume method (FVM) is applied with second order accuracy in space and time, cf. the thesis of Jasak [90]. Therein, also the discretization process and its related errors are described in detail. Each term of a PDE is discretized, resulting in a set of linear algebraic equations following the generic form of:

$$[a][x] = [b] \tag{3.4}$$

where a is a square matrix, x is a column vector of dependent variables and b is a source vector [79]. Table A.10 provides a list of terms and belonging discretization schemes. For time derivatives the Euler scheme is used, while for gradient, divergence and Laplacian terms mainly Gaussian linear schemes are applied. Interpolations and surface normal gradient terms are treated linearly (also called central differencing, see also [91]).

Following discretization, numerical solvers are calculating solutions based on the set of algebraic equations. For the final calculations of the present work, three different numerical solvers have been used:

- Geometric-algebraic multi-grid (GAMG)
- Preconditioned bi-conjugate gradient (PBiCG)
- Preconditioned conjugate gradient (PCG)

Table A.11 gives an overview on computed variables and their chosen numerical solvers. For pressure p and solid angles I_i of the fvDOM thermal radiation sub model, the GAMG method is applied, while all chemical species Y_i, turbulent kinetic energy k and enthalpy h as well as the velocity u_i are derived by PBiCG. Incident radiation G and density ρ are computed by the PCG method. According to the book of Ferziger and Perić, all three numerical solvers are valid choices to approximate PDE [92].

Starting from the available fireFoam tutorial cases found in OpenFOAM [86] and the FM Global variant [93], the author switched numerical solvers and varied their individual parameters such as tolerance and relative tolerance. However, the final configuration used is similar to the one found for FM Global's Steckler case [93]. This choice is justified, as other variants showed worse performance (in terms of computing time), less satisfying residuals or did not converge at all. Table A.11 also lists the used pre conditioners "Diagonal incomplete-Cholesky (DIC) and "Diagonal incomplete-LU " (DILU). Their influence on the efficiency of numerical solvers has not been subjected to further testing.

Discretizing and solving sets of partial differential equations is a research field on its own. The above mentioned numerical solvers, available in OpenFOAM, have been shortly tested and then used as tools to obtain model results. However, no deeper analysis has been carried to identify the most appropriate configuration (if at all existing). For further description on discretization solvers and their application to CFD, the reader is referred to e.g. the books of Anderson, Ferziger, Perić and Versteeg and Malalasekara [92, 94, 95].

4 Verification and Validation

In this thesis the commonly known expressions "verification" and "validation" are used as follows. Verification is an investigation on calculation accuracy, performed by the author using available analytic or empirical data. Validation is a comparison of model results with experimental data, based on full-scale or adapted small-scale experiments. These definitions are similar to the ones defined in ISO 16730 [96], i.e.

- Verification: process of determining that a calculation method implementation accurately represents the developer's conceptual description of the calculation method and the solution to the calculation method[1],
- Validation: process of determining the degree to which a calculation method is an accurate representation of the real world from the perspective of the intended uses of the calculation method.

Any kind of experimental testing towards a better understanding of thermally-induced flows inside the experimental cavern, next to the CMS particle detector, appears only feasible during long-term shutdown periods. Non-destructive real fire experiments, such as artificial smoke generation by using propane fueled burners of up to 5 MW are in principle possible [97]. However, as the LHC accelerator and its large-scale experiments continue operation, it is likely that radiation protection aspects will prohibit such tests in the near future.

To get a certain confidence in the behavior of the proposed model, different tools of verification are used in the following sections. They provide differences between expectations and model output, towards a quantification of errors (as mentioned in the additional note on the definition of verification in ISO 16730 above).

Research has already been undertaken in terms of reliable use of CFD for fire engineering purposes [16, 98]. Often the assumption is made that a finer mesh provides

[1]Note: The fundamental strategy of verification of computational models is the identification and quantification of error in the computational model and its solution [96].

qualitatively better results. However, in the absence of experimental data only relative error ranges can be provided.

4.1 Mesh independence

A first attempt to identify a suitable computational grid is made by simplifying the problem. Out of the large model of the CMS experiment, a 2D slice is extracted, cf. fig. 4.1. It covers a volume where the thermal plume-induced flow hits the extraction ducts of the air management system.

With a size of 6 m x 18 m in y- and z-direction only, it simplifies calculations, especially with larger number of cells. Uniform cell sizes of 5, 10 and 20 cm have been used for further testing. An airflow with a velocity of $3\,\mathrm{m{\cdot}s^{-1}}$ was set at the left edge in figure 4.2(a), pointing in positive z-direction. The velocity value was chosen based on the flow conditions found inside the experimental cavern volume, cf. figure 3.7.

Each simulation run was carried out over 30 s, dived into 15,000 time steps of 2 ms each. Table A.8 gives an overview on the iterations for pressure p, turbulent kinetic energy k and velocity vector u_i (in y and z coordinate only). For the 5 cm uniform grid about 16.9 iterations per time step have been necessary (13.9 and 9.5 for the 10 and 20 cm uniform grids, respectively).

About two third of the iterations are allocated to solve for pressure. The Courant number is used as a stability criterion [78], being calculated for every time step as $\mathrm{Cou} = \partial t\,|u_i|\,\partial x^{-1}$, ∂t denoting the time step, $|u_i|$ velocity magnitude and ∂x the uniform cell size. Table A.9 shows computed mean and maximum values for Cou, ranging from 0.04 to 0.4.

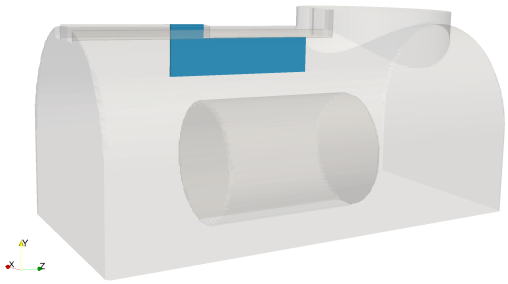

Figure 4.1: Visualization of 2D sub mesh used for mesh independence testing.

Figure 4.2 shows plots of mean velocity magnitude $|u_{i,\mathrm{mean}}|$ for uniform grid sizes of 5,

10 and 20 cm. All three grids indicate the occurrence of an eddy, after the cross-section is reduced by a step (representing the duct of the ventilation extraction unit). A maximum mean velocity magnitude of about 7.34 $\mathrm{m{\cdot}s^{-1}}$ has been found using the uniform 5 cm grid, 6.8 $\mathrm{m{\cdot}s^{-1}}$ for the 10 cm and 5.3 $\mathrm{m{\cdot}s^{-1}}$ for the 20 cm grid. Extent and position of the eddy show qualitatively a good agreement of the three different computational grids.

To quantify the influence of the uniform mesh size on the results, velocity magnitude values have been averaged over 20 s (after initial 10 s in order to minimize numerical oscillation). Mean velocity magnitude values have been extracted along y-direction (89 individuals) at $y = 6.325$ m and $y = 15.025$ m. The former position crosses the center of the eddy, while the latter covers the stable flow region after the eddy. Further values have been analyzed in z-direction (359 individuals), at $z = 4.0975$ m (lower eddy part) and $z = 5.725$ m (inner eddy region). Figure 4.3 shows two exemplary plots of mean velocity magnitude versus coordinate component for the three different grid sizes.

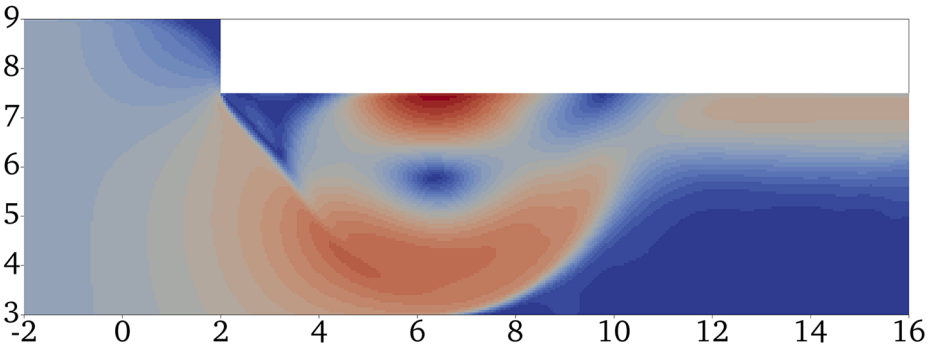

(a) Uniform 5 cm mesh.

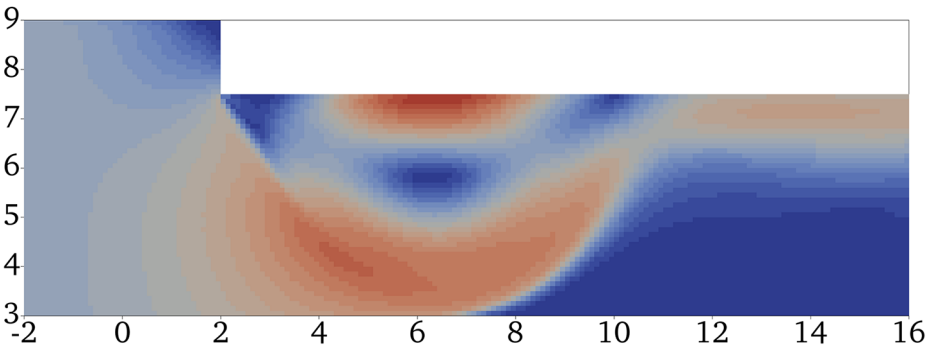

(b) Uniform 10 cm mesh.

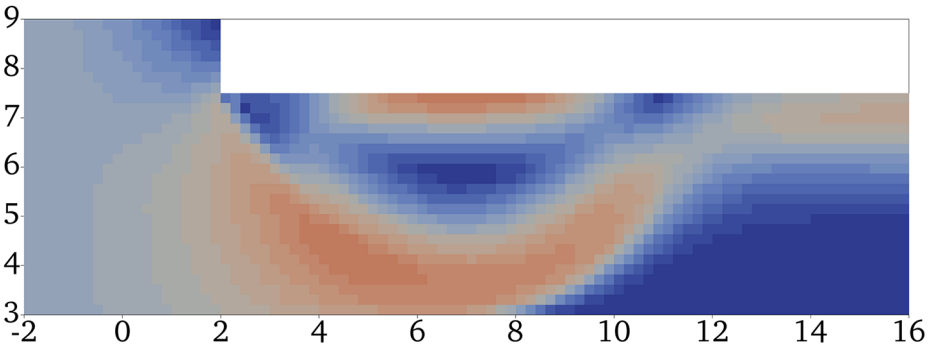

(c) Uniform 20 cm mesh.

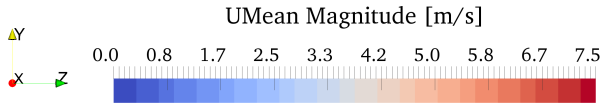

Figure 4.2: Time-averaged mean velocity magnitude plots for 5, 10 and 20 cm uniform cell size (Flow from the left to the right; dimensions in meter).

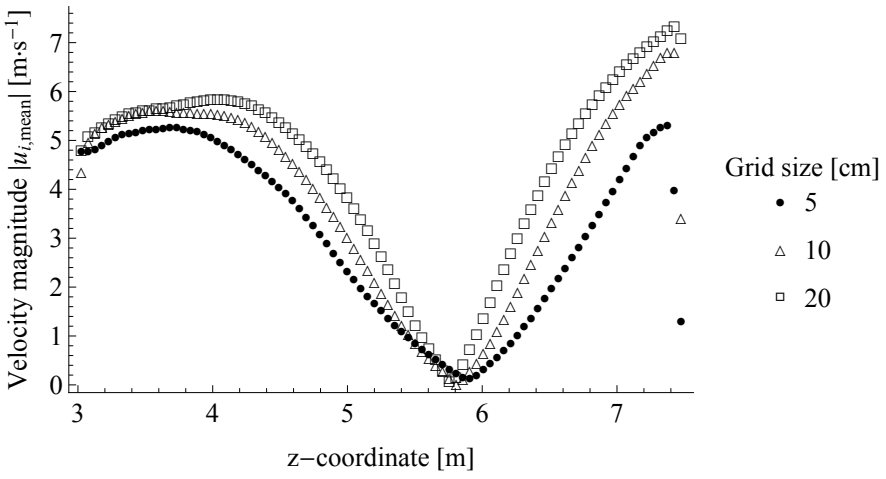

(a) $|u_{i,\mathrm{mean}}|$ at y=6.325.

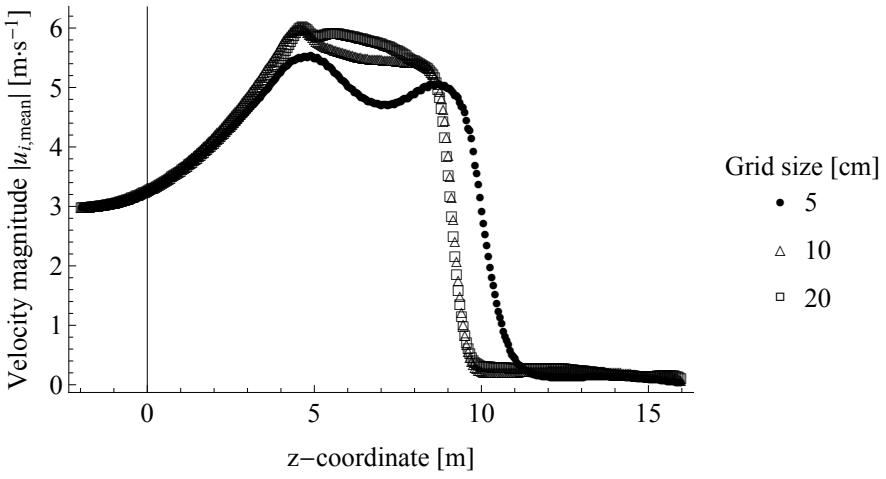

(b) $|u_{i,\mathrm{mean}}|$ at z=4.0975

Figure 4.3: Mean velocity magnitude versus coordinate component at y = 6.325 m and z = 4.0975 m.

Both figures 4.3(a) and 4.3(a) support the good qualititave agreement mentioned above based on figure 4.2. To compare different uniform grid sizes, two mean velocity values (5 - 10 cm; 10 - 20 cm) have been subtracted from each other and divided by the value of the finest grid. As no comparison data sets are available, it is assumed that the finest grid provides the most appropriate result (e.g. as in [15] for the error calculation part). For the comparison between 5 and 10 cm grid sizes, the highest average error of 18.9% ± 3.9 was found at y = 6.325 m. Between 10 and 20 cm cells an average error of 60.1% ± 16.5 has been obtained as highest relative error at z = 4.0975 m. Tables A.4 and

A.5 give an overview on minimal, maximal and average relative errors between 5 and 10 and 10 and 20 cm uniform grid sizes.

Further investigations concerning the spatial discretization have been conducted concerning boundary conditions, cf. section 4.2 and the combustion sub model volume, section 4.3.

4.2 Compliance of initial and boundary conditions

To verify flows through boundary surfaces that have been set up to represent the ambient, coordinate-depending monitoring is used. Further, the minimum and maximum values of different scalar and vector fields have been surveyed, e.g. p, T or u_i. Volume integrals are computed in addition, to record the total change of e.g. a species' concentration or the increase in energy due to combustion.

In case of a closed access shaft, there is no possibility to evacuate the over-pressure from the chosen geometry, built up by modeling an isochoric combustion. Therefore, a small outlet is created, away from the chosen burner position. It extrudes towards a box of arbitrary chosen size, cf. figure 4.4(a). Its floor level and the surface parallel to the cavern wall are defined similar to the cavern walls (no flow condition). The top surface of the box is set to allow outflow only, while its three remaining sides allow in- and outflow of modeled air. This configuration has been chosen in order to establish a free outflow from the experimental volume, as in reality the cavern is not tight and any modeling of a perfectly tight cavern would lead to an internal pressure rise.

Since a first test shows unexpected inflow at the box's top surface, testing is continued using five different combinations, with cell sizes ranging from 10 to 40 cm and either fixed or Courant number controlled time steps. The Courant number is a stability criteria for iterative flow calculation, its implementation in OpenFOAM is defined in [78]. Details on the used mesh refinement are shown in figures 4.4(b), 4.4(c) and 4.4(d). While the box itself is made up from 40 cm cells (fig. 4.4(b)), the first refinement layer results in 20 cm cells (fig. 4.4(c)), followed by a second refinement providing 10 cm cells at the uppermost part of the box (fig. 4.4(d)).

Figure 4.5 shows a plot of mass inflow versus time for the five different combinations mentioned above. In fig. 4.5 $t = 0$ indicates the initialization of the model with the user-defined values. Although in general the mass inflow through the top layer of the

external box occurs on a very low level, different behaviors are shown.

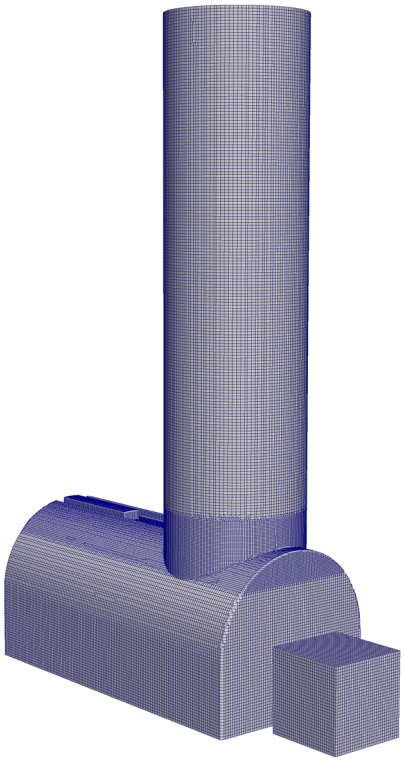

(a) Cavern with attached box.

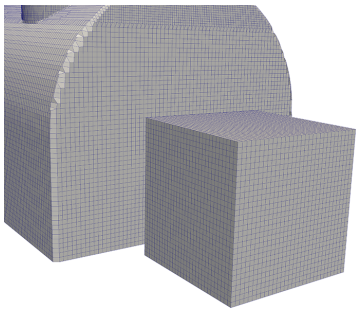

(b) 40 cm cells.

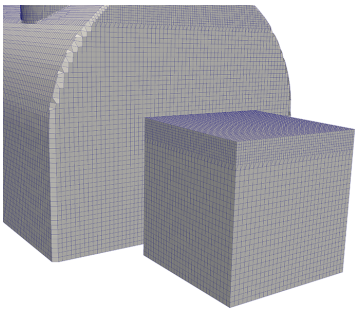

(c) 20 cm cells

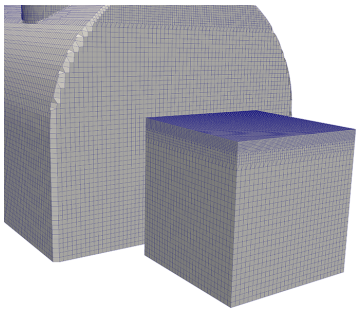

(d) 10 cm cells.

Figure 4.4: Cavern geometry with pressure relief box (a). Detail views show: no refinement (b), 1st top layer refinement (c) and 2nd top layer refinement (d).

Comparing the tests with fixed and varying time steps, it can be shown, that the fixed time step cases perform better in terms of lower inflow. Here, better is defined by registering the lowest mass inflow at a boundary surface that is set to have zero mass inflow. Comparing further the fixed time step tests with each other, a one or two step

refinement does not reduce significantly the inflow (but increases required computational effort). Based on the tests performed, for each full model run presented in chapter 5 the initial box of 40 cm cells is used. Assuming a maximum inflow of modeled air of about 0.008 kg·s^{-1} compared to the preset zero value, an error below 1% is made under worst flow conditions at the discussed boundary surface.

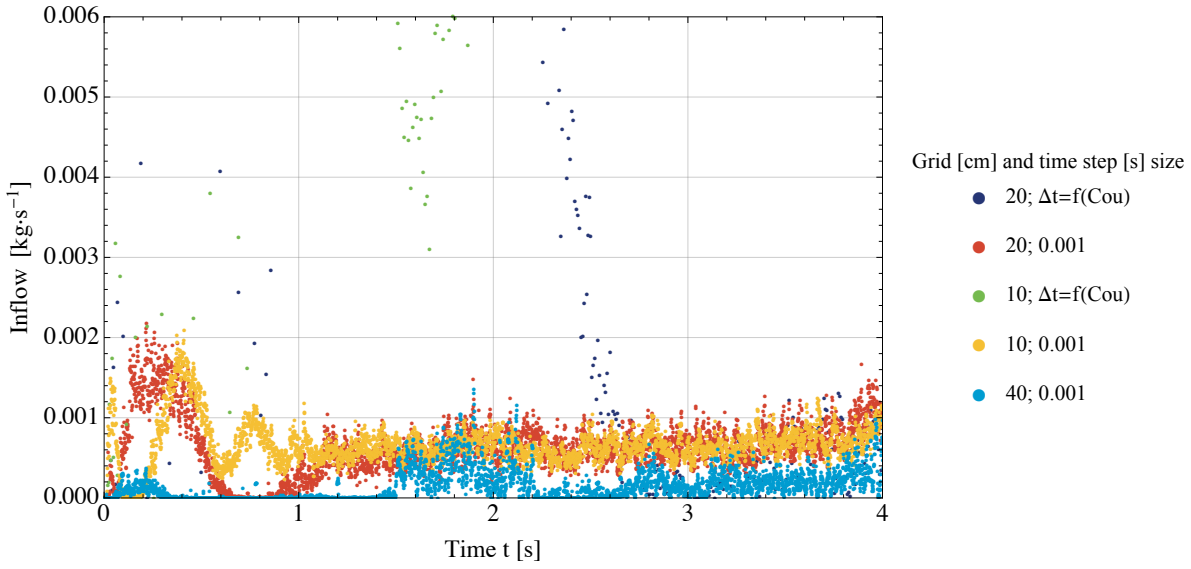

Figure 4.5: Mass inflow versus time t through an outflow-only defined surface (Centimeter value denotes the uppermost layer cell size. Where Δt varies, Cou = 0.5 is used).

In addition to the part of the geometry questioned in detail above, all other surfaces are monitored. Each comply with the user-defined settings, no other unintended flows are found.

4.3 Combustion sub model

Based on one or multiple series of fire experiments, several different empirical correlations related to thermal plumes have been derived in the past. Today they are very often simply adressed as "plume equations". A good overview can be found in the thesis of Knaust [99]. Different equations allow the calculation of e.g. plume temperature, axial plume velocity, plume mass flow and the plume radius. For this thesis the author decided

to use the equations presented by Heskestad et al. [100, 67]. Initially this decision was based on the versatility of Heskestad's set of plume equations, e.g. beside mean excess temperature and plume velocity also the fraction of heat release rate to be emitted as thermal radiation could be taken into account, the plume radius could be estimated etc. However, in the final verification test case presented below, only mean excess temperature and the plume velocity are used, eq. 4.1 and 4.2.

$$\Delta T_0 = 9.1 \left(\frac{T_\infty}{g c_\mathrm{p}^2 \rho_\infty^2} \right)^{1/3} \dot{Q}_\mathrm{c}^{2/3} \left(z - z_0 \right)^{5/3} \tag{4.1}$$

$$u_0 = 3.4 \left(\frac{g}{c_\mathrm{p} \rho_\infty T_\infty} \right)^{1/3} \dot{Q}_\mathrm{c}^{1/3} \left(z - z_0 \right)^{-1/3} \tag{4.2}$$

In equation 4.1 ΔT_0 is the difference between plume temperature and ambient temperature T_∞. ρ_∞ and c_p are the ambient density and specific heat capacity (of air), g is the gravity force in negative z-direction, $\dot{Q}_\mathrm{c}$ the fraction of the heat release rate , z the elevation above the fire source and z_o the elevation of the virtual origin above the fire source. In eq. 4.2 u_0 denotes the axial plume velocity. Together with some additional empirical correlations, e.g. for mean flame length and the virtual origin, the user can finally calculate plume velocities and temperatures along an axis (i.e. the center-line shown in fig. 3.4, section 3.3.3). Throughout this thesis, the plume axis is pointing in positive y-direction (instead of positive z-direction).

Following calculations of plume mean excess temperatures and velocities using the mentioned equations, fireFoam is used to compute meshes of 4.4 m x 10 m x 4.4 m, based on the initial simulation series done by Wang et al. [66]. The author has chosen to test quasi-steady convective heat release rates of 0.5, 1 and 1.5 MW, based on the fire load analysis for an electrical cabinet, cf. section 2.2.2. A goal of this study is to identify a suitable cell structure for the thermal plume inside the CMS experimental cavern, providing not more than 20% quantitative difference between Heskestad's plume equations and the simulations. The latter is derived from earlier results, balancing computational grid resolution, desired accuracy and available computing resources.

All test cases are based on the small pool fire 3D tutorial case that is distributed with OpenFOAM. Figure 4.6 shows an example mesh with 40 and 10 cm cells (outer and inner

parts, respectively). This type of two-step mesh refinements was inspired by the much more complex approach of Chatterjee et al. [68].

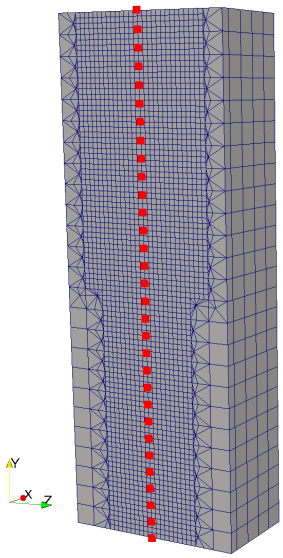

Figure 4.6: Plume equation test mesh with 31 sampling points.

Data sets for plume mean excess temperatures and plume velocities, derived from both, empirical correlations and numerical calculations, have been plotted against each other, using the y-coordinate to align the data. Computed values have been taken from simulations running quasi steady-state combustion for 30 s, where plume mean temperature and plume mean velocity were recorded over the second half of 15 s. This sampling behaviour was suggested by Prateep Chatterjee in order to avoid the influence of numerically-induced oscillations caused by the initialization of a simulation [101]. As the resolution of the mesh is not capable to resolve the complex processes and phenomena occurring inside or next to the combustion or flame, values taken from this volume are not representative. The region of the mean flame length, denoted with L in figure 3.4 is therefore omitted in all plots. The reader is reminded that the goal of this model is to represent a thermal plume, not the combustion process or in reality occurring flames, cf. section 3.3.

In figure 4.7 a comparison is made for a convective heat release rate of 1 MW (no thermal radiation sub model used) using five different mesh sizes ranging from 2.5 to 40 cm. If calculated and computed velocities would match 100% they would follow the

grey line in fig. 4.7. Deviations by ± 10% would stay within the green, deviations by ± 20% within the red lines. The most right data point in each plot denotes the lowest y-axis value (just above the mean flame height) while the most left data point represents the uppermost y-axis value. Thus, only the thermal plume part above the intermittent flame region is taken into account here. The same principle is applied for the plots of mean excess temperatures, cf. figure 4.8.

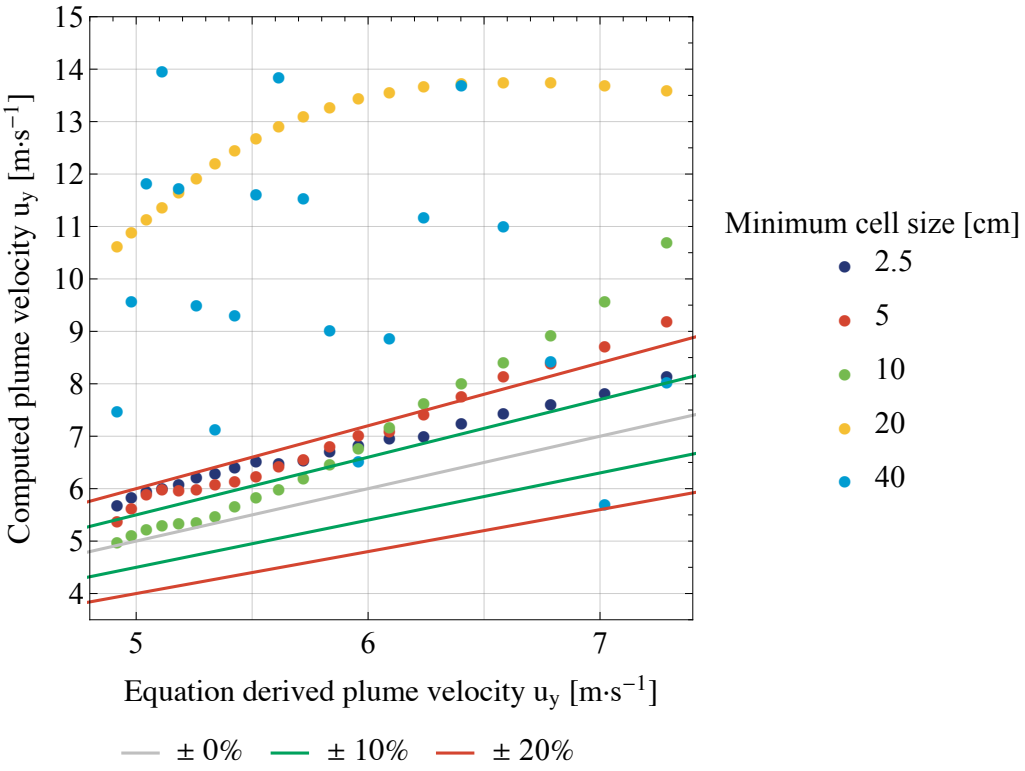

Figure 4.7: Comparison plot between computed and equation derived plume velocities for differently sized plume region cells using a convective HRR of 1 MW.

From figure 4.7 it follows that only a mesh refinement down to 2.5 cm provides plume velocities that fulfill the above set requirement of complying within 20% difference to the plume equations. Using 5 or 10 cm cells shows 20% difference or even below, but only for the most upper part of the considered thermal plume (i.e. equation derived plume velocity values up to 6 m·s^{-1} for 5 or 10 cm cells). A similar behavior is found for the equation based plume mean excess temperature plotted against the numerically computed temperature in figure 4.8. Only the upper plume part modeled with a 2.5, 5

or 10 cm grid is able to stay below the 20% difference threshold (i.e. equation derived plume temperature below 400 K in fig. 4.8).

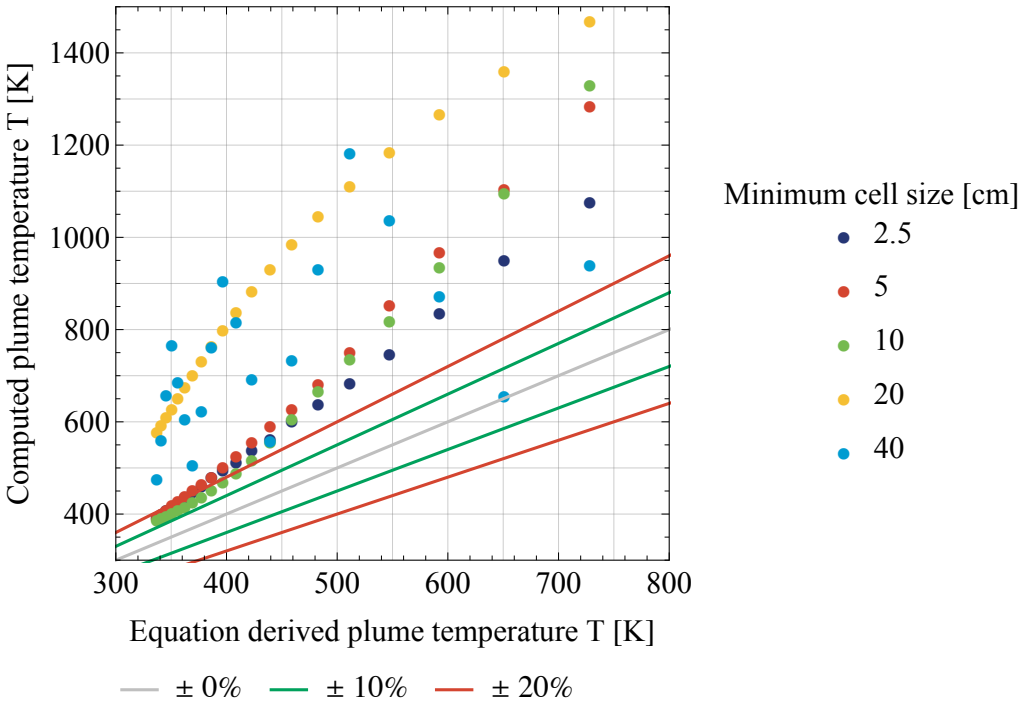

Figure 4.8: Comparison plot between computed and equation derived plume temperatures for differently sized plume region cells using a convective HRR of 1 MW.

Large quantitative differences in the results given for different cell sizes, ranging from 40 cm down to 2.5 cm, are found in figures 4.7 and 4.8. In both plots, scattered values have been obtained for temperature and velocity using 40 cm uniform cells. Only from 20 cm and below, resulting values seem to follow a trend. However, results obtained from a 20 cm grid are still way off the 20% margin defined above. Velocity values in fig. 4.7 range up to the double of their 10 cm counterparts (on the "computed plume velocity" axis), while 20 cm grid derived temperatures in fig. 4.8 are approximately 200 K above the values computed by using a 10 cm grid (on the "computed plume temperature" axis). This behavior is caused by the mesh dependency of the combustion process, together with the chosen combustion sub model. Model results based on sets of partial differential equations can only be approximated. It depends on the accuracy of the computational grid to which extent an approximation matches expectations.

A modeled infinite fast chemistry combustion within one cell having a volume of $0.4^3\,\mathrm{cm}^3$ will provide only one temperature value (and velocity vector) based on the energy released in its volume. If the same overall volume is represented by 10 cm uniform cells, 64 smaller volumes of $0.1^3\,\mathrm{cm}^3$ will provide 64 different results, depending and interacting with each other. Therefore, a comparison with the above mentioned plume equations is used here in order to identify a model degree (or grid refinement level) being capable to represent the physical phenomenon of a buoyant thermal plume up to a certain extent.

Additional tests have been carried out for 0.5 and 1.5 MW heat release rates, using the same procedure. Results similar to those in figures 4.7 and 4.8 have been obtained (not shown). Based on the results presented here, the injection source for the Lagrangian particles discussed in section 4.4 below, is centered 9 m above the inlet of the modeled diffusion burner for the 1 and 1.5 MW cases (while it is 7 m for the 500 kW cases), in order to ensure particle injection, acceleration and deposition within an upper plume part being within 20% range of the plume equations.

4.4 Lagrangian parcel sub model

In FM Global's fireFoam solver the Lagrangian particle framework is frequently used to model sprinkler or water mist nozzles, cf. section 3.3.3. The same sub model is used in this thesis by modeling an "inverted sprinkler" spray cone, that injects parcels (ideal spheres of different aerodynamic diameters) into a the center of a thermal plume. All parcels injected that way follow the plume-induced flow for a certain time, depending of their size and mass. They represent the cloud of aerosols that is usually created by combustion and emitted as hot air or smoke.

To analyze the dependency of the Lagrangian parcels with respect to mesh size, a parcel spray is injected in a box while neglecting any kind of additional fluid flow or parcel forces such as gravity or sphere drag. Only the computational grid, a structured rectangular mesh was set to use 5, 10 and 20 cm cells. Once the spray had evolved as shown in figure 4.9, the position vector data of the parcels of the same time step was compared. The maximum deviation in x, y and z position found, comparing 5 and 10, 5 and 20 as well as 10 and 20 cm cells are given in table A.6. The results show an influence of mesh size of about 10^{-6} m on the parcel position, which is negligible.

Contrary to the mesh independence, parcels are prone to the size of the fluid phase time step Δt. For each fluid time step a certain number of parcels is injected into a chosen domain, e.g. dividing 10 s by Δt = 0.2 s will lead to 50 injections. Assuming a total number of 10,000 parcels, each injection will add 200 parcels. Hence, the smaller the fluid phase time step Δt the higher the number of injections with a smaller number of parcels injected. This behavior is shown in figures 4.9(a) to 4.9(d) showing a cone injection in ideal conditions as already discussed at the beginning of this section. A similar time step dependency has not been found for the shape of the particle cone perpendicular to the injection axis.

To test the influence of the total number of particles on the results in terms of counting the number of parcels released or deposited on a certain surface, the total number of particles is varied from 10,000 up to 100,000 parcels. Results for release and deposition are shown in tables A.33, A.34, A.41, A.42, A.43 and A.44. Based on the percentages, the maximum deviation is in the order of 5%.

Further simple tests have been carried out to verify the used cone angle, and the particles forces taken into account, gravity and sphere drag. They have been found to work as intended, so the results are not discussed here in detail for the sake of brevity.

4.5 Thermal radiation sub model

In addition to the explanations given in section 3.3.4, the fvDOM thermal radiation sub model is subjected to further testing. Repeating and adapting a test case already known [16, 102], a rectangular geometry (box) of 2.8 x 2.8 x 1.2 m is used. It fits the 40 cm cells mainly used in this thesis. Inside, a hot surface irradiates a defined measurement surface at the bottom. All other physical phenomena are neglected. Only the number of solid angles (the resolution used by the fvDOM sub model to model thermal radiation) and the uniform mesh cell size is varied. Together with an analytically obtained value based on the view factor approach, the precision of a given uniform mesh-solid angle combination is obtained, cf. fig. 4.10.

(a) $\Delta t = 0.2\,\mathrm{s}$

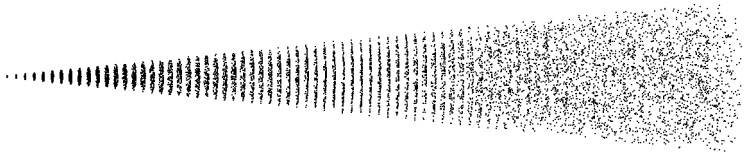

(b) $\Delta t = 0.05\,\mathrm{s}$

(c) $\Delta t = 0.005\,\mathrm{s}$

(d) $\Delta t = 0.001\,\mathrm{s}$

Figure 4.9: Influence of time step size on particle spray cones in ideal conditions.

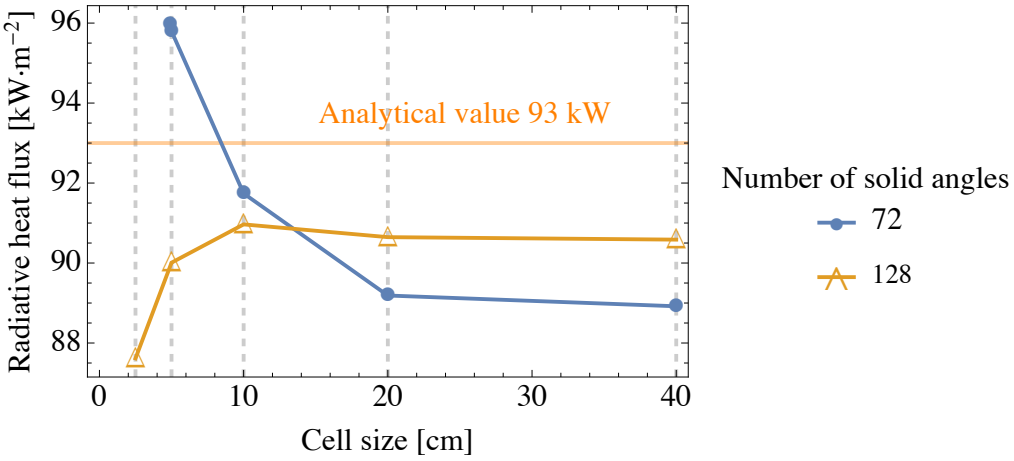

Figure 4.10: Thermal radiative heat flux as a function of uniform mesh size and total number of solid angles.

In table A.7 an overview is given on the numerically obtained radiative heat flux values and their individual deviation from the analytical target value. The absolute maximum deviation is 7.3% for 72 solid angles and 5.8% for 128 solid angles.This dependency of solid angle-mesh combination is still under investigation [103].

Neglecting thermal radiation in the present model results in a relative error of about 30% (which is a rule of thumb value based on fire testing [104]).

4.6 Verification matrix and conclusions

Besides building up a numerical model, using simplifications and being aware of the limitations of such an approach, individual and methodical errors made by the author cannot be excluded. Individual errors may occur e.g. due to wrong configuration of a simulation or using a wrong assumption.

In addition, methodical errors may occur, especially during post-processing of model data. A mathematics application is used in the present work, in order to automatically process e.g. the distribution of surface ID among particles of a certain aerodynamic diameter. To do so, the data is imported and then manipulated by multiple vector operations. Thus, small errors assigning a vector or using an operator may result in wrong output, without the user being aware. A quantification of human error is beyond the scope of this thesis. The reader is refered e.g. to chapter 14 of the work of Lees,

considering a wide range of human errors, their qualification and quantification [105].

Table A.12 provides a verification matrix to assess the accuracy of the simulations carried out for this thesis. It is based on multiple test cases discussed in this chapter. Each relative error has to be considered on its own, as all sub models and routines within an application are related to each other [106, 16, 98]. Therefore, it is the whole matrix of relative errors, that has to be taken into account referring to the results presented in chapter 5.

5 Results and discussion

First, results on the conventional safety goals defined in section 3.2 are presented in section 5.1, while aerosol release and deposition data is presented and discussed in section 5.2. Results are given for the particle local interaction sub model and the particle local interaction rebound sub model, providing details on particle release and interaction with surfaces (deposition).

5.1 Fire-induced flow results for the CMS experimental cavern

Three final geometry configurations have been selected: cavern closed, cavern open to the surface level and cavern open to the surface level and neighboring cavern, cf. section 3.3.1. As for each geometry configuration, parameters related to the thermal plume flow are varied, too, each configuration is represented by its individual part, i.e. in sections 5.1.1, 5.1.2 and 5.1.3. Instantaneous contour plots are used where appropriate to allow qualitative comparison. Countour plots showing a cross-section of the whole CMS experimental cavern are cut on the center plane of the diffusion burner. Scalar values are scaled to allow comparison. Upper limits denote always "value and values higher than" unless otherwise specified. Due to constraints in memory, post-processed time steps cannot be always aligned in the same way.

5.1.1 Closed cavern - air management system use

First, the impact of a closed cavern without the use of its air management system is assessed. In order to do so, two different scenarios with 1 MW and 1.5 MW steady HRR have been run for 20 minutes and 14 minutes, respectively. In both cases the same amount of energy discussed for an electrical cabinet is introduced into the model volume, due to the difference in simulation time and heat release rate. Figures 5.1 and 5.2 show

the belonging instantaneous temperature and velocity contour plots.

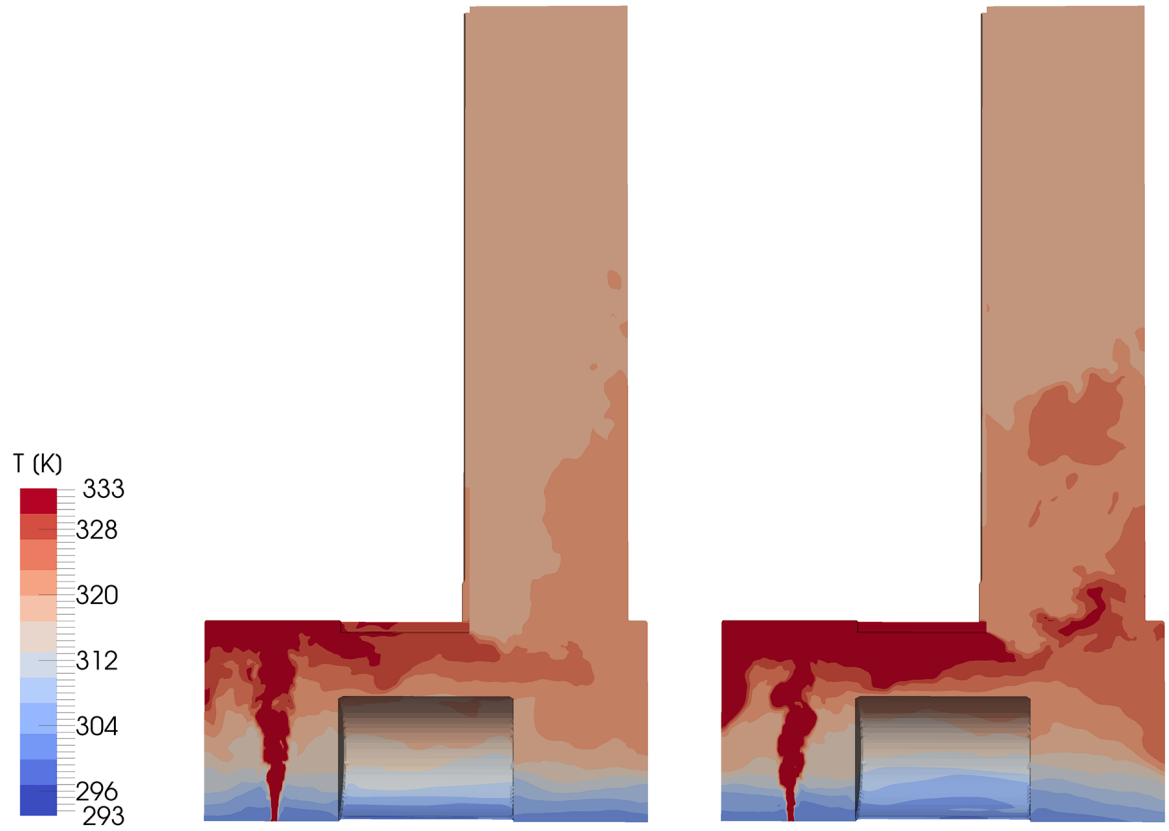

(a) 1 MW, 20 min. (b) 1.5 MW, 14 min.

Figure 5.1: Instantaneous temperature contours inside the closed experimental cavern volume.

From the temperature plot in figure 5.1, it can be shown, that the temperature safety objective (not more than 60°C) from section 3.2 is met. Although in the case of the 1.5 MW steady HRR the volume between the cavern ceiling and the detector is nearly saturated with a layer of 333 K or more, cf. fig. 5.1(b), the detector does not submerge in this layer. In both cases, the access shaft acts as storage volume.

Comparing the velocity magnitudes of both cases, only a little difference in the amount of cells that are marked with a value of 6 $m \cdot s^{-1}$ or more, cf. fig. 5.2(a) and 5.2(b) is observed. In both cases, the plume regions show higher velocity values, than could be found elsewhere in the closed cavern geometry, especially below the mean flame height limits. However, as already pointed out in section 4.3, care was taken to get a reliable

representation of the emerging plume, not the flaming fire region itself.

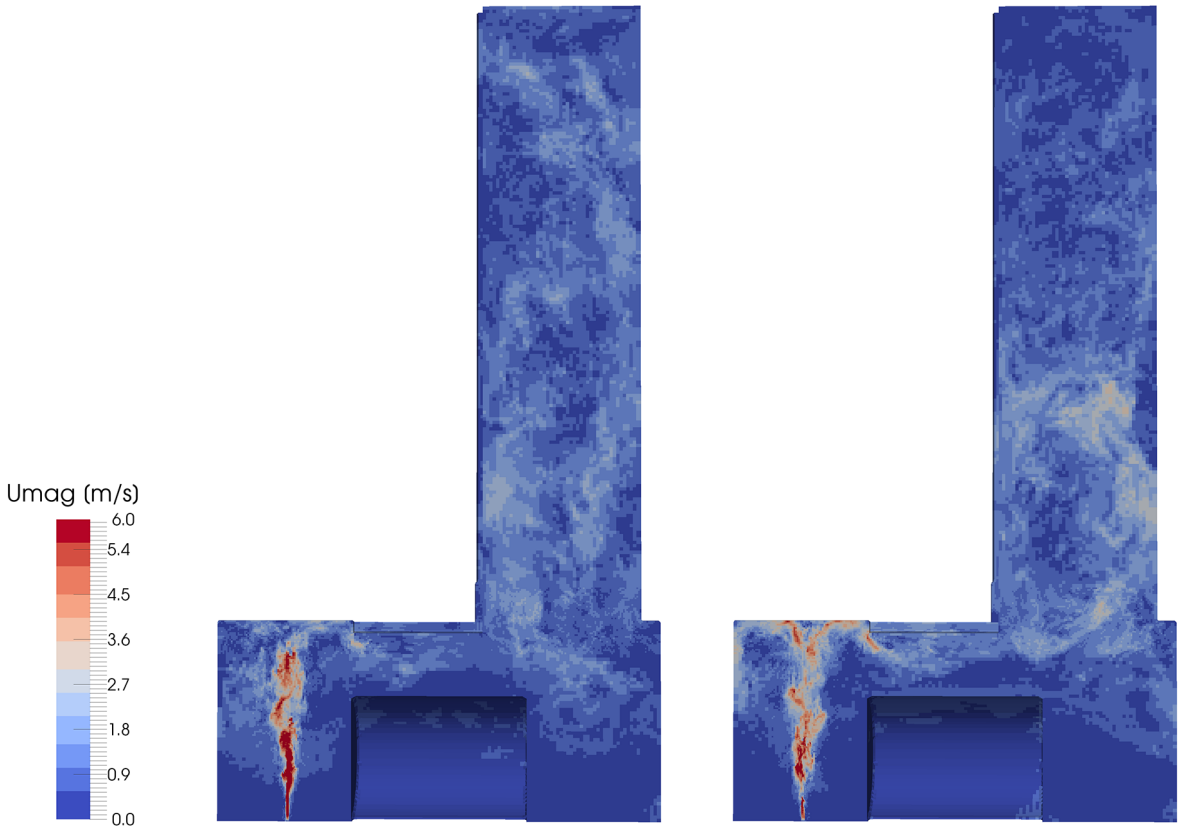

(a) 1 MW, 20 min. (b) 1.5 MW, 14 min.

Figure 5.2: Instantaneous velocity magnitude contours inside the closed experimental cavern volume.

Two additional calculations have been carried out using the 1.5 MW model to evaluate the air management system (in extraction mode only), delayed by two minutes with respect to the time the diffusion burner reaches its maximum preset HRR value. Earlier results have shown, that the highest volume flow rate (extraction mode, 90,000 $m^3 \cdot h^{-1}$) of the CMS experimental cavern's air management system has only little impact on the stratification inside the cavern, compared to the medium one [107]. It is therefore neglected. Figure 5.3 shows the state of instantaneous temperature after 14 minutes, using low volume flow (22,500 $m^3 \cdot h^{-1}$) or medium volume flow (45,000 $m^3 \cdot h^{-1}$) extraction. In both cases, the temperature layer shown as "333 K and above" is reduced, compared to the case without extraction cf. fig. 5.1(b). Further, a layer of unaltered air is noticed

in both, low and medium extraction cases.

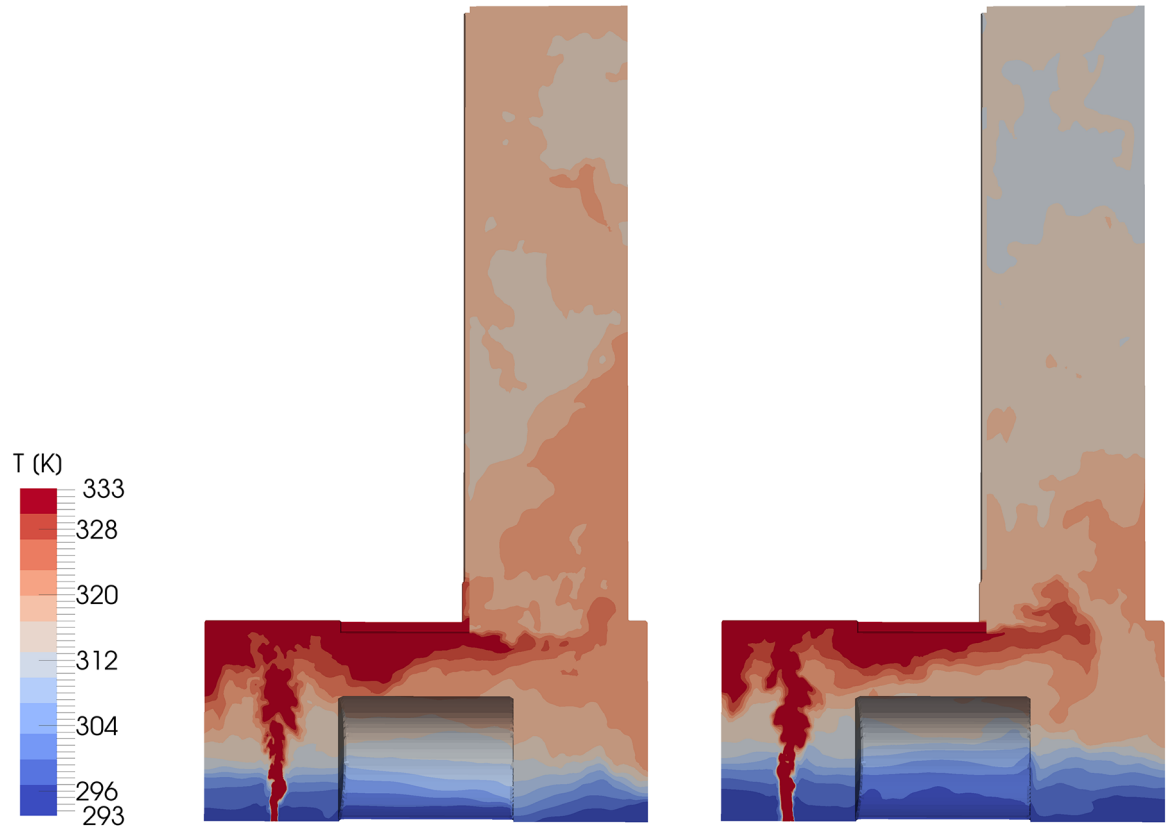

(a) Low extraction volume flow. (b) Medium extraction volume flow.

Figure 5.3: Instantaneous temperature contours inside the closed experimental cavern volume modeling low and medium extraction mode of the air management system (1.5 MW, 14 min).

Comparing the velocity magnitude contours shown in figures 5.4(a) and 5.4(b) with figure 5.2(b) higher velocity magnitudes are observed next to the extraction cross-section. Figure 5.4(b) indicates a flow next to the cavern wall, far-side from the diffusion burner, on floor level. This local increase in velocity is due to external fresh air drawn in passing through the attached volume for pressure relief discussed in section 4.2. Additionally supplied air does not enforce combustion, as it would be the case e.g. in a compartment fire in a residential building. The large total cavern volume provides sufficient air (oxygen) supply for the chosen scenarios and thus, they are independent from additional air entrainment.

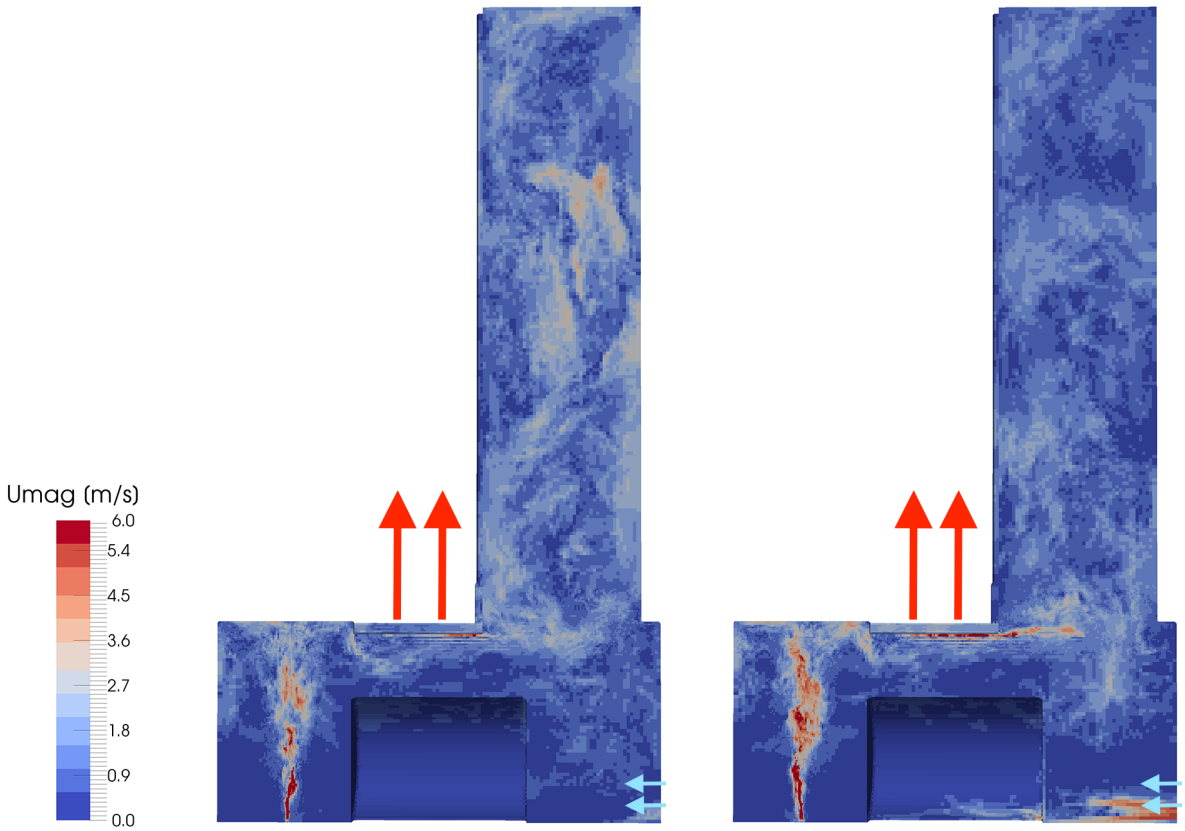

(a) Low extraction volume flow.

(b) Medium extraction volume flow.

Figure 5.4: Instantaneous velocity magnitude contours inside the closed experimental cavern volume modeling low and medium extraction mode of the air management system (1.5 MW, 14 min, red arrows indicate extraction units, blue arrows fresh air entrainment).

To assess a worst case of two electrical cabinets burning next to each other, another variant of the 1.5 MW model is run, doubling the duration of quasi steady heat release rate. Figure 5.5 shows the resulting instantaneous temperature and velocity magnitude contours. Due to the additional time and energy contribution, the temperature level inside the cavern reaches nearly everywhere 333 K or more. In fact, the detector starts to become submerged only three to four minutes after the state shown in figure 5.1(b).

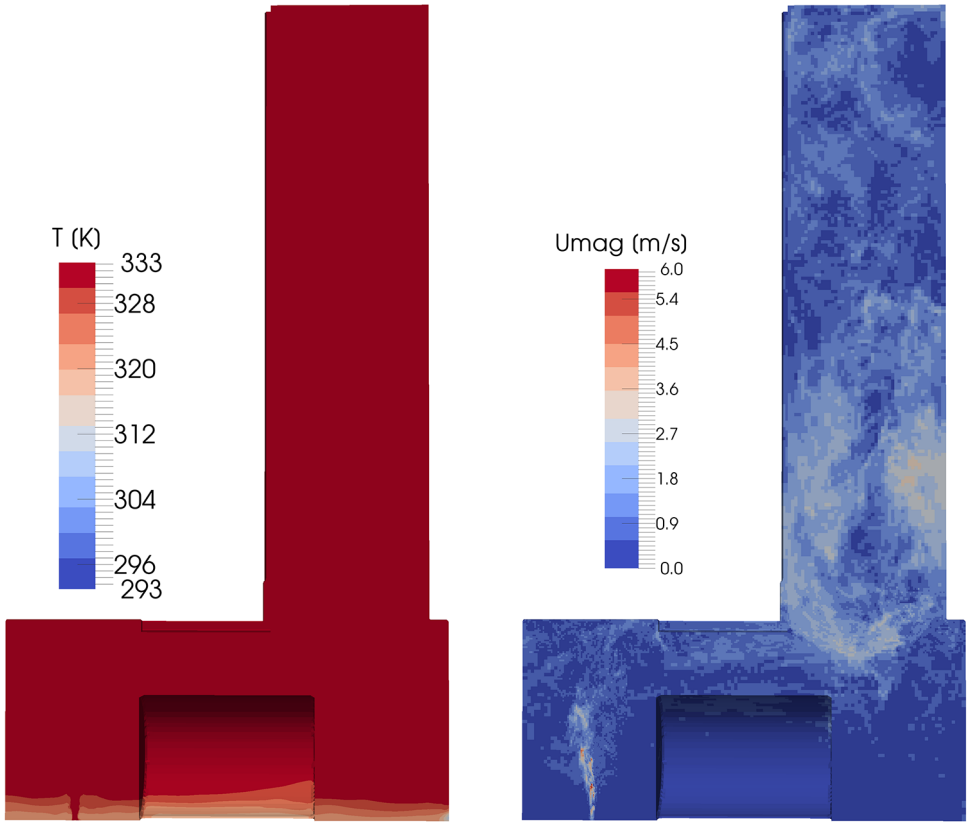

(a) Temperature.

(b) Velocity magnitude.

Figure 5.5: Instantaneous temperature and velocity magnitude contours inside the closed cavern volume (1.5 MW, 28 min; without air management system).

5.1.2 Open access shaft

During short and mid-term intervention and maintenance periods, the concrete plug sealing the access shaft of the CMS experiment is removed. An emerging thermal plume will still move along the cavern ceiling before it continues into the access shaft and exits it at surface level. Figure 5.6 shows the instantaneous temperature distribution for the already described 1 MW and 1.5 MW scenarios. Comparing figures 5.6(a) and 5.6(b) with their counterparts in the closed configuration (see figure 5.1) an obvious difference is found. As the hot air can leave the volume, there is less stratification inside the access shaft and thereby less dense stratification below the cavern ceiling.

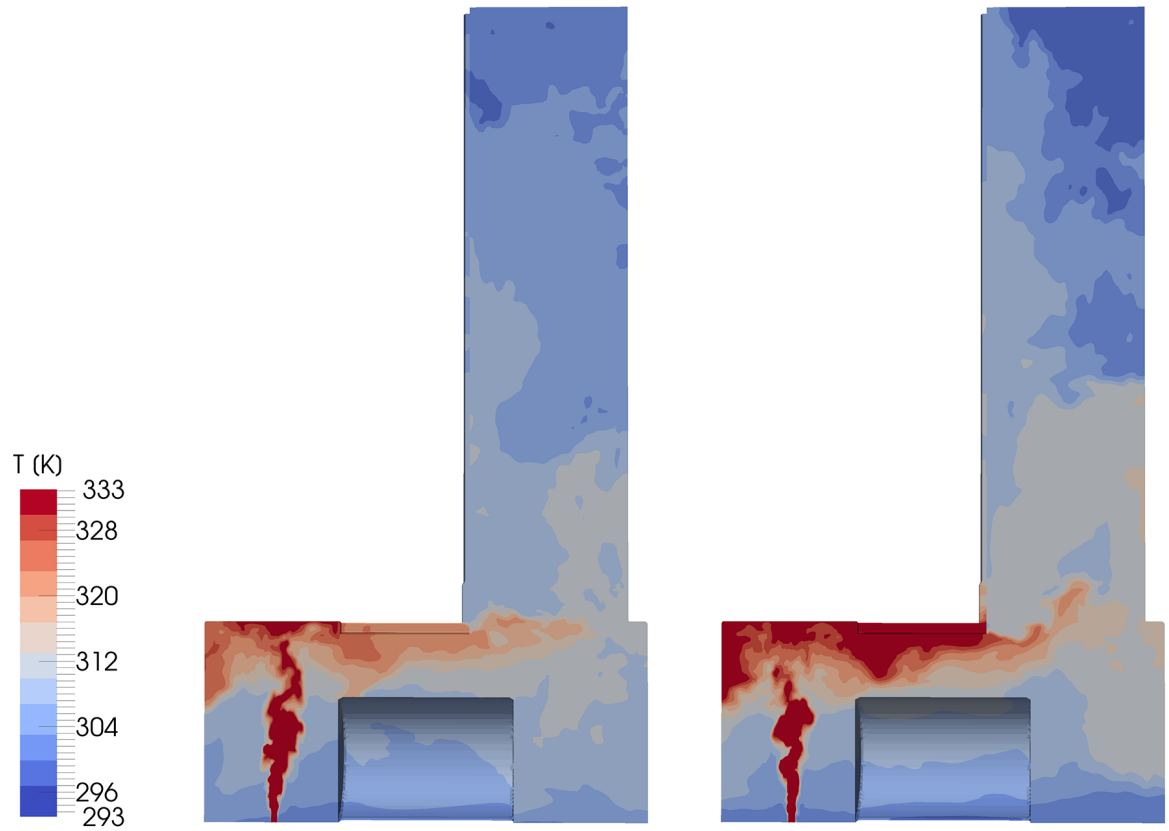

(a) 1 MW, 20 min. (b) 1.5 MW, 14 min.

Figure 5.6: Instantaneous temperature contours for the cavern volume open towards the surface level (1 MW, 20 min and 1.5 MW, 14 min).

Although the concrete cover of the access shaft is removed, the flow inside the cavern volume is rather unaffected, cf. figures 5.7 and 5.2. Emerging from the combustion zone above the diffusion burner inlet, the thermal plume is hitting the cavern ceiling, passing below and entering the access shaft. This observation is a further sign of a well working model set-up, as there should not be any disturbance inside the cavern volume due to the change in geometry at the the top of the access shaft.

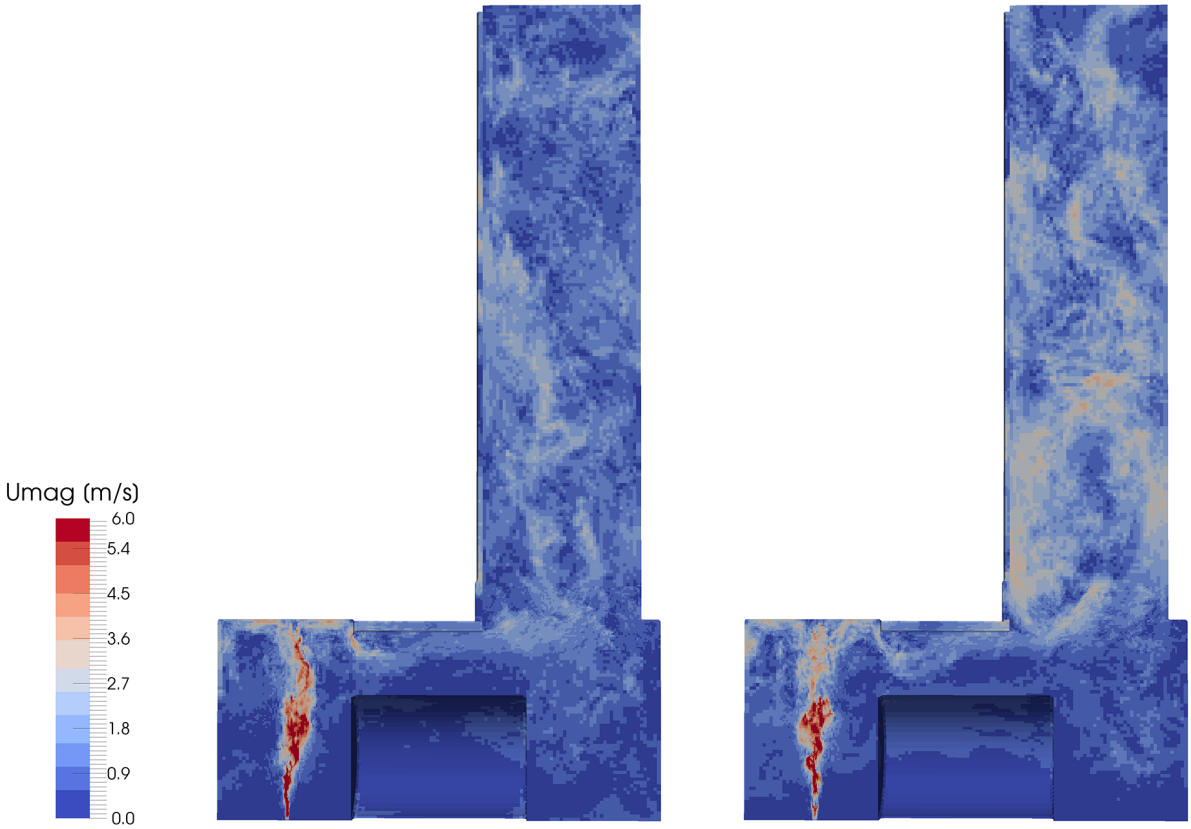

(a) 1 MW, 20 min. (b) 1.5 MW, 14 min.

Figure 5.7: Instantaneous velocity magnitude contours for the cavern volume open towards the surface level (1 MW, 20 min and 1.5 MW, 14 min).

5.1.3 Open access shaft and connection to neighboring service cavern

During long-term shutdown periods, a material passage is established between the CMS experimental and service cavern by removing a large concrete block. Together with a dedicated air management scheme, this negates the pressure difference of about 20 Pa w.r.t. to the ambient, which is usually kept between the two caverns during operation. Using a modified geometry and the 1 MW and 1.5 MW fire scenarios, one obtains the instantaneous temperature plots shown in figure 5.8. Here, the fire position is varied to represent the worst position in terms of release of aerosols, as the thermal plume rises straight into the access shaft without being delayed by the cavern ceiling cf. section 5.2

below. Comparing figures 5.8(a) and 5.8(b) with their predecessors (fig. 5.1 and 5.6) it can be shown, that in terms of temperature development during the different fire scenarios, this configuration has the least impact on the detector.

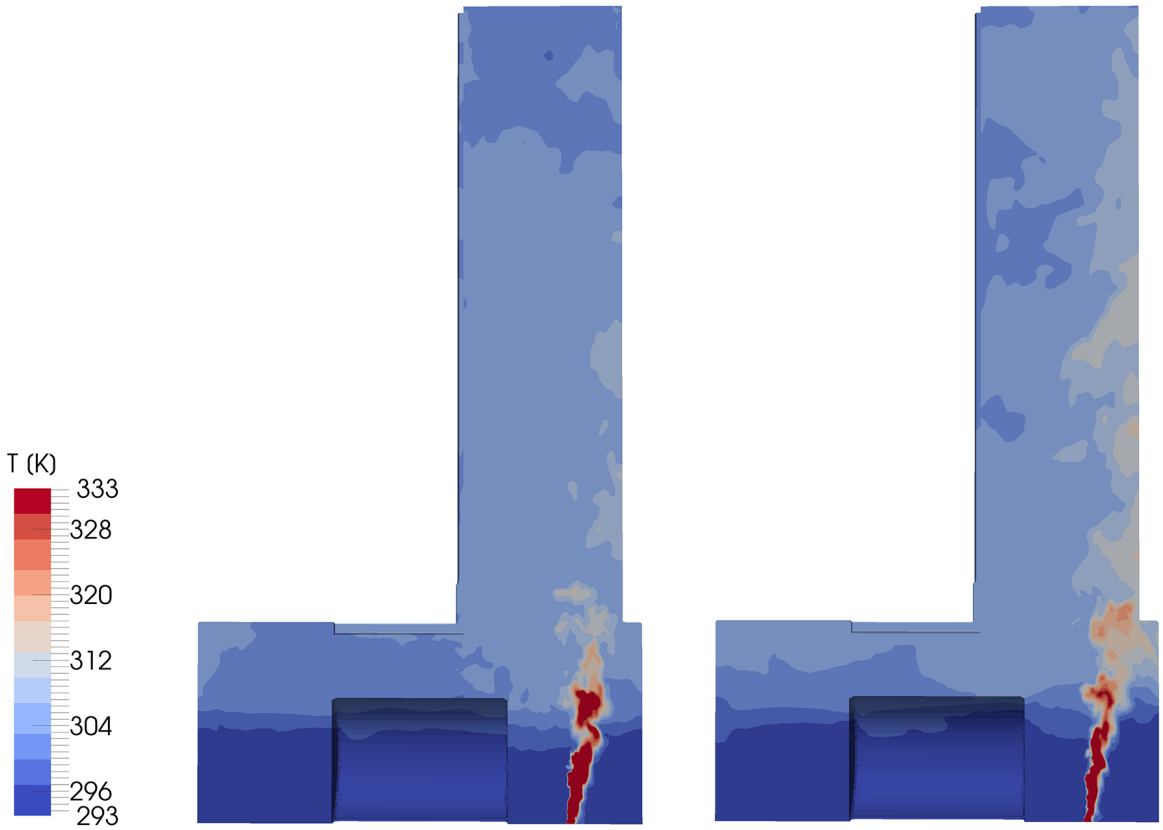

(a) 1 MW, 20 min. (b) 1.5 MW, 14 min.

Figure 5.8: Instantaneous temperature contours for the cavern volume open towards the surface level and the neighboring cavern (1 MW, 20 min and 1.5 MW, 14 min).

Due to the cross-sections open towards the surface level and towards the CMS service cavern, the access shaft of the CMS experimental cavern is found to be acting like a chimney, cf. fig. 5.9. Velocity magnitudes reach $6\,\mathrm{m{\cdot}s^{-1}}$ and more inside the access shaft of the experimental cavern in case of the 1.5 MW case, cf. fig. 5.9(b). Both, instantaneous temperature and velocity contours show slightly inclined plumes towards the cavern wall next to the fire position. This is a side effect of the additional inflow through the cavern, which is also visible along the detector in figures 5.9(a) and 5.9(b), showing a velocity magnitude of about $2\,\mathrm{m{\cdot}s^{-1}}$ on the far side of the fire position.

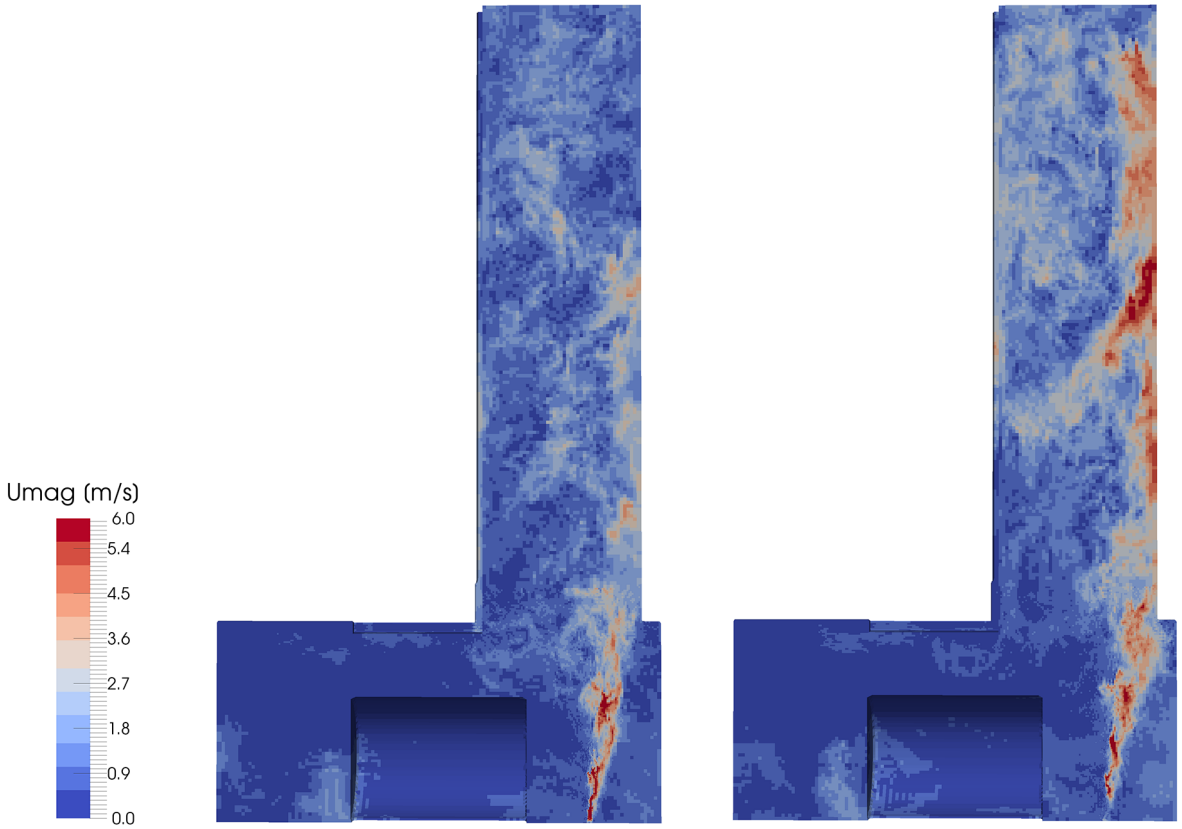

(a) 1 MW, 20 min. (b) 1.5 MW, 14 min.

Figure 5.9: Instantaneous velocity magnitude contours for the cavern volume open towards the surface level and the neighboring cavern.

Figure 5.10 shows velocity vector fields inside the CMS experimental cavern for two different fire positions and ventilation configurations, based on velocity magnitude. Vector fields have been partially cut and the overall velocity magnitude scale has been limited from 0 to 6 $\mathrm{m{\cdot}s^{-1}}$ to improve readability. In case of a fire below the cavern ceiling, the flow is deflected at the cavern ceiling in all directions, mainly into positive and negative z-direction, cf. fig. 5.10(a). Further, a flow deviation from below the cavern ceiling into the access shaft is visible (near side, w.r.t. to the fire position), while at the far side a flow into the experimental cavern from the access shaft is taking place. In case of a fire directly below the access shaft, a similar flow pattern in the lower access shaft is found, cf. figure 5.10(b). Due to the slightly different geometry additional fresh air is supplied on ground level, passing behind the detector (on the positive x-direction cavern part) and finally being entrained into the thermal plume.

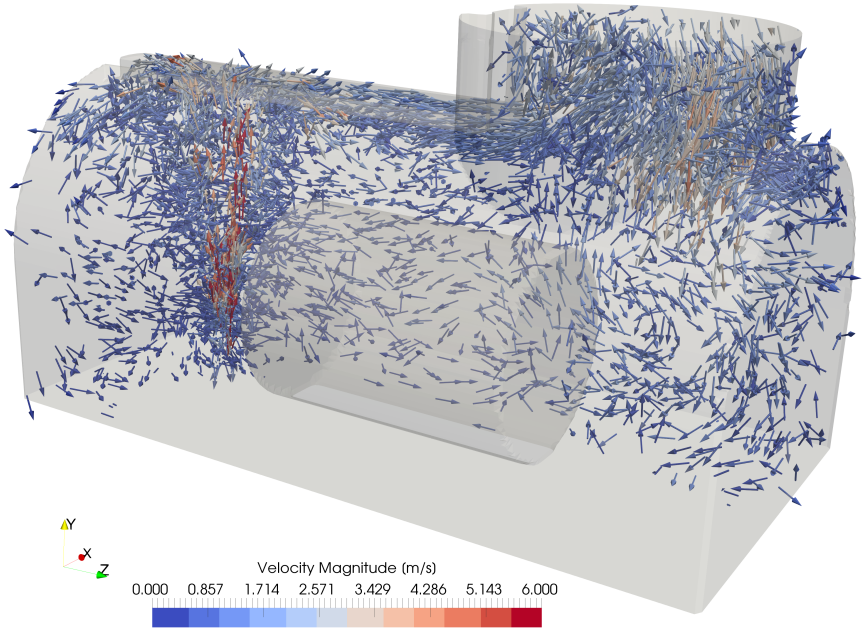

(a) Fire below cavern ceiling.

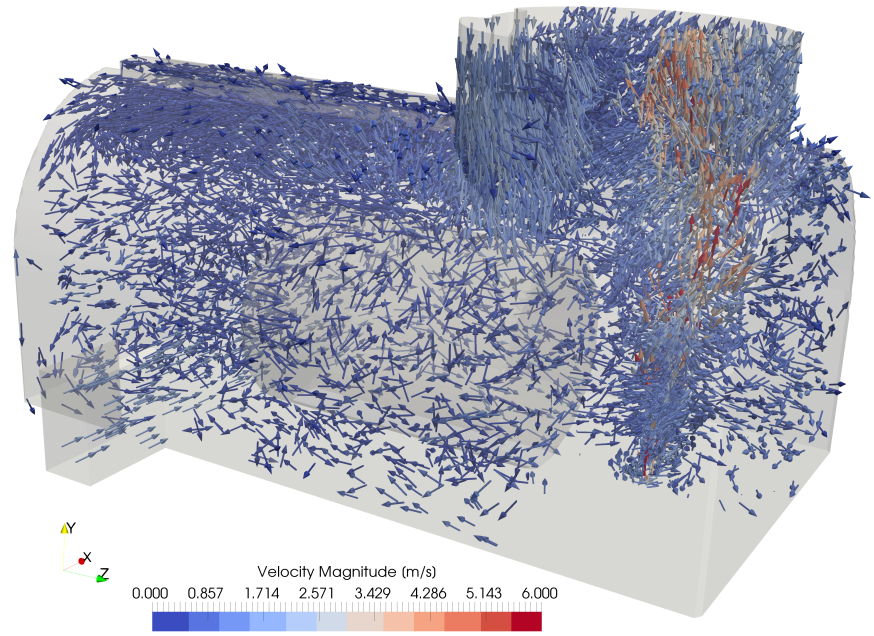

(b) Fire below access shaft.

Figure 5.10: Velocity fields inside the experimental cavern volume for two different fire positions (1.5 MW, 13.5 min, geometry and velocity fields partially cut to improve readability.).

As a plug flow seems to be the worst case in terms of aerosol release to the surface level, also a smaller fire representing case with a preset HRR of 500 kW is calculated in order to investigate if this kind of flow is linked to a certain HRR threshold. The results are shown in figure 5.11. Comparing figure 5.11(a) with 5.8 one notes only a small difference in terms of temperature evolution inside the cavern. The plug flow inside the cavern volume is independent of the HRR of a certain fire scenario. However, the velocity magnitudes vary accordingly.

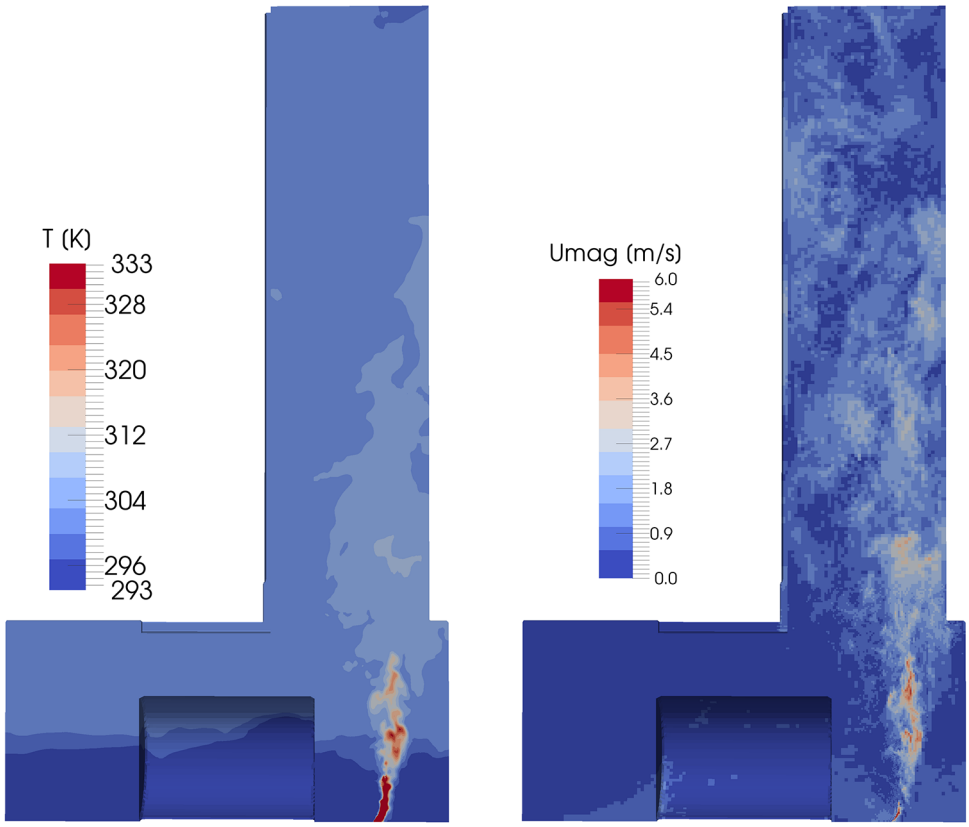

(a) Temperature. (b) Velocity magnitude.

Figure 5.11: Instantaneous temperature and velocity magnitude contours for the cavern volume open to the surface level and the neighboring cavern (0.5 MW, 40 min).

5.2 Fire-induced aerosol results for the CMS experimental cavern

As discussed in section 3.3.3, a modified local interaction rebound sub model for Lagrangian parcels is used to gather data on particle release and deposition. Three different variants have been run: unlimited[1] rebounds for a particle, user-defined maximum of rebounds for a particle before considering it as released or deposited, and the default local interaction sub model, where a particle is released or deposited on first interaction. Section 5.2.1 covers the unlimited rebound data, section 5.2.2 the limited part, while section 5.2.3 is dedicated to the standard sub model used for comparison reasons.

While the original models feature more than 40 different surfaces ("patches"), in the following sections the patch results are grouped as follows:

- Floor; covers the entire floor of the CMS experimental cavern
- Cavern - and + end; cavern walls perpendicular to the beam line
- Cavern ceiling; ceiling part of the cavern, walls parallel to the beam line, access shaft partly up to 24 m
- Detector; detector surface
- Access shaft; access shaft from 24 up to 98 m

Figure 5.12 shows a graphical illustration of the grouped patches. Here, these six placeholders shall demonstrate the methodology. For any further application, the number of surfaces might be increased to obtain detailed results e.g. on deposition on each of the five different particle detector wheels of the CMS experiment.

[1] Technically unlimited rebounds are achieved by setting $n_{\mathrm{reb}} = 10^8$, which is below the current code limit of a scalar value ($\approx 10^9$). A single particle has never shown more than 10^6 rebounds. Thus this approach is justified.

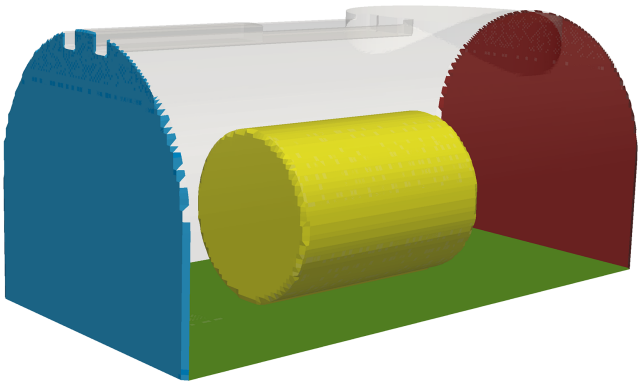

Figure 5.12: Illustration of the different patch groups: Floor (green), cavern - (blue), cavern + (red), detector (yellow), and cavern ceiling (grey, transparent part).

While in sections 5.2.1, 5.2.2 and 5.2.3 these simplified surfaces are used, please note that the results given, i.e. in terms of the unlimited local interaction model compared to the two others are not directly comparable. Unlimited surface interaction and its post-processing takes into account the history for each individual parcel, while limited interaction gives instantaneous data on particle release and deposition, where release and deposition fractions are extracted at a certain time step. As such, e.g. a comparison between total hits per patch and a deposition data table in annex A is not possible.

5.2.1 Local interaction unlimited rebound sub model

Lagrangian particles with 1, 10 and 100 μm are used. Based on the scale of Hinds, 1 and 10 μm particles have been chose to represent smoke [81]. A class of 100 μm particles was added, following a proposal from CERN's radiation protection group [108]. So far it is unknown, which radioactive isotope would attach to what kind of aerosol. Thus, 100 μm particles have been added to represent heavy isotopes, e.g. ^{60}Co, assumed to attach themselves rather to large diameter aerosols than to smaller ones. A uniform particle density of 10^3kg·m^{-3} is used, as proposed by Hinds for aerosol modeling [81].

For each aerodynamic diameter 10,000 particles are injected continuously during the quasi steady-state HRR phase of each case. Using a CMS experimental cavern case open towards the surface level and a preset HRR of 1.5 MW over 800 s (next available time step is memorized at 840 s or 14 minutes), the following results have been obtained.

Figure 5.13 and table A.13 give an overview on the absolute values of how many particles hit how many patches. Starting with the smallest aerodynamic diameter of 1 μm, 5,340 out of 10,000 particles hit no patch at all (53.4%) i.e. they are dispersed in air, 4,197 hit only one patch (41.97%) while 463 hit at least two patches (4.63%). Regarding the 10 μm particles, 46.22% hit no patch at all, 42.64% hit only one patch while 11.14% hit two up to four patches. For the 100 μm particles it can be shown, that only 10.41% hit no patch at all, 71.33% hit one and 18.26% hit two patches or more.

Figure 5.14 shows the percentages of total patch hits after 14 minutes, at a HRR of 1.5 MW in a cavern open to the surface level. Total patch hits include all particle hits, regardless of the individual number of patches particles have hit. The total patch hits differ only slightly from hits generated by particles hitting only one patch, cf. figure 5.15(a) and table table A.14. Only 11% (1 μm), 23% (10 μm) and 16% (100 μm) of all (total) particle hits occur on two or more patches, cf. table A.14. However, particles hitting two or more patches give additional information on how the present model behaves. Therefore, the interaction of particles hitting exactly two or three patches is described in detail below.

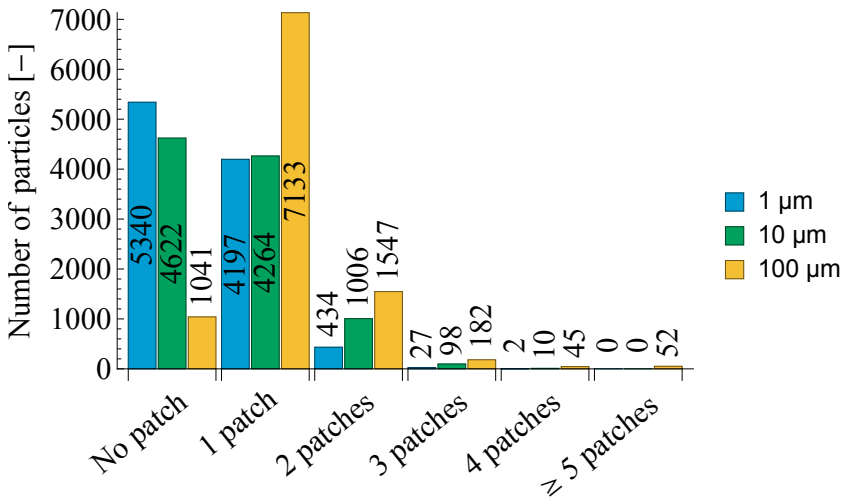

Figure 5.13: Overview on 1, 10 and 100 μm particles having hit no, one or multiple patches (1.5 MW, 14 min, cavern open to the surface level, unlimited rebounds).

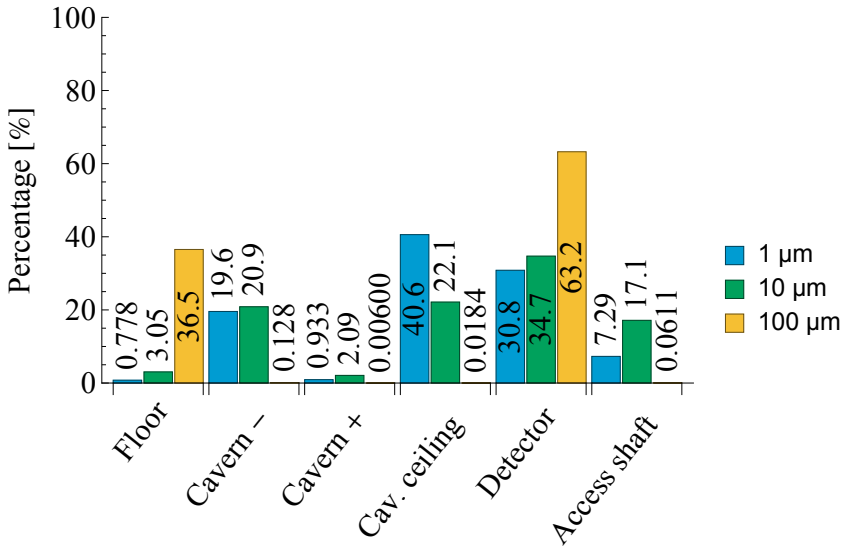

Figure 5.14: Percentages of total patch hits (1.5 MW, 14 min, cavern open to the surface level, unlimited rebounds).

Based on the total number of hits generated by particles hitting one or more patches, percentages have been derived for single patch particles and multiple patch particles, cf. figures 5.15(a) and 5.15(b). Particles with a 1 μm aerodynamic diameter hitting only one patch are merely concentrated on the cavern (-) end, the cavern ceiling, the detector surface and the access shaft. Particles of the same class but hitting multiple patches show less hits on the cavern (-) end (21.4% vs 5.02%) and more hits on the detector (29% vs 45.5%). As for 10 μm particles hitting only one patch, the hits are mainly distributed between the cavern (-) side, the cavern ceiling, the detector and the access shaft. For the latter, 10 μm particles outperform even the 1 μm particles, an effect further described below. For 10 μm particles hitting two or more patches, the impact is increased for the cavern ceiling (45.8% vs 15.1%) while the percentages for cavern ceiling and detector are decreasing. Finally, the 100 μm hitting only one patch are mainly distributed between the detector surface and the cavern floor. For particles of the same class this behavior is reversed in case of hitting two or more patches, presumably caused by 100 μm particles hitting first an elevated surface such as the cavern (-) end, its ceiling or the detector surface, settling down towards the cavern floor.

Figure 5.16 shows the percentages on the different patches hit by particles that impact

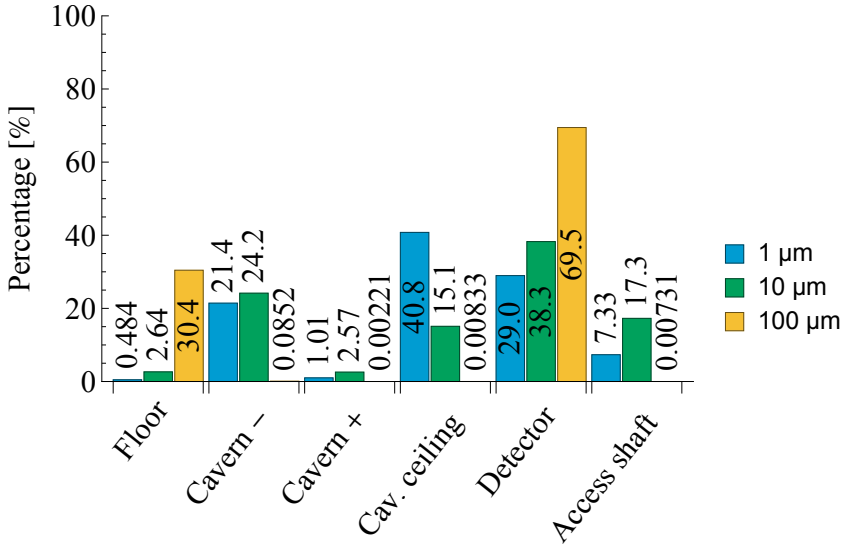

(a) Single patch hits.

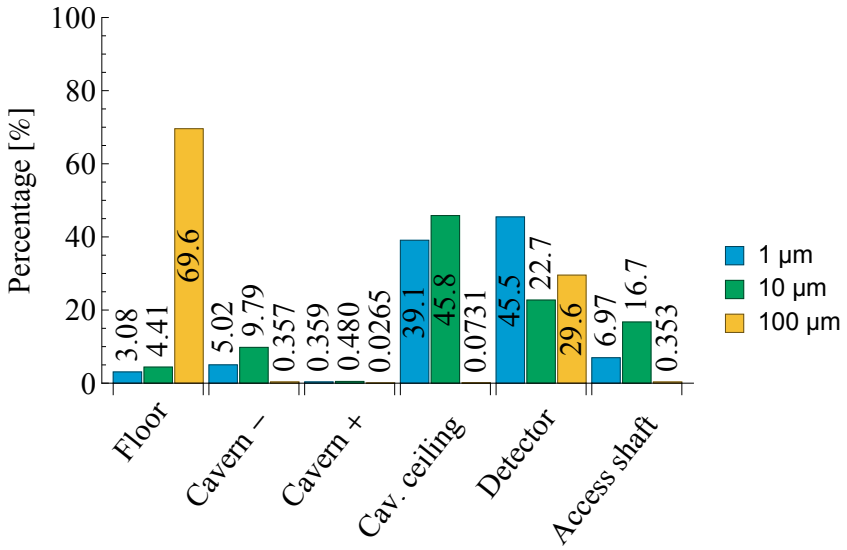

(b) Multiple patch hits.

Figure 5.15: Percentages of single and multiple patch hits (1.5 MW, 14 min, cavern open to the surface level, unlimited rebounds).

exactly on two surfaces. The lightweight 1 and 10 μm particles hit as first patch merely the cavern ceiling part, the cavern (-) wall next to the fire position and the access shaft, following the thermal plume flow. Their second impact is mainly concentrated in the access shaft, i.e. by particles just getting in, or by particles that have been already carried along towards the surface and are partly settling down. As for the larger 100 μm particles, the first patch hit is distributed among the cavern (-) side, the cavern ceiling and the detector. Only a very small part reaches the access shaft. A second contact of the 100 μm particles is mainly made with the floor and the detector.

For all three different aerodynamic diameters, the behavior is meeting the physical expectations. Lightweight particles reach higher surfaces with an increased number of hits compared to the 100 μm particles, while the latter reach merely the cavern part of the geometry and settle down towards floor level.

Percentages for particles hitting exactly three patches are shown in fig. 5.17. For the 1 μm parcels, the cavern walls, the cavern ceiling and the access shaft are the main surfaces regarding their first impact. The second is consisting mainly of the access shaft and the cavern ceiling. This can be explained by particles moving from the cavern ceiling into the shaft while the ones being already in the access shaft rise higher inside. Also the third patch interaction of 1 μm particles mainly takes place inside the access shaft, while the percentages i.e. for the cavern (+) side and the detector, both next to or below the access shaft have been increased by particles floating back from the access shaft into the cavern. Looking at the 10 μm parcels, starting from fig. 5.17(a), their behavior is similar to the 1 μm case discussed above. However, on their first interaction, less 10 μm particles hit the cavern ceiling and the access shaft. This is a desired effect, as the heavier 10 μm particles should stick around more to the lower part of the geometry as the lighter 1 μm parcels. As for the second and third patch contact made by 10 μm particles, this is not the case. The 10 μm slightly overtake the 1 μm particle hits inside the access shaft, cf. fig. 5.17(b), while the order is reversed during the third contact, cf. figure 5.17(c). As for the 100 μm particles, their impact behavior is again in line with the expectations. Carried along the thermal plume, they initially hit mainly the cavern ceiling, the access shaft and the detector surface. This is followed by intermediate contacts on the cavern (-) side next to the fire position, the access shaft and the cavern ceiling, but mainly on the detector surface. Finally, 100 μm parcels impact merely the cavern floor.

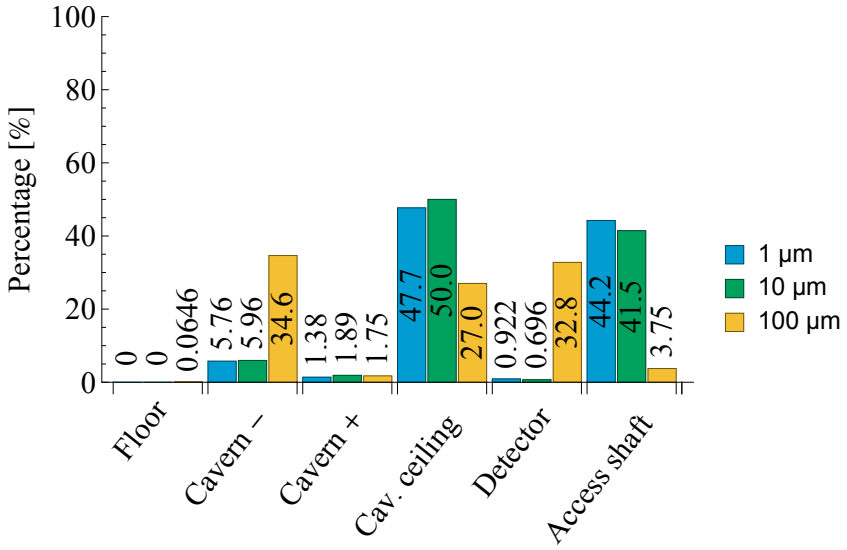

(a) First patch.

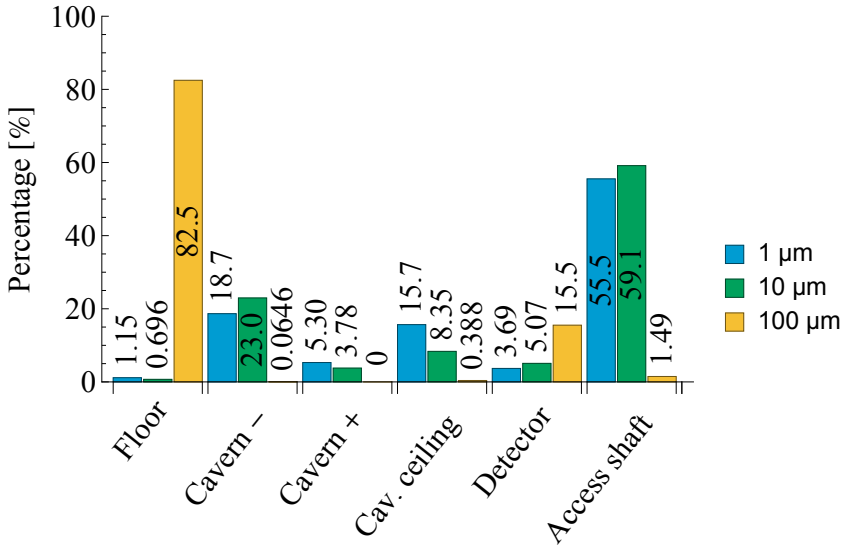

(b) Second patch.

Figure 5.16: Percentages of 1, 10 and 100 μm particles hitting exactly two different patches (1.5 MW, 14 min, cavern open to the surface level, unlimited rebounds).

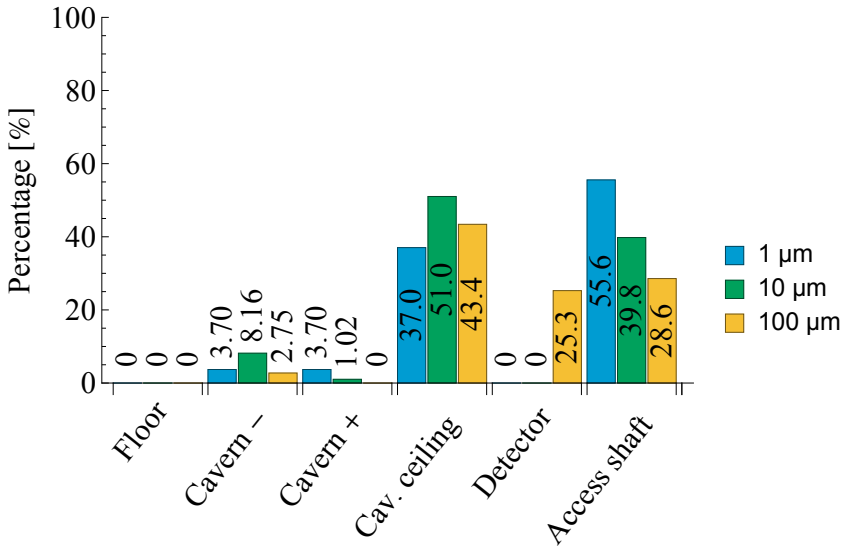

(a) First patch.

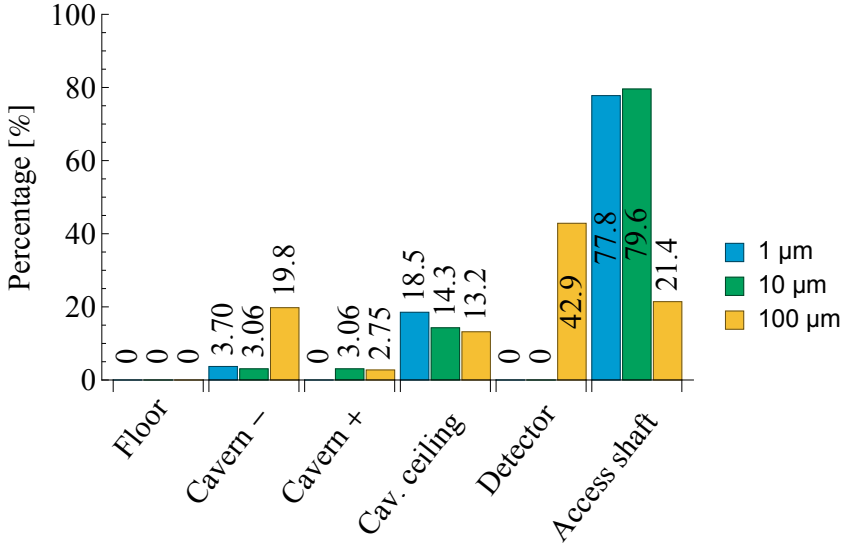

(b) Second patch.

Figure 5.17: Percentages of 1, 10 and 100 μm particles hitting exactly three different patches (1.5 MW, 14 min, cavern open to the surface level, unlimited rebounds).

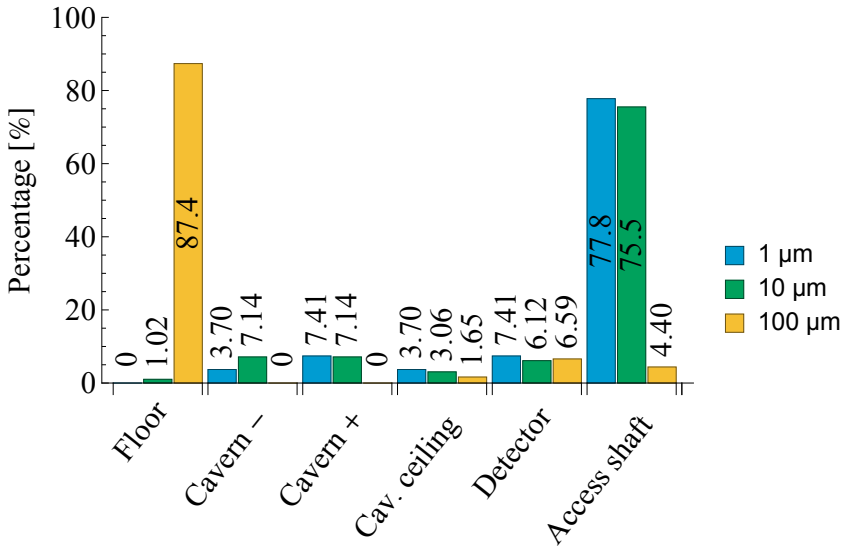

(c) Third patch.

Figure 5.17: Percentages of 1, 10 and 100 μm particles hitting exactly three different patches (1.5 MW, 14 min, cavern open to the surface level, unlimited rebounds).

Each simulation has been continued for additional ten minutes of simulated time (particle settling time), in order to analyse the particle behaviour after the quasi-steady heat release duration. Results have been obtained normally for 1 and 10 μm particles. However, for the 100 μm particles the amount of data to be written to temporary disk space exceeded the technical capabilities[2]. As already about 90% of the 100 μm particles have hit one or more patches at t = 840 s (fig. 5.13) and about 99% registered on floor level and detector surface, the absence of further data can be justified.

Within 10 minutes, the number of patches hit change significantly for both, 1 and 10 μm particles, cf. figures 5.13 and 5.18 (table A.15). An increase of about 20% is noted for the smaller 1 μm particles hitting one patch, while the amount of 1 μm particles hitting two patches increase by 161%. Looking at the 10 μm diameter particles, the same particle hit classes change only by about 6 and 85%, respectively. However, an increase of about 300% is noted for 10 μm particles hitting three different patches.

Principally both particle diameters show an increase of surface interactions with time,

[2]Another attempt could be made involving a parallel file system [109] on a dedicated professional grade high performance cluster system available e.g. at universities.

even if there is no continued thermal plume to impose a flow. This behavior would be expected, considering that particles without further external force would settle in a certain time, depending on their individual aerodynamic diameter.

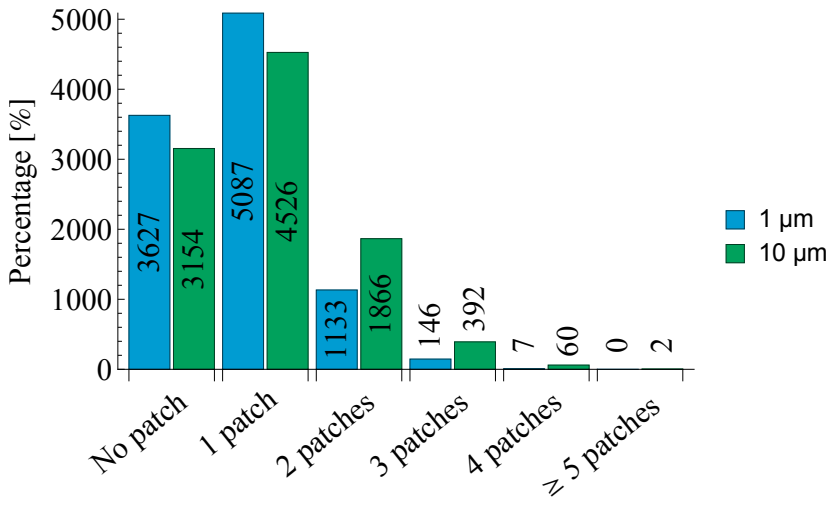

Figure 5.18: Overview on 1 and 10 μm particles having hit no, one or multiple patches (1.5 MW, 24 min, cavern open to the surface level, unlimited rebounds).

Comparing the total number of hits registered for 1 and 10 μm particles after 14 and 24 minutes of simulated time, cf. tables A.14 and A.16, a large increase is determined. The total number of hits increases by approximately 2600% for the 1 μm particles and about 340% for the 10 μm parcels. Accordingly, the single and multiple patch hits change, cf. figure 5.19. While for the the 1 μm particles hitting a single patch after 14 minutes the cavern ceiling was the dominating surface, it is the detector after 24 minutes. As for the 10 μm particles, they keep hitting mainly the detector surface, based on the data extracted after 14 and 24 minutes. Both particle classes hitting more than one patch shifting their impact from the cavern ceiling towards the detector surface.

Following the observations and comparisons for both, total single and multiple patch hits, similar is found for the percentages of total patch hits at $t = 24$ min, cf. figure 5.20 (table A.16). A diminution of hits on cavern ceiling, access shaft and cavern (-) side towards an increase of hits on detector surface and floor is found.

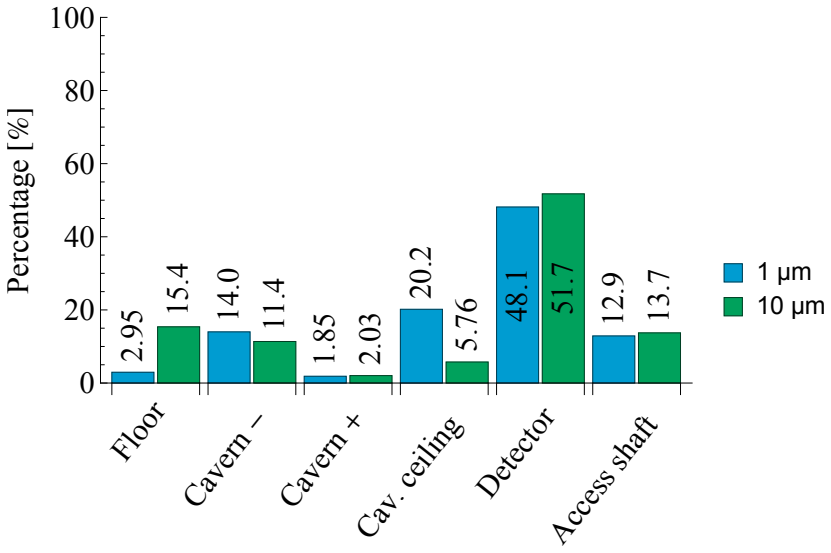

(a) Single patch hits.

Figure 5.19: Percentages of single and multiple patch hits (1.5 MW, 24 min, cavern open to the surface level, unlimited rebounds).

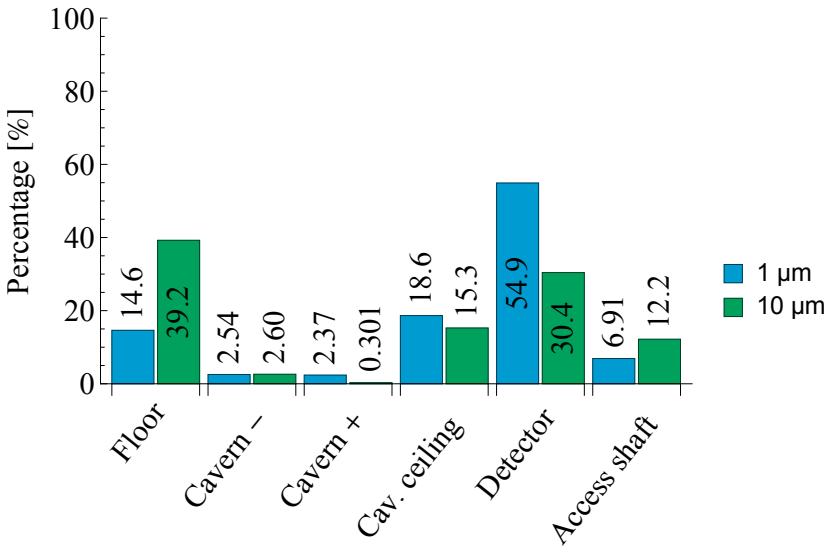

(b) Multiple patch hits.

Figure 5.19: Percentages of single and multiple patch hits (1.5 MW, 24 min, cavern open to the surface level, unlimited rebounds).

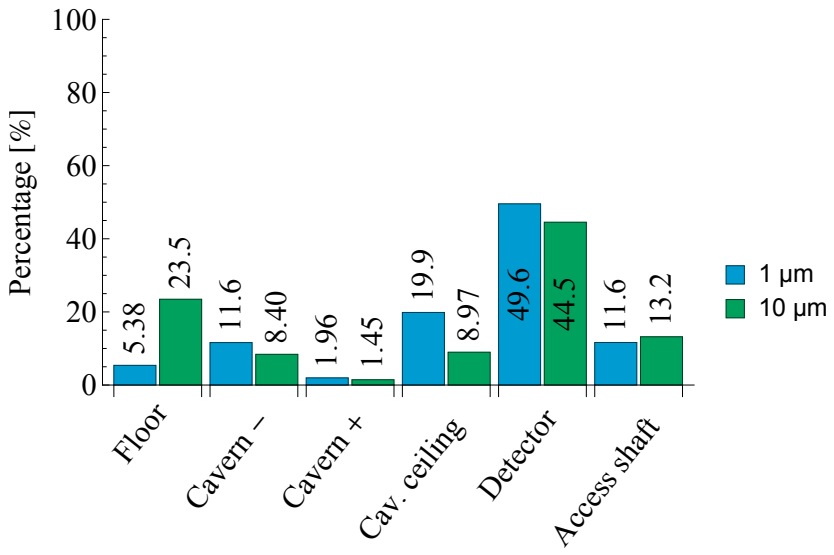

Figure 5.20: Percentages of total patch hits (1.5 MW, 24 min, cavern open to the surface level, unlimited rebounds).

First and second patches have been identified for 1 and 10 μm particles hitting exactly two different surfaces (over 24 minutes), cf. figure 5.21. Both particle diameters show a similar behavior for the first patch, mainly hitting access shaft and cavern ceiling. As for their second patch, the percentages for the access shaft do even increase due to particles settling down along the surface of the access shaft and thus keep rebounding (hitting) the surface. Apart from the increase in the access shaft, both diameters distribute similarly among the different second patch surfaces (with the exception of a peak for the cavern ceiling for 1 μm particles). Figures 5.16 and 5.21 show a similar particle behavior. The same is true for particles hitting exactly three patches, cf. figures 5.22(a), 5.22(b) and 5.22(c). The first patch impact is mainly on the access shaft and the cavern ceiling, followed by a second patch hit, merely in the access shaft. As patch hit by both, 1 and 10 μm particles, again the access shaft shows the highest impact. However, about 10% of each particle class is registered on floor level after 24 minutes (contrary to the percentage in fig. 5.17(c)).

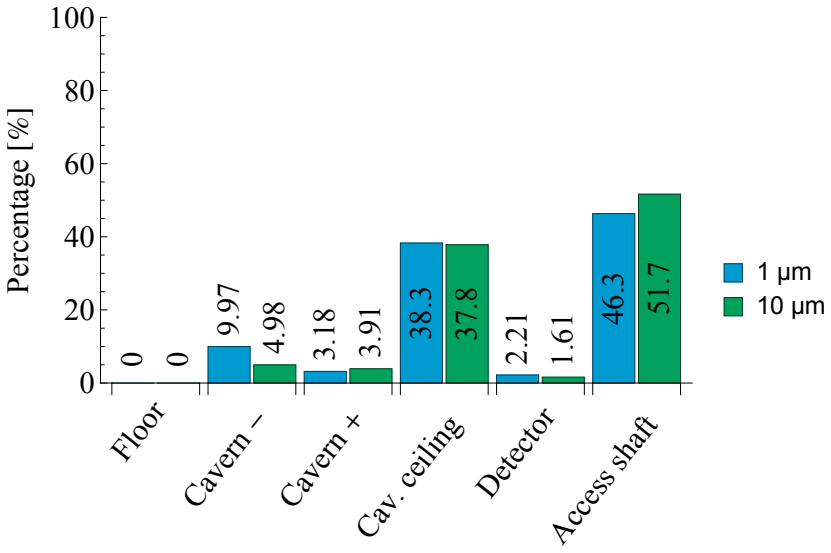

(a) First patch.

Figure 5.21: Percentages of 1 and 10 μm particles hitting exactly two different patches (1.5 MW, 24 min, cavern open to the surface level, unlimited rebounds).

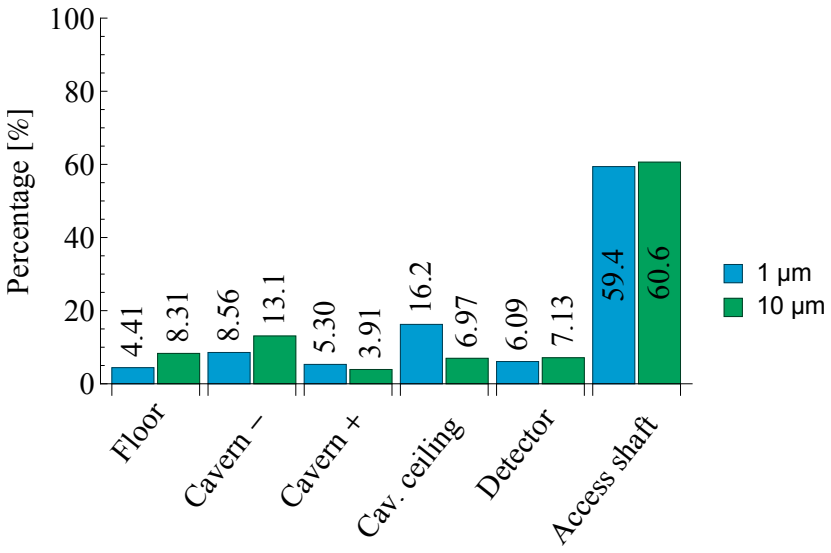

(b) Second patch.

Figure 5.21: Percentages of 1 and 10 μm particles hitting exactly two different patches (1.5 MW, 24 min, cavern open to the surface level, unlimited rebounds).

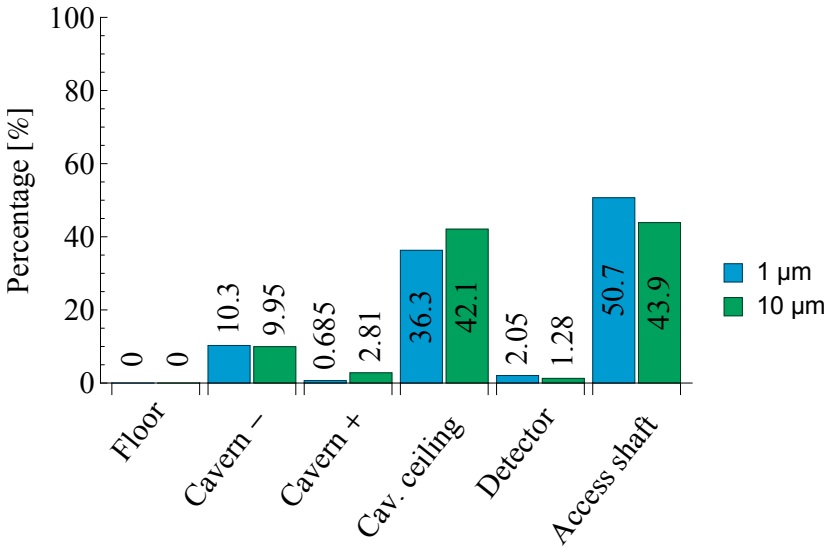

(a) First patch.

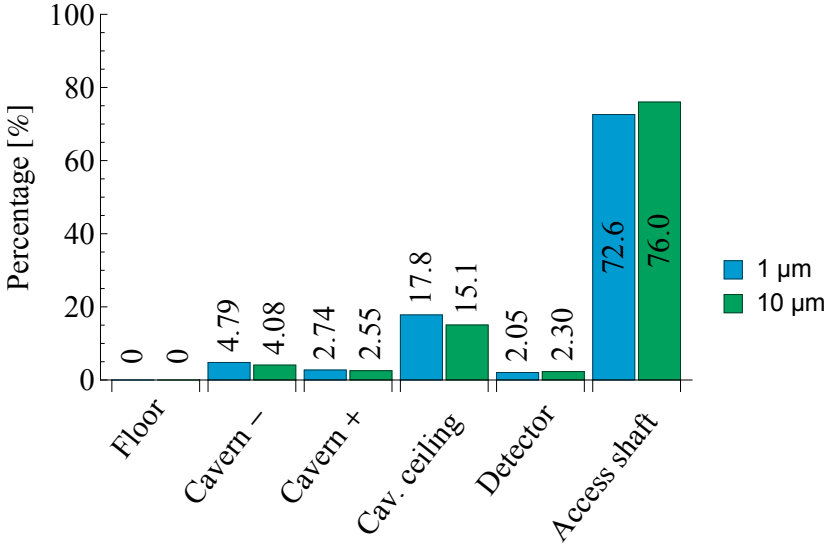

(b) Second patch.

Figure 5.22: Percentages of 1 and 10 μm particles hitting exactly three different patches (1.5 MW, 24 min, cavern open to the surface level, unlimited rebounds).

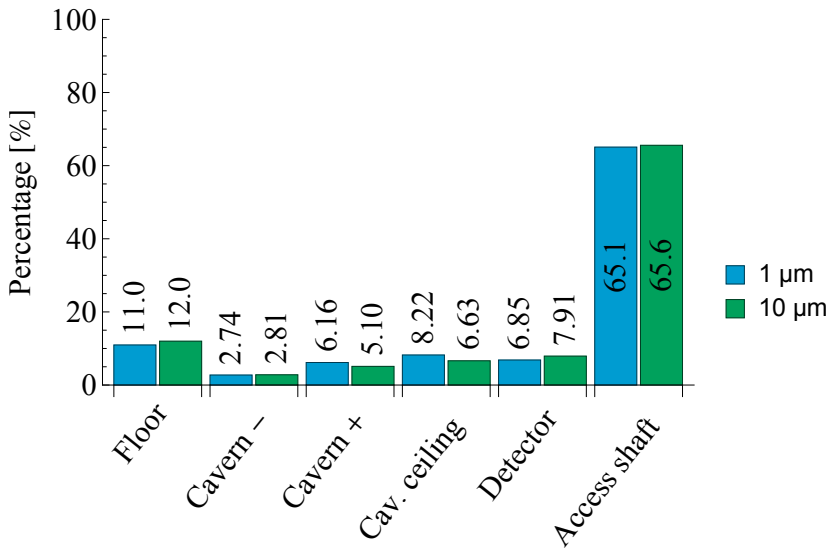

(c) Third patch.

Figure 5.22: Percentages of 1 and 10 μm particles hitting exactly three different patches (1.5 MW, 24 min, cavern open to the surface level, unlimited rebounds).

Considering the discussion above, the model presented in chapter 3 is assumed to be plausible. In principal, particles with different aerodynamic diameters have been found behaving differently, e.g. according to their mass settling on a surface occurs sooner or later. However, based on the results only a minor difference in terms of rebound and deposition behavior has been found for the two aerodynamic diameters of 1 and 10 μm. Especially inside the access shaft noticeably higher values resulted for the 10 μm particles from the simulations, than for the 1 μm ones.

In figure 5.23 all 1, 10 and 100 μm particles have been sorted according to their number of rebounds. Particles with $n_{\mathrm{reb}} = 0$ are summarized in the first three columns, providing the same values for 1 and 10 μm particles as in fig. 5.18. Both, 1 an 10 μm particles show similar trends, although with a shifted peak value. While the peak for the 1 μm particles occurs between 101 and 1,000 rebounds, the 10 μm particles peak between 1,001 and 10,000 rebounds. A different behavior is observed for the 100 μm particles, as about 91.4% show 100,001 or more rebounds. So far no criteria exists to stop particles from interacting. Thus the 100 μm particles who are motionless interacting with a surface such as the experimental cavern floor cause high number of rebounds and large amounts of data.

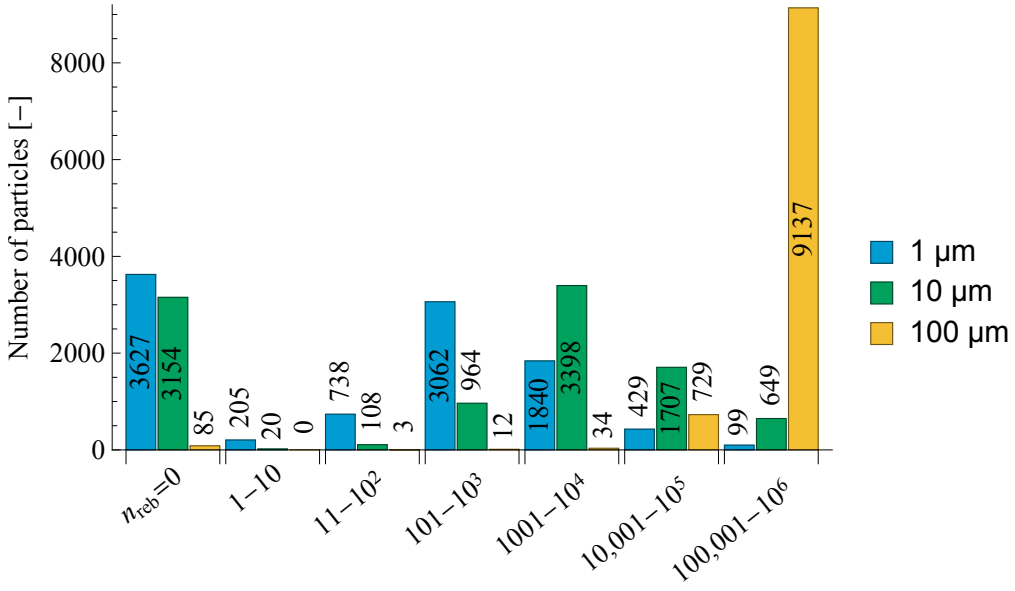

Figure 5.23: Number of particles versus number of rebounds n_{reb} (1.5 MW, 24 min[3], cavern open to the surface level, unlimited rebounds).

Plots like the one shown in figure 5.23 provide means to correct computed release fractions and deposition probabilities by future experimental data. One could assume that e.g. only the $n_{\text{reb}} = 0$ particles are counted as released, i.e. 36.3%, 31.5% and 0.9%. If a certain surface interaction behavior for an aerosol is proven, e.g. a maximum rebound value of 100 for 1 μm particles on a concrete surface, the release fraction for this class of particles could be estimated with 45.7%.

Inside the access shaft, the flow up or down the y-axis (along the access shaft) is the dominating force, based on reviewing the motion history of several individual particles. Figure 5.24 shows an example of instantaneous flow velocity in y-direction after 14 and 24 minutes. For both time steps, one obtains an in-homogeneous turbulent flow field, carrying the Lagrangian particles.

[3]For the 100 μm particles the data has been taken from the last accessible time step $t = 1260$ s.

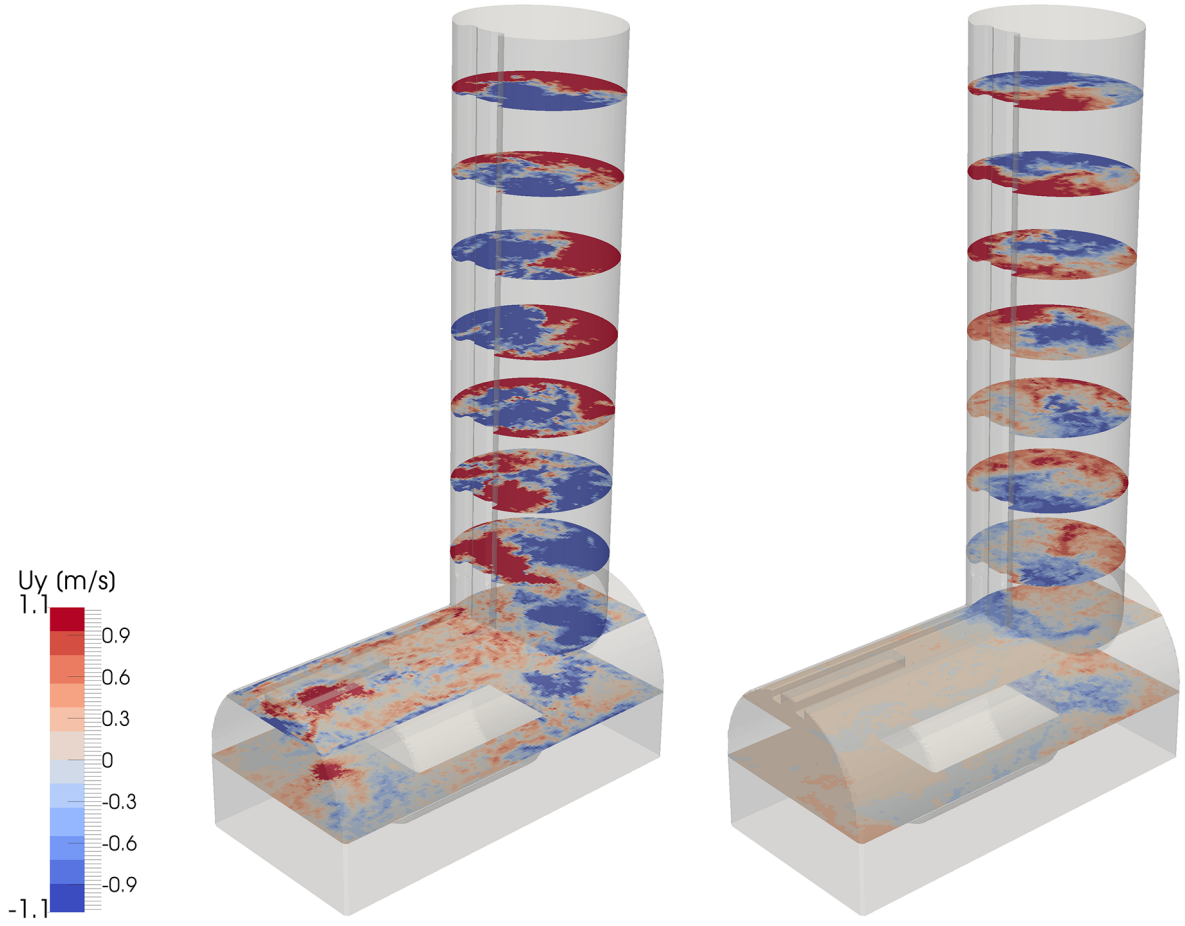

(a) 14 min. (b) 24 min.

Figure 5.24: Instantaneous velocity y-component contours inside the experimental cavern volume (every 10 m in positive y-direction, for two different time steps).

Once a particle reaches its individual highest position inside the access shaft (with respect to the experimental cavern floor) it starts to settle. The phenomenon of settling is shown in figure 5.25, expressed as change in the y-coordinate of a single parcel over time. Due to the nature of the unlimited rebound interaction model, each contact between a particle and a surface is registered. For three similar 10 μm particles next to the internal wall of the access shaft, about 71,000 rebounds over time have been counted. This behavior of slowly settling particles along a wall explains the high patch hit fractions inside the access shaft resulting for 1 and 10 μm particles, analyzing the total number of hits in figures 5.14 and 5.20.

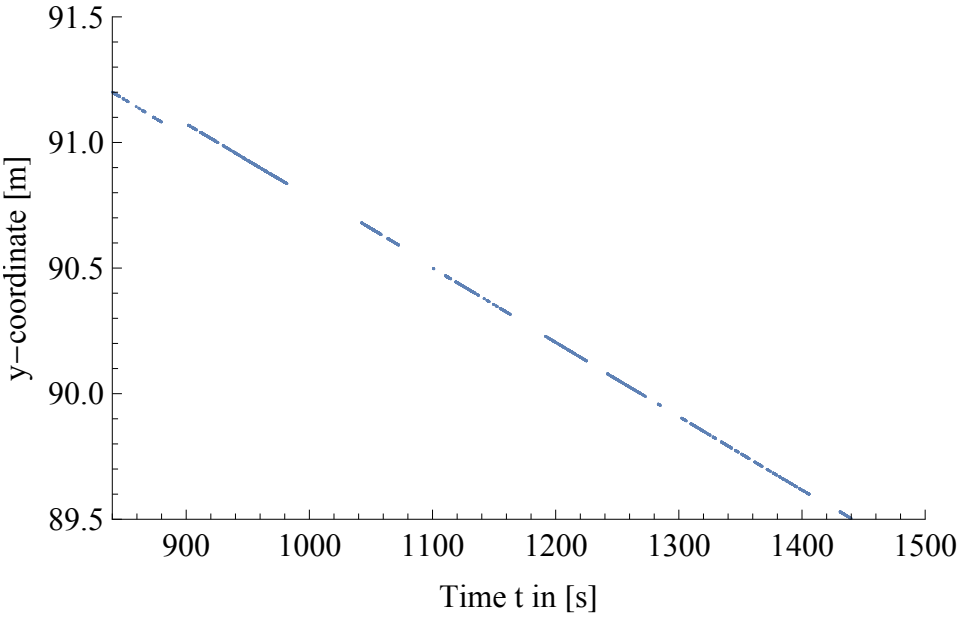

Figure 5.25: Settling of a 10 μm particle inside the access shaft, expressed as change of its y-coordinate over time.

5.2.2 Local interaction limited rebound sub model

As noted in the previous section, the number of rebounds for individual particles can be very high and it might be difficult to understand when a particle eventually deposits to a certain surface. To assess these influence of maximum number of rebounds n_{reb} on the particle interactions with surfaces and release to the ambient, simulations with limited values for $n_{\mathrm{reb}} = 100$ and $n_{\mathrm{reb}} = 10,000$ have been run. The results are discussed below and compared to the unlimited rebound ones in section 5.2.1 above.

Figure 5.26 shows the distribution of 1, 10 and 100 μm particles according to the number of patches hit after 24 minutes, within a maximum of 100 rebounds, cf. also table A.17. Most of the 1 and 10 μm particles hit only one or no patch, while nearly all of the 100 μm particles hit one or two patches. Only approximately 1.3% of the 100 μm particles rest dispersed in air. Comparing figures 5.18 and 5.26 shows, that in total the unlimited rebound particles hit significantly more different patches than their limited relatives, e.g. for both, 1 and 10 μm the percentage of particles hitting exact two patches is 11.3 and 18.7%, compared to 3.8 and 1.1%.

Table A.18 gives an overview on the total patch hits on single and multiple patches.

Compared to the simulations with an unlimited number of rebounds, the total values per patch are much lower (as one would expect from limiting n_{reb}). Figure 5.27 shows the distribution of the single and multiple patch hits for particles with up to 100 rebounds.

While the 1 and 10 μm particles hitting only one patch are merely registered at the cavern (-) side, its ceiling and the access shaft, the percentages for the same particle diameter classes shift towards the access shaft for particles hitting more than one patch. The larger and heavier 100 μm particles hitting only one patch are merely split between the floor and the detector i.e. the horizontal surfaces, while percentages for 100 μm particles hitting two or more patches show a detour of about a third to the cavern ceiling and about 12% towards the access shaft.

Summing up the total number of hits of particles limited to 100 rebounds results in the percentages shown in figure 5.28. About 50% of 1 and 10 μm particle hits take place in the access shaft, approximately 20% each on the cavern ceiling and its belonging wall on the negative z-coordinate (cavern (-)). For the 100 μm particles the percentages are divided between floor and detector surface. Comparing these results to the unlimited ones (fig. 5.20), a clear difference has to be noted. While using unlimited rebounds most hits for 1 and 10 μm particles are recorded on the detector, it is the access shaft for the limited ones. Further much less hits are registered on the cavern ceiling and the floor for the 10 μm particles set to limited rebounds.

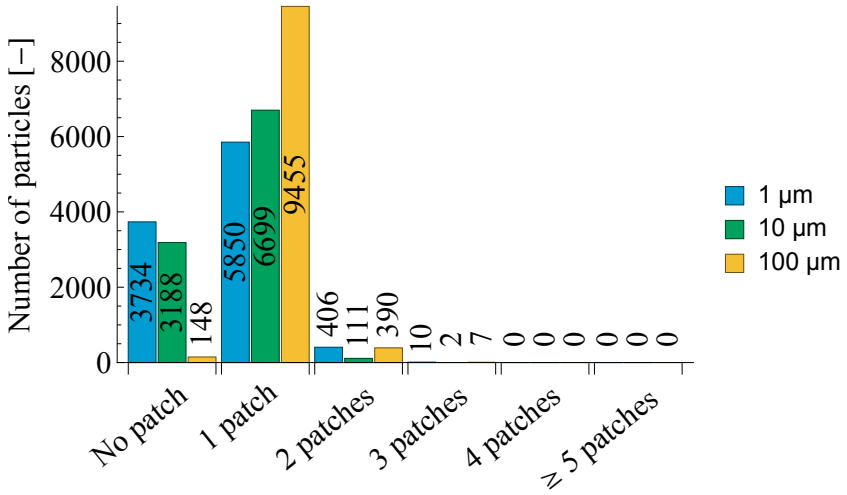

Figure 5.26: Overview on 1, 10 and 100 μm particles having hit no, one or multiple patches after (1.5 MW, 24 min, cavern open to the surface level, n_{reb} = 100).

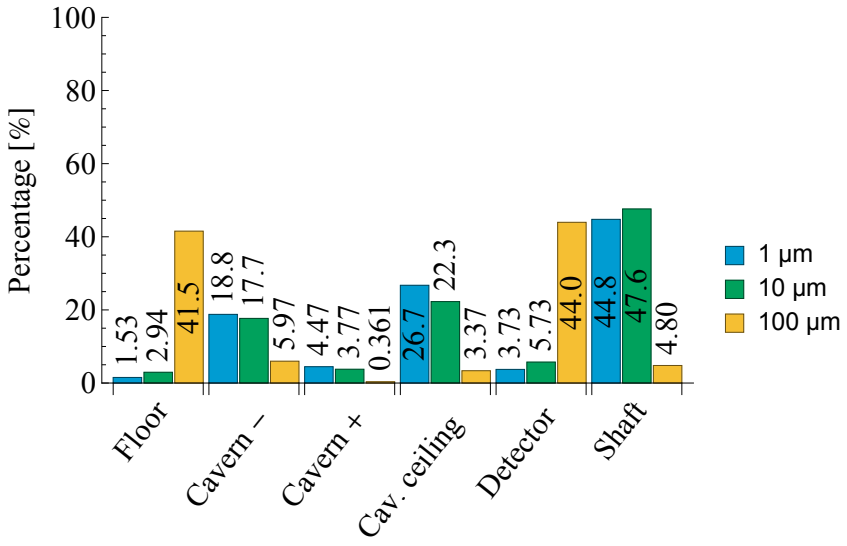

(a) Single patch hits.

Figure 5.27: Percentages of single and multiple patch hits (1.5 MW, 24 min, cavern open to the surface level, $n_{\mathrm{reb}} = 100$).

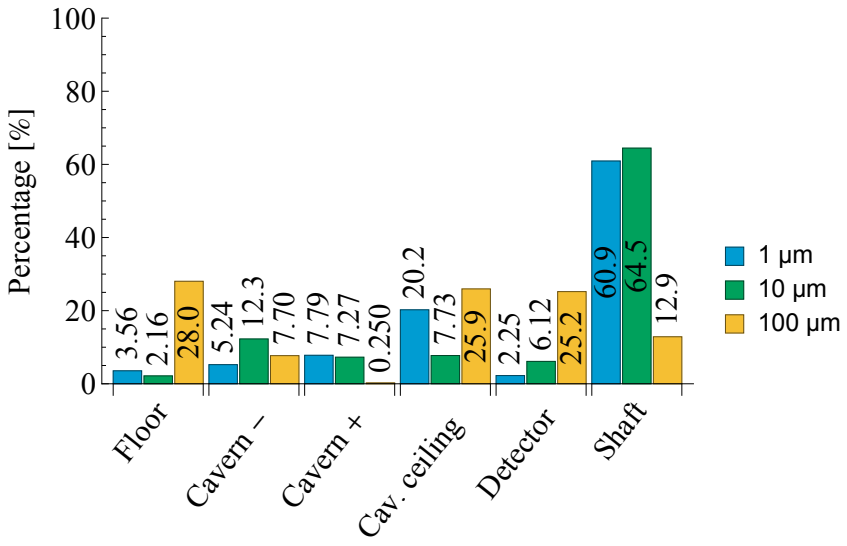

(c) Multiple patch hits.

Figure 5.27: Percentages of single and multiple patch hits (1.5 MW, 24 min, cavern open to the surface level, $n_{\mathrm{reb}} = 100$).

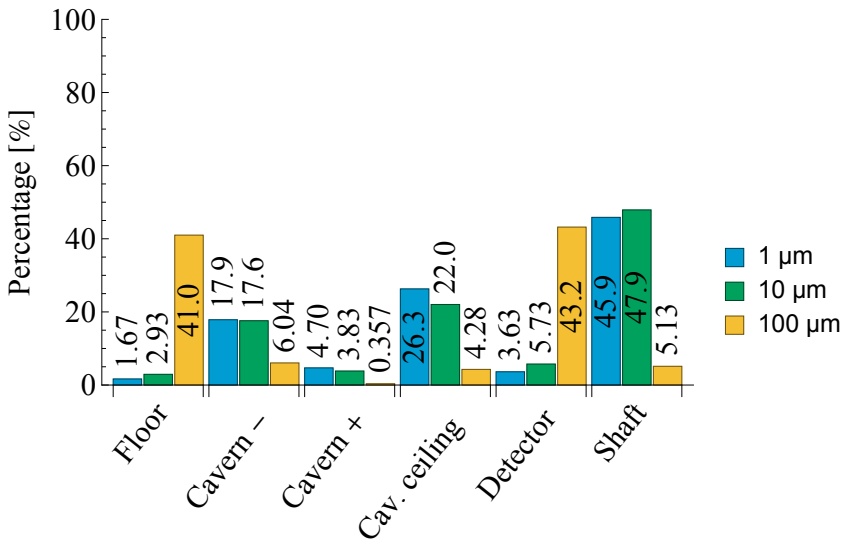

Figure 5.28: Percentages of total patch hits (1.5 MW, 24 min, cavern open to the surface level, $n_{\mathrm{reb}} = 100$).

Figure 5.29 shows the first and second patch hit by particles with exact two patches and limited to 100 rebounds. About three quarter of the 100 μm particles hit the cavern ceiling first, being deflected to their second patches, mainly the floor and the detector surface. A similar trend is observed for the smaller aerodynamic diameters. However, they cause a significant increase in the access shaft.

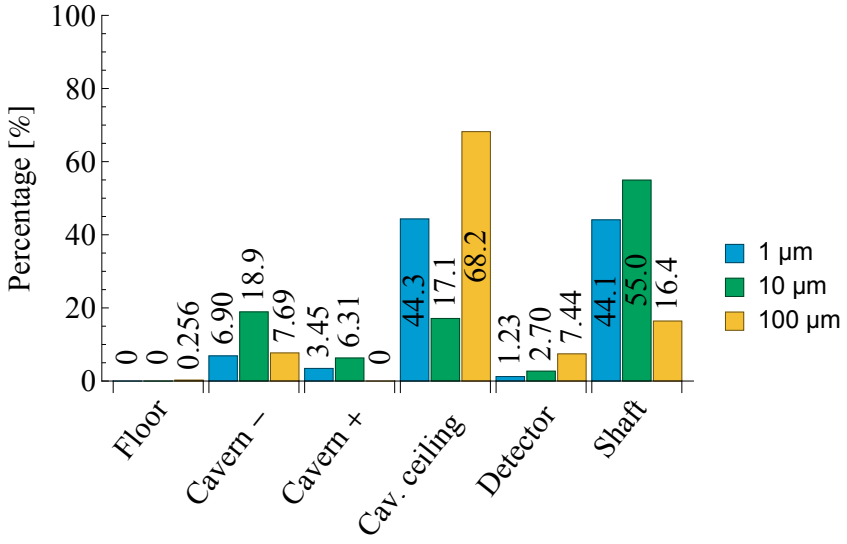

(a) First patch.

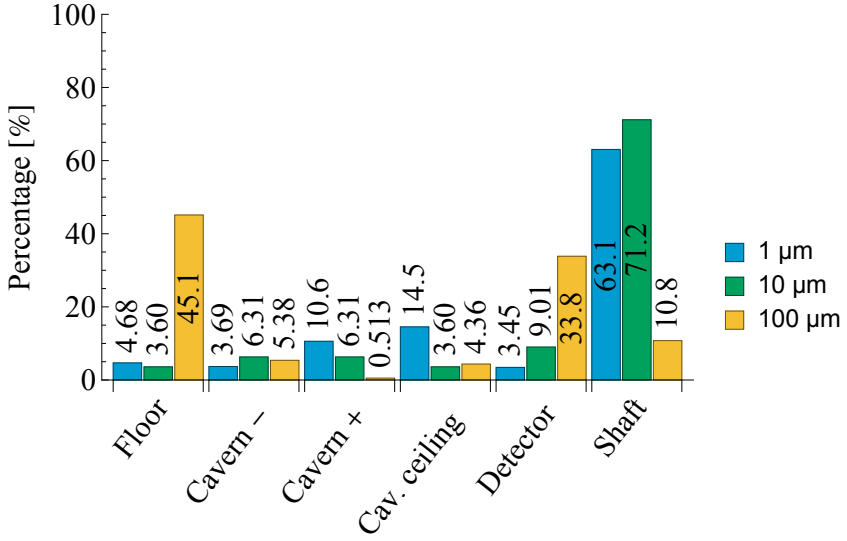

(b) Second patch.

Figure 5.29: Percentages of 1, 10 and 100 μm particles hitting exactly two different patches (1.5 MW, 24 min, cavern open to the surface level, $n_{\text{reb}} = 100$).

Following a limit of 100 rebounds, the next higher value of 10,000 particle rebounds is chosen. Figure 5.30 shows the belonging distribution of particles hitting no, one or multiple patches (table A.19). Its trend is more similar to the results obtained by the

unlimited rebound model after 14 minutes (figure 5.13) and 24 minutes (figure 5.18). However, due to the limitation in rebounds, also data for the 100 μm particles could be extracted and properly stored to disk. In any case, the results are quite similar to the ones shown in figure 5.13, about 80% of the 100 μm particles are hitting only one patch, followed by two patches with approximately 18%.

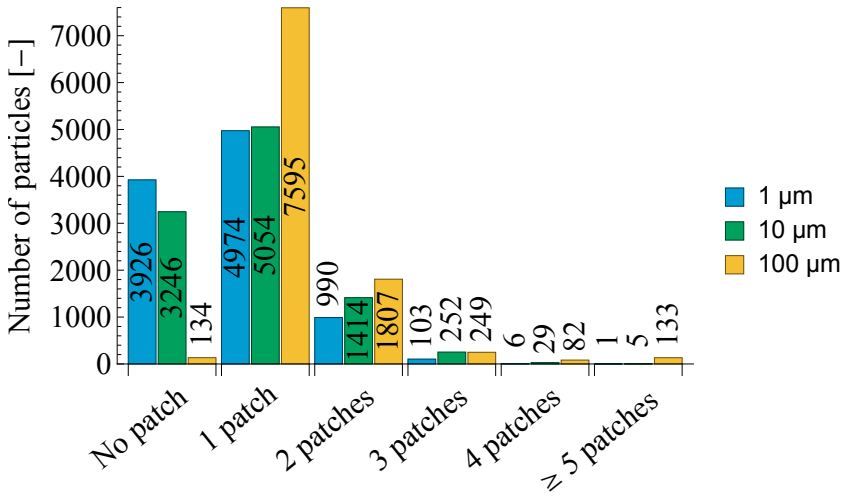

Figure 5.30: Overview on 1, 10 and 100 μm particles having hit no, one or multiple patches (1.5 MW, 24 min, cavern open to the surface level, $n_{\text{reb}} = 10,000$).

Single and multiple patch hits of particles undergoing up to 10,000 interactions are shown in figure 5.31 (table A.20). While the 1 and 10 μm particles hitting only one patch are mostly split in three large chunks on the cavern (-) side, its ceiling and the access shaft, is this not the case for particles hitting multiple patches. The latter show a peak of about 57% for 10 μm particles hitting the access shaft. A deflection is observed for the lighter 1 μm diameter particles towards the floor and the detector surface. No surprise is found for the 100 μm particle class, hitting mainly the floor and detector surface.

The above described behavior is different from the observations for the unlimited rebound particles, cf. figure 5.19.

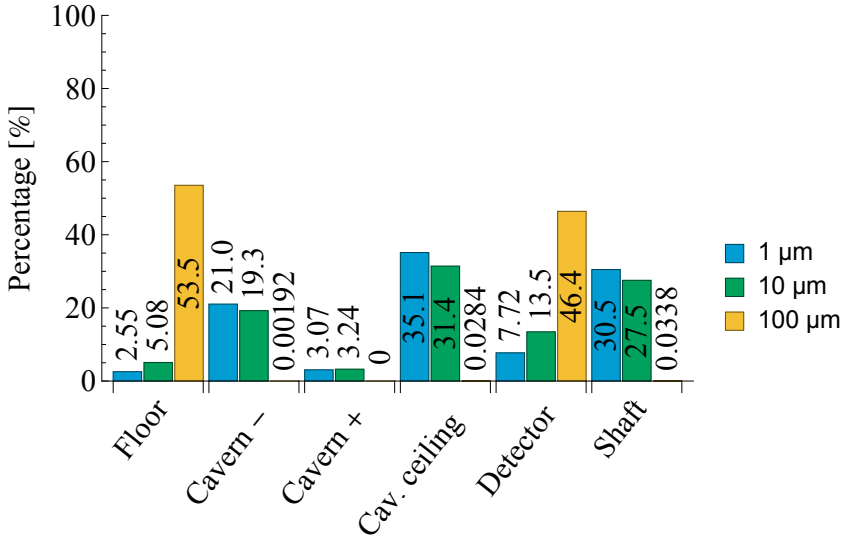

(a) Single patch hits.

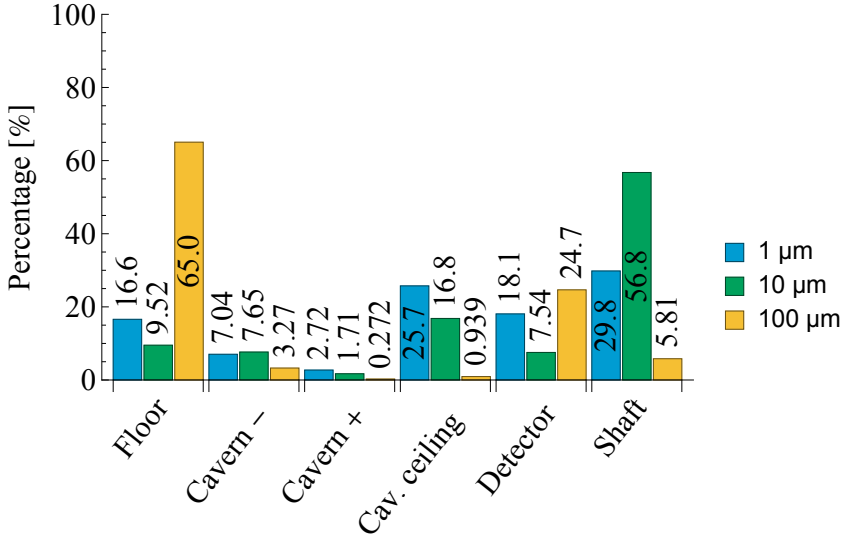

(b) Multiple patch hits.

Figure 5.31: Percentages of single and multiple patch hits (1.5 MW, 24 min, cavern open to the surface level, $n_{\text{reb}} = 10,000$).

Comparing the total hits of particles with unlimited and limited rebounds (10,000), cf. figures 5.20 and 5.32 (and table A.20), several differences are observed. While with unlimited rebounds 1 and 10 μm particles generate most hits (both in the range of 40%)

on the detector surface, the most hits of 1 μm particles limited to 10,000 rebounds are found at the cavern ceiling (inside the access shaft for 10 μm particles). Further peaks occur at cavern ceiling and cavern (-) side, with only about 10% each on the detector surface. A similar behavior has been observed by the limitation of n_{reb} to 100, cf. fig. 5.28. Thus, a limitation in number of rebounds precede to a change in particle hits and by this to a change in residence probability of a particle class on a certain surface.

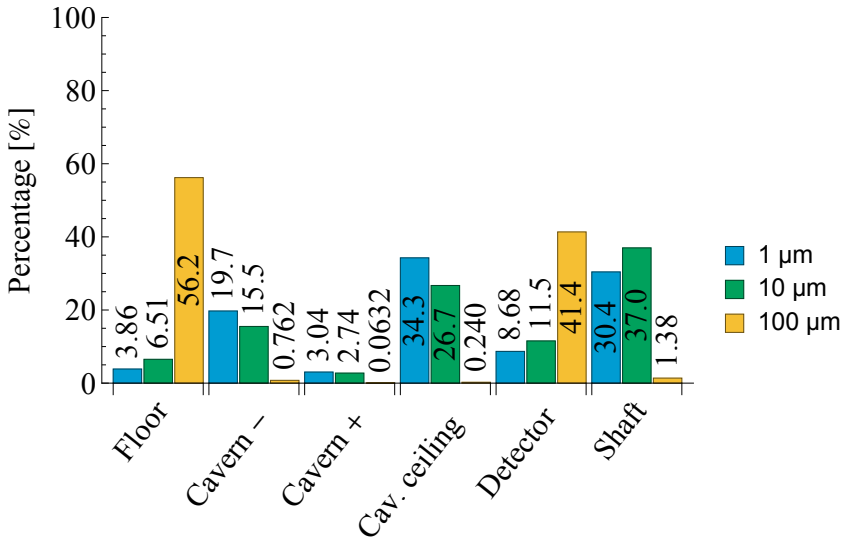

Figure 5.32: Percentages of total patch hits (1.5 MW, 24 min, cavern open to the surface level, $n_{\mathrm{reb}} = 10,000$).

In terms of patch interaction behavior some similarities are observed between the unlimited rebound model and the 10,000 rebounds limit one. Figure 5.33 shows the first and second patch percentages of 1, 10 and 100 μm particles limited to 10,000 rebounds. Both, 1 and 10 μm particles show peaks for their individual first patch inside the access shaft, followed by the cavern ceiling. A tripartition is observed for the 100 μm particles, hitting mainly cavern (-) side, ceiling and the detector. For the latter this changes drastically towards the floor surface with respect to the individual second patch, while for the 1 and 10 μm particles merely the access shaft is registered. In case of the 1 and 10 μm particles, the results of the 10,000 limited rebound calculation is quite similar to the results of the unlimited ones concerning particles hitting exactly two patches, cf. fig. 5.21.

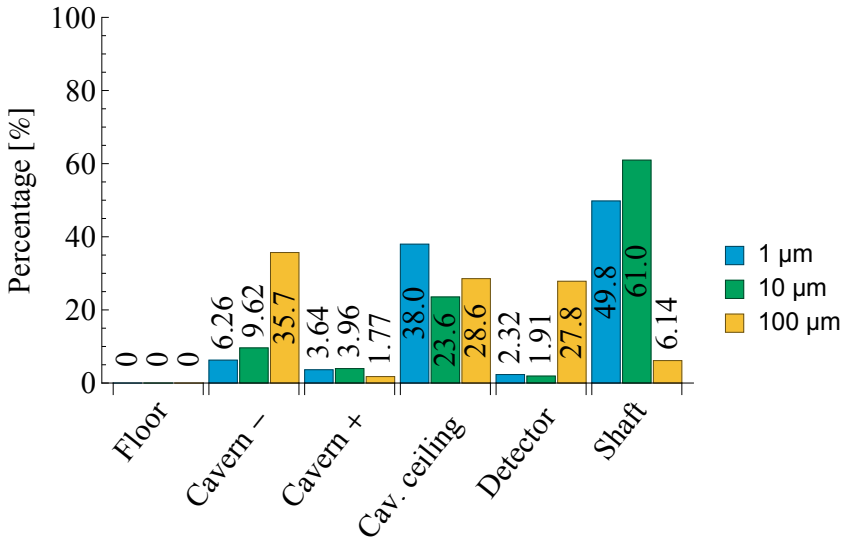

(a) First patch.

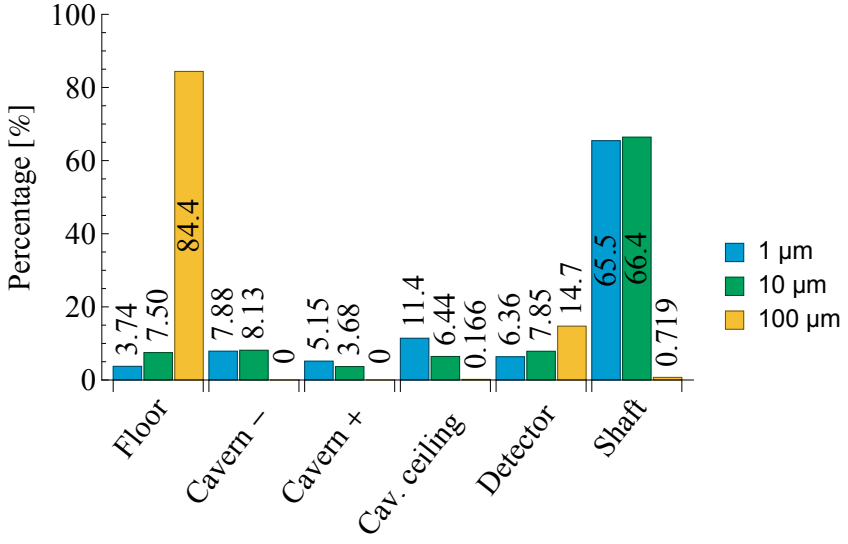

(b) Second patch.

Figure 5.33: Patch percentages of 1, 10 and 100 μm particles hitting exactly two different patches (1.5 MW, 24 min, cavern open to the surface level, $n_{\text{reb}} = 10,000$).

Analyzing the patch sequence of particles limited to 10,000 rebounds and hitting exactly three patches again similarities were found compared to the unlimited particle behavior. Figure 5.34 shows the first, second and third patch distribution for particles

hitting up to 10,000 times. While upon first interaction 1 and 10 μm particles are mainly focused on access shaft and cavern ceiling, the shaft's percentage is increasing upon second contact. Finally, a slight decrease is noticed, especially towards the floor. This is quite similar to figure 5.22 Being larger and heavier, the 100 μm particles show a different order, starting with the cavern ceiling, detector and also the access shaft, the intermediate patch is mainly the detector and the shaft followed by the floor with a huge peak of about 88%.

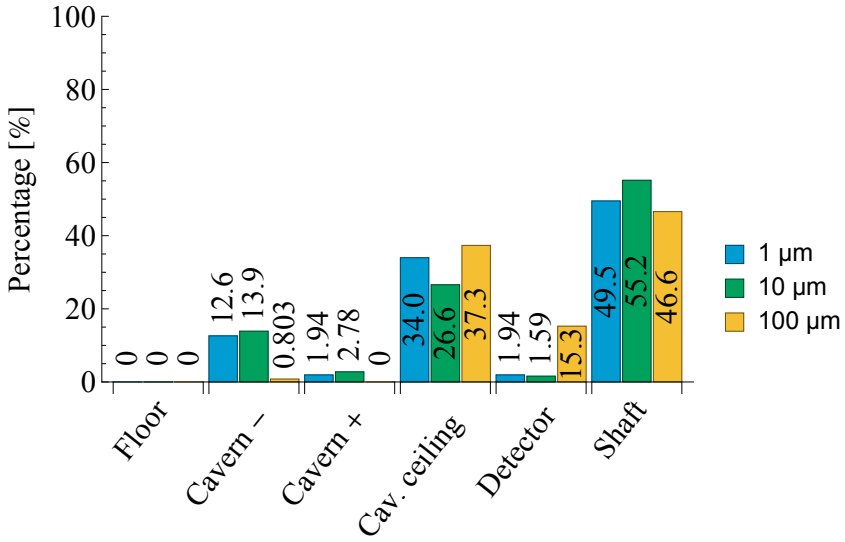

(a) First patch.

Figure 5.34: Percentages of 1, 10 and 100 μm particles hitting exactly three different patches (1.5 MW, 24 min, cavern open to the surface level, $n_{\text{reb}} = 10,000$).

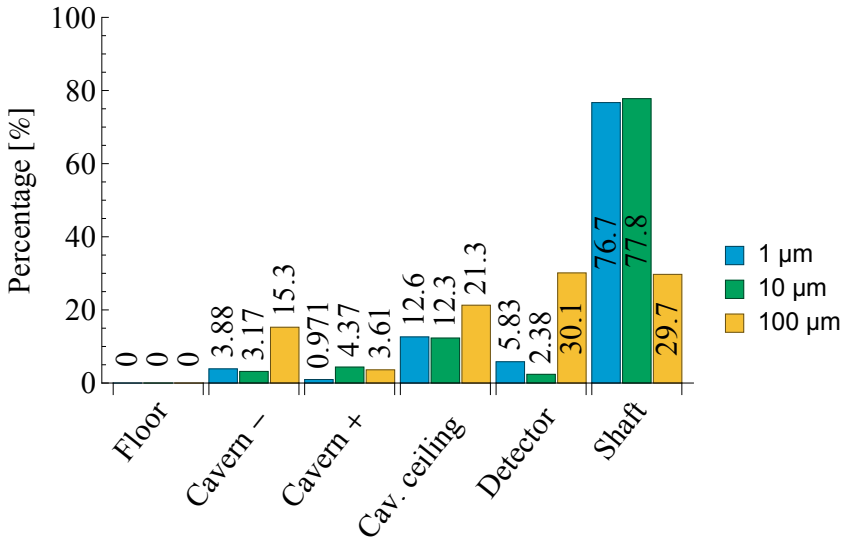

(b) Second patch.

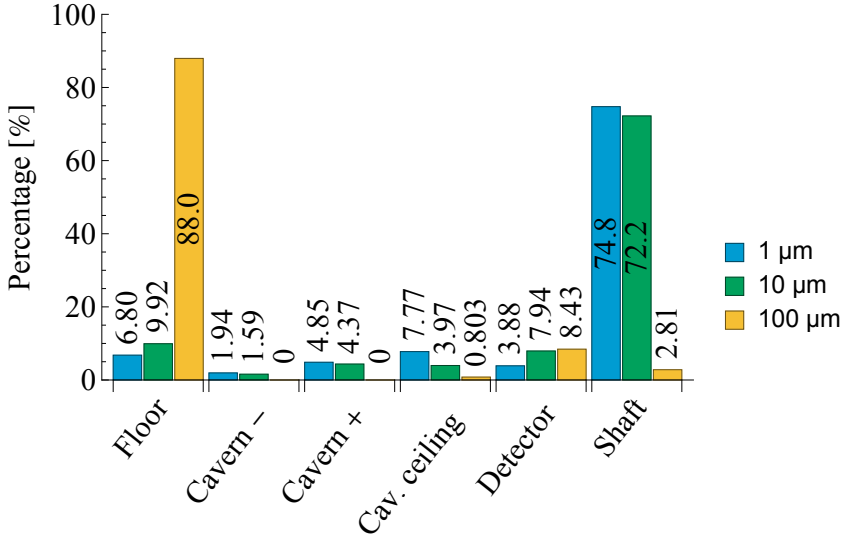

(c) Third patch.

Figure 5.34: Percentages of 1, 10 and 100 μm particles hitting exactly three different patches (1.5 MW, 24 min, cavern open to the surface level, $n_{\text{reb}} = 10,000$)).

Further aerosol results, e.g. of simulations taking into account fire scenarios with varying heat release rates or boundary conditions are only presented in terms of tables. For each scenario release and deposition percentages are given. Percentages have been

always extracted ten minutes after the modeled fire, expressed in terms of different heat release rates, had seized. These additional ten minutes is referred to as "settling time".

As the order of tables follows the flow results presented in section 5.1, the first release table A.21 corresponds to the closed cavern case (1 MW heat release over 20 minutes plus settling time), where release is only possible via the air management system. The term "release inside" expresses the fraction of particles still dispersed inside the volume that has not been finally deposited yet. Table A.21 shows, that about 51% and 32% of the 1 and 10 μm particles are still dispersed in air, while the 100 μm particles have mostly settled. This is also retrieved looking at table A.22, showing the belonging deposition percentages. While most of the larger and heavier 100 μm particles settle on the floor and detector surface, the smaller and lighter 1 and 10 μm particles deposit mainly inside the access shaft, followed by the cavern ceiling and walls. Table A.23 and A.24 show the same case, but for a heat release rate of 1.5 MW over 14 minutes, followed by the settling time. Thus release and deposition percentages are given after 24 minutes. All particle fractions behave quite similarly to the 1 MW case, presented above. This consistent behavior has been found for all cases, where only the heat release rate was varied. The immediate conclusion is, that aerosol release and deposition is independent from the heat release rate, as long as the total amount of energy introduced is approximately the same.

Tables A.25 and A.26 show release and deposition percentages modeling the low extraction mode of the air management system, cf. figure 5.3. Due to the activation of the extraction two minutes after the HRR reaches its quasi steady state, about 12% of 1 and 10 μm particles are extracted, while the 100 μm particles stick to their deposition behavior on floor and detector surface. Using medium extraction mode, about 22% of the 1 and 10 μm particles are extracted by the air management system, cf. tables A.28 and A.27. Thus, an use of the extraction shortly after fire detection is not only able to keep the detector out of any warm or hot temperature layer, it enhances also significantly the situation by partly extracting smoke and its aerosols, not to be further deposited inside the cavern volume.

To assess the impact of a propagating fire, a heat release rate of 1.5 MW was continued over 28 minutes, providing the aerosol release and deposition results shown in tables A.29 and A.30. Both tables compared to the shorter 1.5 MW case presented above show higher deposition percentages for 1 and 10 μm particles with a decrease of dispersed particles of the same size. No significant changes are observed for the 100 μm particles though.

Opening the concrete plug of the access shaft allows thermal plume and aerosols to exit towards the surface. Tables A.31, A.32, A.33 and A.34 show release and deposition percentages for the 1 and 1.5 MW fire scenarios over 20 and 14 minutes, respectively. Compared to the former closed configuration, only little changes are observed related to deposition of particles. However, the 1 and 10 μm percentages of particles dispersed in air show a release of approximately 22% outside of the experimental underground geometry.

In another attempt the removal of the concrete block between the service and experimental cavern in addition to an open access shaft is simulated. Three different heat release rates of 0.5, 1 and 1.5 MW have been used (over 30, 20 and 14 minutes) representing a fire scenario directly beneath the access shaft, thus maximizing the thermal plume carrying along aerosols towards the surface. Tables A.35, A.36, A.37, A.38, A.39 and A.40 provide results on release and deposition percentages for the chimney flow configuration. In each case about 50% of the 1 and 10 μm particles are released to the surface level. A slight increase is noted with increase of heat release rate. Further a significant release of 100 μm particles could be shown, ranging from about 15% up to 27%, depending on the heat release rate, too. Due to the change in the fire position, cavern walls, ceiling and the detector are much less affected by deposition as in all other cases presented above. However, this is conveyed by an increase in deposition along the access shaft. The 1.5 MW case with cross-sections open to the surface level and the adjacent cavern is the worst case found so far in terms of aerosol release. At the same time it is the best in terms of aerosol deposition inside the experimental cavern and the detector surface.

Additional aerodynamic particle diameters have been introduced in order to round off the given results. Tables A.45 and A.46 show percentages for aerosol release and deposition for 1, 5, 10, 50, 75 and 100 μm particles, based on the worst case aerosol release fire scenario identified above. In general, deposition percentages increase with aerodynamic diameter, while release percentages decrease. This is another indication towards a proper verification of the model behavior.

5.2.3 Local interaction sub model

Using the standard local interaction sub model being part of OpenFOAM, particles are not allowed to rebound but either to deposit immediately onto a surface on first contact

("stick"), or, in case the cross-section is not a solid surface but open to the ambient, to escape the domain and thus being counted as released. This model configuration has been used to run cross-check simulations.

All individual results have been found consistent in terms of particle release and deposition to the ones of the limited local interaction rebound model limited to 100 rebounds as presented in section 5.2.2 above. Therefore their interpretation is not repeated here. The results of the different scenarios are given as release and deposition percentages in appendix A, cf. table A.47 to table A.58.

5.2.4 Comparison of interaction sub model configurations in terms of release

So far two different particle interaction sub models have been used. The local interaction rebound sub model, introduced in section 3.3.3 and the local interaction sub model being part of the Lagrangian particle framework of OpenFOAM, cf. section 5.2.3. For both particle interaction sub models a release over time can be extracted. Release is defined as the amount of particles registered above the cross-section between access shaft and surface geometry, i.e. all particles at $y \geq 98\,\mathrm{m}$ at a certain time step t_i. Further, a maximum and minimum release is defined as follows:

- Maximum release takes into account all particles of a certain diameter without regarding the individual number of rebounds value of each particle.
- Minimum release considers only particles of a certain diameter with a number of rebounds value equal to zero, i.e. particles that have never hit a surface during their transport from the experimental cavern up to the surface level.

Figure 5.35 shows maximal and minimal release percentages versus time for 1, 10 and 100 μm particles set to a maximum of 0, 100, 10,000 and unlimited rebounds, for a 1.5 MW experimental cavern case open to the surface level. It was run for 14 minutes, followed by additional 10 minutes of settling time. The highest maximum release value of about 38% at $t = 1440\,\mathrm{s}$ is observed for the 10 μm particles, followed by approximately 30% at the same time step for the 1 μm particles, both particle classes using unlimited rebounds. In both cases, particles with a maximum number of rebounds of 10,000 show a similar behavior. Particles with the same diameters and up to 100 rebounds

level off at around 20% at t = 1440 s, being more consistent with the standard local interaction rebound sub model than with the higher rebound particles. In all four different configurations for the maximum number of rebounds, the 100 μm particles show a release of not more than 2%, which further indicates that they are too heavy to be carried along a thermal plume being redirected from the experimental cavern ceiling towards the access shaft. Further, at some time steps e.g. at t = 600 s the release percentage of the 10 μm particles set to n_{reb} = 100 is higher than for particles of the same diameter but n_{reb} = 10,000. These small differences in percentage are likely caused by the interaction of a transient turbulent air flow and the boundary conditions (different n_{reb} values) of the particles. Similar data has been obtained for the experimental cavern cases open to the surface and the neighboring cavern, discussed below. Looking at the minimum release percentages over time, cf. figure 5.35(b), one concludes that all four different configurations are in a good qualitative and quantitative agreement.

For the experimental cavern case open to both, the surface and the neighboring cavern, similar results are obtained, although with higher percentages. With n_{reb} set to unlimited, a maximum release fraction of about 62% at t = 1440 s could be shown for the 10 μm particles, followed by approximately 59% for the 1 μm particles, cf. figure 5.36(a). Approximately the same values are found for the same particle diameters set to n_{reb} = 10,000. Between t = 800 s and t = 1440 s a difference of up to ten percent is reached between the release fractions for particles set to unlimited or n_{reb} = 10,000 and n_{reb} = 100 or n_{reb} = 0. In general, in both plots in fig. 5.36 the release percentages from t = 100 s to t = 800 s show much more individual trends than shown in figure 5.35. This random behavior is caused due to the change in fire position, resulting in an emerging thermal plume directly upwards the access shaft without impinging the experimental cavern ceiling, cf. sections 5.1.2 and 5.1.3. It explains also the high value of 100 μm particles released, compared to the experimental cavern case open to the surface only, reaching a minimum release fraction of up to 26% at t = 900 s, cf. figure 5.36(b). From this time step onward, a slight decrease of the release fraction for 100 μm particles is visible. A part of the decrease is caused by 100 μm particles settling back into the access shaft of the experimental cavern, thus not longer being counted as released. The other part is explained by 100 μm particles settling on surface level and reaching their final number of rebounds. Here, the 100 μm particles with n_{reb} = 100 reach their final state sooner than the ones with higher n_{reb} values. Starting from t = 800 s a good qualitative and quantitative agreement is shown for the four different n_{reb} value runs.

Both cases of the CMS experimental cavern, the one open to the surface and the one open to the surface and the neighboring, show the advantage of the proposed local interaction rebound sub model for Lagrangian particles. In both cases it provides higher maximum release fractions, while still staying well below the conservative 100% value being applied so far, cf. section 1.2. Furthermore being able to differ between particles with and without any kind of surface interaction allows to provide not only a single release fraction value, but rather release fraction ranges.

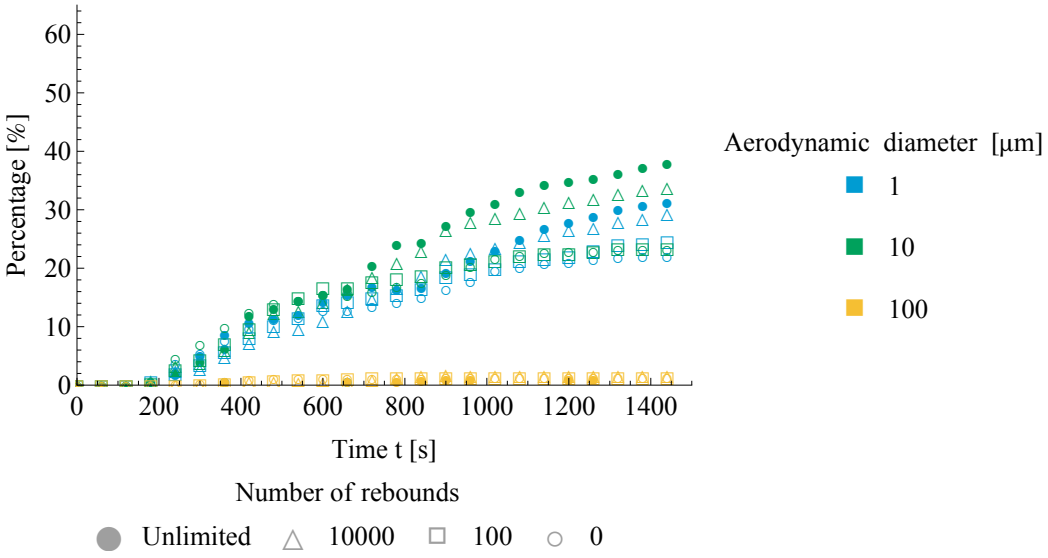

(a) Maximum release percentages.

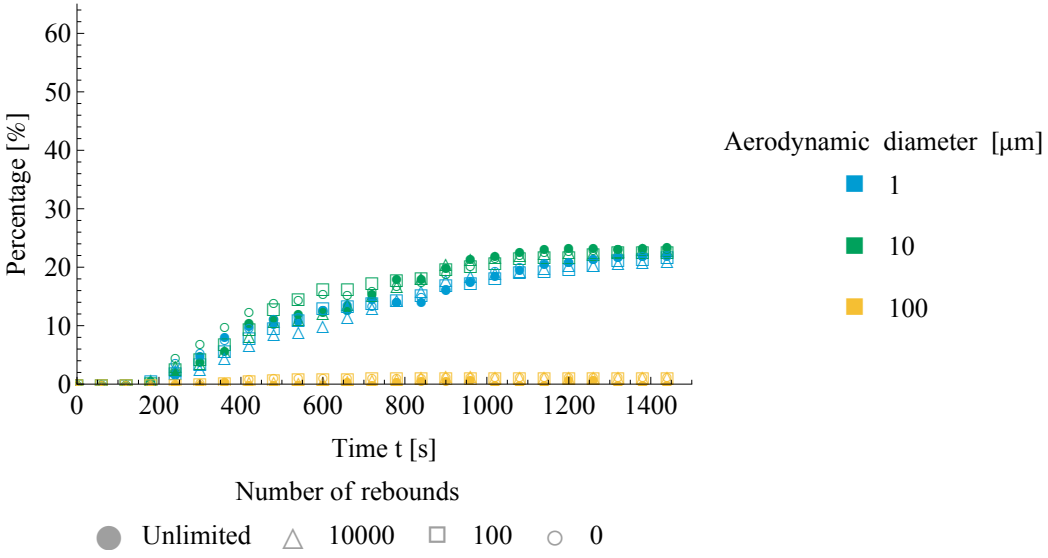

(b) Minimum release percentages.

Figure 5.35: Particle release percentages over time for cavern geometry open to the surface using different particle surface interaction models (1.5 MW, 24 minutes).

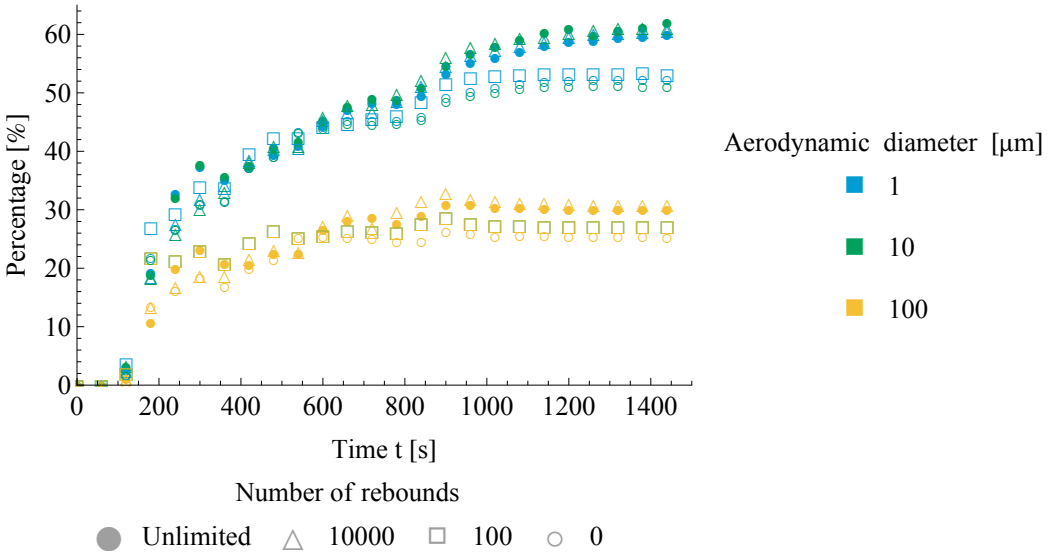

(a) Maximum release percentages.

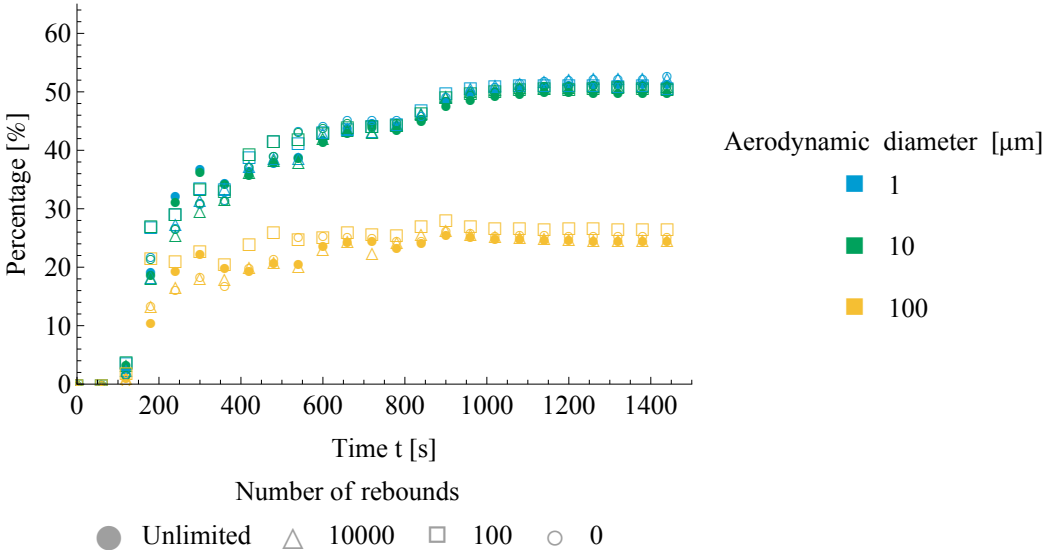

(b) Minimum release percentages.

Figure 5.36: Particle release percentages over time for cavern geometry open to the surface and neighboring cavern using different particle surface interaction models (1.5 MW, 24 minutes).

6 Conclusions and further investigations

Particle collisions, e.g. between protons or ions, cause ionizing radiation. Premises and equipment present during operation of particle accelerators become partially activated. Depending on the level of activation and the composition of a nuclide inventory present, radiation protection measures have to be adapted. Similarly, the level of fire safety has to be optimized in order to mitigate as best as possible any fire incident taking place in supervised, radioactive environments.

In the recent past, fire scenarios at CERN's underground premises involving radioactive material have always been considered in the most conservative way: a complete release of all present nuclides to the surface. To improve the current situation, the author proposed in the present thesis to use CFD modeling of fire scenarios. Simulations of fire-induced thermal plumes, carrying aerosols of discrete aerodynamic diameters modeled by Lagrangian particles provide insight on aerosol release from underground facilities to surface level. A new method for better understanding how and how many particles engage with different surfaces is shown in this thesis.

As complex geometry, the experimental cavern of the CMS Experiment was chosen. By size and volume it is a representative installation of the Large Hadron collider's large-scale experiments. This thesis work was split into understanding two key elements: the flow inside different given geometry variations, i.e. open, closed, based on different fire scenarios and the interaction with the installed air management system as well as an analysis on particle dispersion and deposition inside the experimental cavern.

Regarding the fire-induced flow and resulting temperature and velocity magnitude distributions inside the cavern volume, the closed cavern geometry during operation is the worst case for the detector. Especially a propagating fire due to absence of compensatory measures could lead to an submergence of the detector before CERN's fire and rescue service switches on smoke extraction or intervenes.

In terms of aerosol release to the surface, the cavern geometry open towards its neighboring cavern and the adjacent surface building was found to be the worst configuration

due to a distinct chimney flow. By using two different surface interaction sub models, a lower and upper release fraction of 1, 10 and 100 μm particles could be derived, independent of the prescribed heat release rate of each individual scenario. As all results are given in fractions of different aerodynamic diameters, released or deposited to a certain surface or volume, an universal application is given. Any kind of airborne combustion product, such as soot and other agglomerates of solid and liquid material could be distributed according to the given results. Further, the derived data on particle hits on a certain surface, using unlimited rebounds, provides a residence probability for each aerodynamic particle diameter and specified surface, based on a continuous approach (instead of the intermittent one existing up to now).

For each CFD sub model used in the present thesis, a verification was carried out by adapting known or new test cases. The resulting vector of differences between the particular expectations and computed values indicates the credibility of the model itself and its variations. Together with the lower and upper release fractions it provides a new, unique combination. Each item could be subjected to further optimization by using and improving computational resources available. To the experience gained by the author during his investigations, any kind of complementary in situ validation is out of touch with reality, due to the operational state of the LHC accelerator and its experiments.

Despite the gained, present knowledge, further research has to be carried out, especially on the subject of fire propagation and fire behavior in particle physics accelerator tunnels and underground experiments. Geometries and fire load distributions differ significantly from the ones found e.g. in pedestrian, road and railway tunnels. Taking into account all aspects of ionizing radiation related to research application, an integrated fire and radiation protection concept is advised. Mutual research topics could certainly be found in the domain of aerosol behavior e.g. agglomeration and deposition of radio nuclides, soot or other fire products.

Acknowledgements

The present work has been carried out in the framework of the Doctoral Student Programme at CERN, mostly in the former PH-CMX group. I am most grateful to my CERN thesis supervisor Prof. Dr. rer. nat. Christoph Schäfer for giving me the opportunity to carry out this thesis work, continuous support, countless discussions, an incredible amount of patience and an introduction into a completely different mindset.

Special thanks are due to my university supervisor Prof. Dr.-Ing. habil. Ulrich Krause, for accepting me as remote doctoral student, also continuous support, fruitful discussions and a lot of encouraging exchanges with a good sense of humor. I also appreciate the financial support having been made available by the Institute of Process Equipment and Environmental Engineering.

I am very grateful to Prof. Dr. Enrico Da Riva, for following my scientific career and accepting the challenge to join the scientific board dedicated to my thesis work. I enjoyed our myriads of discussions, the introduction into basic Italian and the art of making good coffee. Grazie mille!

Également un grand merci à JProf. Dr. Benoît Fond pour l'organisation de ma soutenance. C'était un grand plaisir.

The work presented in this thesis has been mainly funded by the Wolfgang-Gentner-Programme at CERN. I would like to express my gratitude to the programme coordinator Dr. Michael Hauschild, for continuous administrative and financial support and a lot of good discussions as well.

Further financial support has been provided by the CMS collaboration at CERN, for which I would like to thank the technical coordinators Dr. Austin Ball and Dr. Wolfram Zeuner. It has been a pleasure to work with you in such an international and vibrant environment.

I am also very grateful to Dr. Doris Forkel-Wirth for her kind help in numerous discussions on the integration of fire safety and radiation protection. Similarly, I appreciate the financial support and computing resources provided by CERN's radiation protection group. Especially the help of my "Austrian fan club" concerning ionizing radiation, provided by Prof. Dr. Helmut Vincke and Dr. Chris Theis shall not go unnoticed.

For insights into top level RF research, an advanced crash course in Mathematica and, even more important, permanent encouragement in combination with a sharp wit I am highly grateful to Dr. Christine Völlinger.

A big "thank you" is also due to Marc Dobson, Nils Høimyr, Michal Husejko, Fernando Pereira and Attila Racz for their kind help and support on high performance computing. Special thanks are also due to the FM Global fireFoam team, in particular Dr. Prateep

Chatterjee and Dr. Karl Meredith, CERN's CFD team past and present members and Dr. Dominik Christ as well as Prof. Dr. Hrvoje Jasak, Wikki Ltd., for their patient help in understanding OpenFOAM source code and providing the interaction sub model.

I would like to thank my university colleagues Dr. Dieter Gabel, Dr. Sarah Hahn, Christian Kusche, Dr. Thomas Melcher, Alexander Saupe, Stephanie Schubert, Christoph Wanke and Dr. Ronald Zinke for their encouragement and a lot of interesting exchanges. Thanks are also due to Jan Deubel and Martin Werrel for their inspiration and motivation to join fire research.

Without Bernhard Linseisen I would not have been aware, neither of CERN nor of the scholarship programme I have been accepted for. Dankschee Bernhard!

Finally, I am very grateful to my friends and family, for their continuous encouragement, patience, distractions and support over all the time it took.

Bibliography

[1] Thomas E. Widner and Susan M. Flack. Characterization of the World's First Nuclear Explosion, the Trinity Test, as a Source of Public Radiation Exposure. *Health Physics*, 98(3):480–497, March 2010.

[2] http://www.cern.ch.

[3] Lyndon Evans and Philip Bryant. LHC Machine. *Journal of Instrumentation*, 3(S08001), 2008.

[4] Lyndon Evans, editor. *The Large Hadron Collider: A Marvel of Technology*. EPFL Press, Lausanne, Switzerland, 1 edition, 2009.

[5] Julie Haffner. The CERN accelerator complex. Complexe des accélérateurs du CERN. OPEN-PHO-ACCEL-2013-056, http://cds.cern.ch/record/1621894, Oct 2013.

[6] ALICE collaboration. The ALICE Experiment at the CERN LHC. *Journal of Instrumentation*, 3(S08002), 2008.

[7] ATLAS collaboration. The ATLAS Experiment at the CERN Large Hadron Collider. *Journal of Instrumentation*, 3(S08003), 2008.

[8] CMS collaboration. The CMS Experiment at the CERN LHC. *Journal of Instrumentation*, 3(S08004), 2008.

[9] The LHCb collaboration. The LHCb Experiment at the CERN LHC. *Journal of Instrumentation*, 3(S08005), 2008.

[10] The LHCf collaboration. The LHCf Experiment at the CERN Large Hadron Collider. *Journal of Instrumentation*, 3(S08006), 2008.

[11] The TOTEM collaboration. The TOTEM Experiment at the CERN Large Hadron Collider. *Journal of Instrumentation*, 3(S08007), 2008.

[12] CMS Collaboration. Detector Drawings. CMS-PHO-GEN-2012-002, http://cds.cern.ch/record/1433717, March 2012.

[13] Charles-Eduard Sala, Pavol Vojtyla, and Joachim Vollaire. Rapport Provisoire de Sûreté du SPS/CNGS et du LHC - Section II.3 Conséquences du Fonctionnement Normal et du Fonctionnement Dégradé sur les Travailleurs et sur l'Environment. Technical Report EDMS 634779, European Organization for Nuclear Research, Geneva, Switzerland, August 2011.

[14] Charles-Eduard Sala, Helmut Vincke, and Pavol Vojtyla. Rapport Provisoire de Sûreté du SPS/CNGS et du LHC - Section II.4 Étude des Accidents. Technical Report EDMS 634782, European Organization for Nuclear Research, Geneva, Switzerland, August 2008.

[15] Sabine Pfister. *Grundlagen für die Anwendung numerischer Strömungssimulation auf Brandszenarien in Industrieanlagen.* PhD thesis, Technische Universität Berlin, Berlin, Germany, 2012.

[16] Matthias Münch. *Konzept zur Absicherung von CFD-Simulationen im Brandschutz und der Gefahrenabwehr.* PhD thesis, Otto-von-Guericke-University Magdeburg, Magdeburg, Germany, 2012.

[17] http://code.google.com/p/firefoam-dev/.

[18] http://sites.google.com/site/firemodelingworkshop/home.

[19] Roberto Saban. EDMS 107398: Naming Conventions for Buildings and Civil Engineering Works. Technical report, European Organization for Nuclear Research (CERN), 1999.

[20] Anonymous. Code de Securité E: Protection contre l'Incendie. Technical report, European Organization for Nuclear Research (CERN), 1995.

[21] Anonymous. Safety Instruction IS23 Rev. 3: Criteria and Standard Test Methods for the Selection of Electric Cables and Wires with Respect to Fire Safety and Radiation Resistance. Technical report, European Organization for Nuclear Research (CERN), 2005.

[22] Anonymous. Safety Instruction IS41 Rev. 1: The Use of Plastic and other Non-Metallic Materials at CERN with respect to Fire Safety and Radiation Resistance. Technical report, European Organization for Nuclear Research (CERN), 2005.

[23] Ordonnance sur la radioprotection. Swiss regulation 814.501, 1994.

[24] Stefano Fratianni. Edms 399800: Derogation for 30 t of borated polyethylene. Technical report, European Organization for Nuclear Research (CERN), 2003.

[25] Michael Plagge and Wolfram Zeuner. EDMS 1527754: Preshower fire safety review update due to LHC LS1 changes. Technical report, European Organization for Nuclear Research (CERN), 2015.

[26] Rui Nunes and Floris Bonthond. EDMS 397064: Automatic Fire Detection System for the LHC Underground Areas. Technical report, European Organization for Nuclear Research (CERN), 2004.

[27] Zoltan Szilasi (CERN EP-UCM). Personal communication, May 2015.

[28] Silvia Grau. EDMS 537182: The SNIFFER Project. Technical report, European Organization for Nuclear Research (CERN), 2006.

[29] Niels Dupont-Sagorin, Christoph Schäfer, and Niels van Veen. EDMS 963887: Predefined Reactions to "Level 3" Alarms and Incidents/Accidents at Point 5 for the CMS Experiment. Technical report, European Organization for Nuclear Research (CERN), 2011.

[30] Anonymous. EDMS 1250205: Protection de chaînes à cables CERN Point 5 - Rapport de Fin d'Intervention Dossier "Tel Que Construit". Technical report, European Organization for Nuclear Research (CERN), 2004.

[31] Nuno Dos Santos. EDMS 766676: CO2 protection system installation for racks, in S1 and S2 floor of USC55 cavern. Technical report, European Organization for Nuclear Research (CERN), 2004.

[32] Anonymous. EDMS 932610: Air Handling Installations of the Two Experimental Areas at Points 1 and 5 of the LHC - Point 5 CMS - General LHC Ventilation Plant Configurations Considering LHC Status and Fire/Smoke/Gas Safety Conditions, Revision A (as-built). Technical report, European Organization for Nuclear Research (CERN), 2008.

[33] Bernard Pirollet. EDMS 932610: The CMS Ventilation System. Technical report, European Organization for Nuclear Research (CERN), 2008.

[34] Geir Jensen. Hypoxic air venting for protection of heritage. Technical report, Riksantikvaren the Norwegian Directorate for Cultural Heritage and Hostoric Scotland: Technical Conservation, Research and Education group, 2006.

[35] Anonymous. PAS 95:2011 Hypoxic air fire prevention systems – Specification. Technical report, British Standards Institution BSI, London, United Kingdom, 2011.

[36] Michael Plagge. EDMS 1213276: Review of the CMS foam extinguishing system. Technical report, European Organization for Nuclear Research (CERN), 2013.

[37] Code du travail, Partie réglementaire, 4. Partie: Santé et Sécurité au travail, 1. Titre: Obligations du Maître d'ouvrages pour la conception des lieux de travail, Chapitre VI: Risques d'incendies et d'explosions et évacuation, Section 2: Dégagements. Décret no 2008-244 du 7 mars 2008.

[38] Niels Dupont-Sagorin. EDMS 1216621: Formation/exercice d'evacuation CMS, cavernes USC55 et UXC55. Technical report, European Organization for Nuclear Research (CERN), 2012.

[39] Geroge V. Hadjisophocleous and Jim R. Mehaffey. *Fire Scenarios*, chapter 11, section 5. SFPE Handbook of Fire Protection Engineering. National Fire Protection Association, Quincy, Massachusetts, United States of America, 4. edition, 2008.

[40] Angela Harrison. *Risk Analysis of the LHC underground area - Fire risk due to faulty electrical equipment.* Cern-thesis-2007-044, Institute for Process Technology and Industrial Environmental Protection, University of Leoben, Leoben, Austria, 2007.

[41] NFPA 70: National Electric Code. Technical report, National Fire Protection Association, Quincy, United States of America, 2014.

[42] J. Mangs, J. Paananen, and O. Keski-Rahkonen. Calorimetric fire experiments on electronic cabinets. *Fire Safety Journal*, 38(2):165 – 186, 2003.

[43] IEC 60332-3-24:2000 Test for vertical flame spread of vertically-mounted bunched wires or cables - Category C. Technical report, International Electrotechnical Commission, Geneva, Switzerland, 2000.

[44] Adam B. Stein, Ephraim M. Sparrow, and John M. Gorman. Numerical simulation of cables in widespread use in the nuclear power industry subjected to fire. *Fire Safety Journal*, 53:28–34, 2012.

[45] J. M. Chavez. An experimental investigation of internally ignited fires in nuclear power plant control cabinets, Part 1: Cabinet effects tests, NUREG/CR-4527/1, SAND86-0336. Technical report, Sandia National Laboratories, 1987.

[46] Anonymous. ISO/TR 13387-2:1999 Fire safety engineering – Part 2: Design fire scenarios and design fires. Technical report, International Organization for Standardization, Geneva, Switzerland, 1999.

[47] W. Plumecocq, M. Coutin, S. Melis, and L. Rigollet. Characterization of closed-doors electrical cabinet fires in compartments. *Fire Safety Journal*, 46(5):243 – 253, 2011.

[48] M. Coutin, W. Plumecocq, S. Melis, and L. Audouin. Energy balance in a confined fire compartment to assess the heat release rate of an electrical cabinet fire. *Fire Safety Journal*, 52(0):34 – 45, 2012.

[49] L. Audouin, L. Rigollet, H. Prétrel, W. Le Saux, and M. Röwekamp. OECD PRISME project: Fires in confined and ventilated nuclear-type multi-compartments - overview and main experimental results. *Fire Safety Journal*, 62, Part B:80 – 101, 2013. Special Issue on PRISME – Fire Safety in Nuclear Facilities.

[50] Dietmar Hosser. Leitfaden Ingenieurmethoden des Brandschutzes - 3rd Edition. Technical Report TB 04-01, Vereinigung zur Förderung des deutschen Brandschutzes (vfdb), Altenberge, Germany, November 2013.

[51] Gert Beilicke. *Brandschutz - Brandlastberechnung.* Rudolf Haufe Verlag, Berlin, Germany, 1. edition, 1990.

[52] H. Prétrel, W. Le Saux, and L. Audouin. Pressure variations induced by a pool fire in a well-confined and force-ventilated compartment. *Fire Safety Journal*, 52(0):11–24, 2012.

[53] S. Vaux and H. Prétrel. Relative effects of inertia and buoyancy on smoke propagation in confined and forced ventilated enclosure fire scenarios. *Fire Safety Journal*, 62, Part B(0):206 – 220, 2013. Special Issue on PRISME – Fire Safety in Nuclear Facilities.

[54] http://www.fire.nist.gov/fds/.

[55] Guan Heng Yeoh and Kwok Kit Yuen. *Computational Fluid Dynamics in Fire Engineering.* Elsevier, Inc., Oxford, United Kingdom, 1. edition, 2009.

[56] Morgan J. Hurley, Daniel Gottuk, John R. Hall Jr., Kazunori Harada, Erica Kuligowski, Milosh Puchovsky, John M. Watts Jr., and Christopher Wieczorek, editors. *SFPE Handbook of Fire Protection Engineering.* Springer, New York Heidelberg Dordrecht London, 5. edition, 2015.

[57] http://www.firegrowthmodel.ca/index.php.

[58] http://www.fs.fed.us/pnw/fera/wfds/index.shtml.

[59] http://www.openwfm.org.

[60] Francesco Collela. *Multiscale Modeling of Tunnel Ventilation Flows and Fires.* PhD thesis, Dipartimento di Energetica, Politecnico di Torino, Torino, Italy, May 2010.

[61] Christopher William Lautenberger. *A Generalized Pyrolysis Model for Combustible Solids*. PhD thesis, University of California, Berkeley, Dezember 2007.

[62] http://www.fmglobal.com/page.aspx?id=04010400.

[63] Arnaud Trouvé and Yi Wang. Large eddy simulation of compartment fires. *International Journal of Computational Fluid Dynamics*, 24(10):449–466, 2010.

[64] FM Global. http://www.fmglobalreason.com/article/real-team-effort, 2010.

[65] FM Global. http://www.fmglobalreason.com/article/model-citizens, 2014.

[66] Yi Wang, Prateep Chatterjee, and John L. de Ris. Large eddy simulation of fire plumes. *Proceedings of the Combustion Institute*, 33(2):2473 – 2480, 2011.

[67] Gunnar Heskestad. *Fire Plumes, Flame Height, and Air Entrainment*, chapter 1, Section 2. SFPE Handbook of Fire Protection Engineering. National Fire Protection Association, Quincy, Massachusetts, United States of America, 4th edition, 2008.

[68] Prateep Chatterjee, Karl V. Meredith, Benjamin Ditch, Hong-Zeng Yu, Yi Wang, and Francesco Tamanini. Numerical Simulations of Strong-Plume Driven Ceiling Flows. In *Proceedings of the 11th IAFSS Symposium*, 2014.

[69] Karl V. Meredith, Jaap de Vries, Yi Wang, and Yibing Xin. A comprehensive model for simulating the interaction of water with solid surfaces in fire suppression environments. In *Proceedings of the Combustion Institute*, volume 34, pages 2719–2726, 2013.

[70] Marcos Chaos, Mohammed M. Khan, Niveditha Krishnamoorthy, John L. de Ris, and Sergey B. Dorofeev. Evaluation of optimization schemes and determination of solid fuel properties for CFD fire models using bench-scale pyrolysis tests. *Proceedings of the Combustion Institute*, 33(2):2599 – 2606, 2011.

[71] Niveditha Krishnamoorthy, Marcos Chaos, Mohammed M. Khan, Prateep Chatterjee, Yi Wang, and Sergey B. Dorofeev. Application of bench-scale material flammability data to model flame spread in medium-scale parallel panel test. In *Proceedings of the 12th International Conference*, London, United Kingdom, 2010. InterFlam, Interscience Communications Ltd.

[72] Prateep Chatterjee, Niveditha Krishnamoorthy, Yi Wang, John L. de Ris, and Sergey B. Dorofeev. CFD simulation of radiative heat transfer between a buoyant turbulent fire and inert parallel panels. In *Proceedings of the 12th International Conference*, London, United Kingdom, 2010. InterFlam, Interscience Communications Ltd.

[73] Prateep Chatterjee, John L. de Ris, Yi Wang, and Sergey B. Dorofeev. A model for soot radiation in buoyant diffusion flames. *Proceedings of the Combustion Institute*, 33(2):2665 – 2671, 2011.

[74] Karl V. Meredith and Xiangyang Zhou. A Spray Interaction Model with Application to Surface Film Wetting. In *12th Triannual International Conference on Liquid Atomization and Spray Systems*, pages 1–8, Heidelberg, Germany, September 2012.

[75] Karl V. Meredith, Yibing Xin, and Jaap de Vries. A numerical model for simulation of thin-film water transport over solid fuel surfaces. In *Proceedings of the 10th IAFSS Symposium*, pages 415–428. International Association of Fire Safety Science, 2011.

[76] Yi Wang, Karl V. Meredith, Xiangyang Zhou, Prateep Chatterjee, Yibing Xin, Marcos Chaos, Ning Ren, and Sergey B. Dorofeev. Numerical simulation of sprinkler suppression of rack storage fires. In *Proceedings of the 11th IAFSS Symposium*, pages 1170–1183. International Association of Fire Safety Science, 2014.

[77] D. A. Purser and J. L. McAllister. *Assessment of Hazards to Occupants from Smoke, Toxic Gases, and Heat*, volume III, Section 63 of *SFPE Handbook of Fire Protection Engineering*. National Fire Protection Association, Quincy, Massachusetts, United States of America, 5th edition, 2015.

[78] OpenFOAM Foundation. *OpenFOAM User Guide Version 2.2.2*, 2013.

[79] OpenFOAM Foundation. *OpenFOAM Programmer's Guide Version 2.2.2*, 2013.

[80] Niklas Nordin. *Complex Chemistry Modeling of Diesel Spray Combustion*. PhD thesis, Chalmers University of Technology, Gothenburg, Sweden, 2001.

[81] William C. Hinds. *Aerosol Technology*. John Wiley & Sons, Inc., New York, 1st edition, 1982.

[82] Paul A. Saunders. *Principles of Aerosol Technology*. Van Nostrand Reinhold Company, New York, 1st edition, 1970.

[83] Anonymous. *ANSYS Fluent Theory Guide*. ANSYS, Inc., Canonsburg, Pennsylvania , United States of America, November 2013.

[84] Kevin McGrattan, Simo Hostikka, Randall McDermott, Jason Floyd, Craig Weinschenk, and Kris Overholt. NIST Special Publication 1018-1, Fire Dynamics Simulator Technical Reference Guide Volume 1: Mathematical Model. Technical report, National Institute of Standards and Technology, Gaithersburg, Maryland, USA, November 2015.

[85] Michael F. Modest. *Radiative Heat Transfer*. Academic Press, New York San Francisco London, 3rd edition, 2013.

[86] http://openfoam.org/download/2-2-2-source/.

[87] Fernando F. Grinstein, Len G. Margolin, and William J. Rider. *Implicit Large Eddy Simulation*. Cambridge University Press, New York, 2007.

[88] Stephen B. Pope. *Turbulent flows*. Cambridge University Press, Cambridge, United Kingdom, 2000.

[89] D.B. Spalding. A Single Formula for the "Law of the Wall". *Journal of Applied Mechanics*, 28(3):455–458, 1961.

[90] Hrvoje Jasak. *Error Analysis and Estimation for the Finite Volume Method with Applications to Fluid Flows*. PhD thesis, Imperial College of Science, Technology and Medicine, London, United Kingdom, 1996.

[91] Tomislav Marić, Jens Höpken, and Kyle Mooney. *The OpenFOAM Technology Primer*. Sourceflux UG, Duisburg, Germany, 1st edition, 2014.

[92] Joel H. Ferziger and Milovan Perić. *Computational Methods for Fluid Dynamics*. Springer Verlag, Berlin Heidelberg New York, 2nd edition, 2002.

[93] FM Global. fireFoam solver repository, https://github.com/fireFoam-dev.

[94] John David Anderson. *Computational Fluid Dynamics - The basics with applications*. McGraw-Hill, Inc., 1995.

[95] H. K. Versteeg and W. Malalasekera. *An Introduction to Computational Fluid Dynamics*. Pearson Education Limited, Essex, United Kingdom, 2nd edition, 2007.

[96] Anonymous. ISO 16730-1:2015 Fire safety engineering — Procedures and requirements for verification and validation of calculation methods — Part 1: General. Technical report, International Organization for Standardization, Geneva, Switzerland, 2015.

[97] I.F.I. Institut für Industrieaerodynamik GmbH, Aachen, Germany. http://www.ifi-aachen.de/en/content/real-fire-tests.

[98] Kathrin Grewolls. *Probabilistic Modelling of Sensitivity in Fire Simulations*. PhD thesis, University of Central Lancashire, Preston, Lancashire, United Kingdom, 2013.

[99] Christian Knaust. *Modellierung von Brandszenarien in Gebäuden*. PhD thesis, Fakultät Bauingenieurwesen, Technische Universität Wien, Wien, Österreich, 2009.

[100] Gunnar Heskestad. Engineering relations for fire plumes. *Fire Safety Journal*, 7(1):25–32, 1984.

[101] Prateep Chatterjee. Personal communication, 2013.

[102] Randall McDermott, Kevin McGrattan, Simo Hostikka, and Jason Floyd. NIST Special Publication 1018-5, Fire Dynamics Simulator (Version 5) – Technical Reference Guide, Volume 2: Verification. Technical report, National Institute of Standards and Technology, Gaithersburg, Maryland, USA, April 2010.

[103] Michael Plagge and Matthias Münch. Bug oder feature? Über numerische lichschutzfaktoren im fvDOM-Strahlungsmodell. In *4. Magdeburger Brand- und Explosionsschutztag / 3. vfdb Workshop Brandschutzforschung*, March 2015.

[104] Dougal Drysdale. *An Introduction to Fire Dynamics*. John Wiley & Sons, 3. edition, 2011.

[105] Frank P. Lees. *Loss Prevention in the Process Industries: Hazard Identification, Assessment and Control*, volume 3. Butterworth-Heinemann, Oxford, United Kingdom, 2 edition, 1996.

[106] Bil Kleb and Bill Wood. CFD: A Castle in the Sand? In *34th AIAA Fluid Dynamics Conference*, CFD Verification and Validation session 88-FD-22. The American Institute of Aeronautics and Astronautics, 2004.

[107] Michael Plagge, Ulrich Krause, and Christoph Schäfer. CFD Calculations of Design Fire Scenarios for Experimental Underground Installations at CERN. In *3. Magdeburger Brand- und Explosionsschutztag / 2. vfdb Workshop Brandschutzforschung*, March 2013.

[108] Doris Forkel-Wirth. Personal communication, 2013.

[109] http://www.pvfs.org/.

[110] Mickaël Coutin. Phenomenological description of actual electrical cabinet fires in a free atmosphere. In *INTERFLAM 2007: Proceedings of the eleventh international conference*, pages 725–730, 2007.

[111] Dominik Marek Christ. Personal communication, Wikki Ltd. London, 2012-2014.

[112] C. Fureby, G. Tabor, H.G. Weller, and A. D. Gosman. A comparative study of subgrid scale models in homogeneous isotropic turbulence. *Physics of Fluids*, 9(5):1416–1429, May 1996.

[113] Dominik Marek Christ. *The Effect of Char Kinetics on the Combustion of Pulverized Coal under Oxyfuel Conditions*. PhD thesis, Faculty of Mechanical Engineering, Rheinisch-Westfälische Technische Hochschule Aachen, Aachen, Germany, 2013.

[114] Christopher W. Lautenberger, John L. de Ris, Nicholas A. Dembsey, Jonathan R. Barnett, and Howard R. Baum. A simplified model for soot formation and oxidation in CFD simulation of non-premixed hydrocarbon flames. *Fire Safety Journal*, 40(2):141–176, 2005.

[115] Christopher William Lautenberger. CFD Simulation of Soot Formation and Flame Radiation. Master's thesis, Worcester Polytechnic Institute, Worcester, Januar 2002.

[116] D. R. Stull and H. Prophet. NSRDS-NBS 37: JANAF Thermochemical tables. Technical report, National Bureau of Standards, Washington D.C., U.S.A., 1971.

[117] William Sutherland. LII. The viscosity of gases and molecular force. *Philosophical Magazine Series*, 5(36:223):507–531, 1893.

[118] Bruce E. Poling, John M. Prausnitz, and John P. O'Connell. *The properties of gases and liquids*. McGraw-Hill, Inc., New York San Francisco London, fifth edition, 2001.

[119] R. I. Issa. Solution of the implicitly discretised fluid flow equations by operator-splitting. *Journal of Computational Physics*, 62(1):40 – 65, 1986.

[120] Suhas V. Patankar. *Numerical Heat Transfer and Fluid Flow*. Hemisphere Publishing Corporation, United States of America, 1. edition, 1980.

[121] OpenFOAM Foundation. *OpenFOAM Version 2.2.2 Source Code Documentation*, September 2013.

Appendix A

Tables

Table A.1: Inner dimensions of the underground experimental cavern UXC55.

	m	Reference drawing
Length	53.1	LHC-GSG1352540021
Width	26.6	LHC-GSG135254003
Height	24.2	LHC-GSG135254003
Shaft height	73.8	LHC-PDP135000003
Shaft diameter	20.5	LHC-PDP135000003

Table A.2: Comparison of literature data on open electrical cabinet fires.

Peak HRR kW	Energy released MJ	Fire duration min	Source -
995	1051	15	[45]
1636	1206	>60	[110]
1174	1115	>60	[110]

Table A.3: Derived fire load values for electrical cabinets based on literature data.

Cabinet size Width x Depth X Height m	Derived fire load $MJ \cdot m^{-2}$	Source -
0.914 x 0.762 x 2.29	1509	[45]
1.2 x 0.6 x2	1161	[110]
0.6 x 0.58 x 2.25	1161	[42]
1 x 1 x -	400	[50]

Table A.4: Relative error values for 5 and 10 cm uniform grid sizes.

Coordinate m	$X_{\min}$ %	$X_{\max}$ %	$\bar{X}$ %	σ_X ($\gamma = 0.95$) %	ΔX %	$X_i \geq 50\%$ - (%)
$y = 6.325$	0.03	88.3	18.9	18.4	3.9	7 (8)
$y = 15.025$	0.16	269.9	26	42.8	9	16 (18)
$z = 4.0975$	0	31.1	7.3	8.1	0.84	0 (0)
$z = 5.7625$	0	102.4	12.4	18	1.86	26 (7.2)

Table A.5: Relative error values for 10 and 20 cm uniform grid sizes.

Coordinate m	$X_{\min}$ %	$X_{\max}$ %	$\bar{X}$ %	σ_X ($\gamma = 0.95$) %	ΔX %	$X_i \geq 50\%$ - (%)
$y = 6.325$	0.5	226.5	20.5	27.2	5.7	2 (2.2)
$y = 15.025$	0.01	960.3	47.6	113.2	23.8	18 (20.2)
$z = 4.0975$	0	893.9	60.1	159.4	16.5	43 (12)
$z = 5.7625$	0	263.9	31.3	43.1	4.5	83 (23.1)

Table A.6: Influence of mesh size on particle positions.

Direction	Deviation between 5 and 10 cm cells m	Deviation between 5 and 20 cm cells m	Deviation between 10 and 20 cm cells m
x	$2 \cdot 10^{-7}$	$4 \cdot 10^{-7}$	$2 \cdot 10^{-7}$
y	$7 \cdot 10^{-7}$	$1.1 \cdot 10^{-6}$	$4 \cdot 10^{-7}$
z	$7 \cdot 10^{-7}$	$1.1 \cdot 10^{-6}$	$4 \cdot 10^{-7}$

Table A.7: Thermal radiation heat flux depending on number of solid angles and uniform mesh size obtained by the fvDOM sub model.

Cell size	Number of solid angles		Absolute deviation	
	72	128	72	128
cm	$kW \cdot m^{-2}$	$kW \cdot m^{-2}$	%	%
2.5	99.9	87.6	7.3	5.8
5	95.8	90.0	3.0	3.3
10	91.7	91.0	1.4	2.2
20	89.2	90.6	4.1	2.6
40	88.9	90.6	4.4	2.6
	Analytical value: $93\,kW \cdot m^{-2}$		100%	

Table A.8: Pressure, turbulent kinetic energy and velocity iteration data for 5, 10 and 20 cm uniform grid sizes.

	5 cm	10 cm	20 cm
p_{1st}	39,911	43,595	36,070
p_{2nd}	136,625	90,275	55,755
k	15,013	15,006	15,003
u_y	30,719	30,009	17,685
u_z	31,108	30,021	17,237
Total	253,376	208,906	141,750

Table A.9: Mean and maximum Courant number for 5, 10 and 20 cm uniform grid sizes (highest individual values found are shown).

	5 cm	10 cm	20 cm
Mean	0.18	0.08	0.04
Max	0.4	0.17	0.08

Table A.10: Numerical schemes.

Term	Scheme
Time derivative	Euler
Gradient	Gauss linear
Surface normal gradient	Corrected
Divergence	Gauss limited linear[a]
Laplace	Gauss linear corrected
Interpolation	Linear

[a] For k, an upwind scheme has been used.

Table A.11: Numerical solvers.

	ρ (G)	p (p_{final})	Y_i, k, h	u_i ($u_{i,\text{final}}$)	I_i
Solver	PCG	GAMG	PBiCG	PBiCG	GAMG
Pre conditioner	DIC	-	DILU	DILU	-
Tolerance	0 (10^{-6})	10^{-5} (10^{-6})	10^{-8}	10^{-6} (10^{-7})	10^{-4}
Relative tolerance	0	0.01 (0)	0	0	0

Table A.12: Verification matrix.

Sub model / assumption	Maximum difference / relative error %
Mesh independency	up to 60.1% ± 16.5
Flow boundary conditions	1
Heat release rate	20
Lagrangian parcels	5
Thermal radiation	8
Absence of thermal radiation	30

Table A.13: Patch counts for UXC case open to the surface level, 1.5 MW, 14 minutes (840 s), unlimited rebounds.

	1 μm	10 μm	100 μm
0	5340	4622	1041
1	4197	4264	7133
2	434	1006	1547
3	27	98	182
4	2	10	45
5	0	0	22
6	0	0	18
7	0	0	9
8	0	0	3
9	0	0	0
10	0	0	0

Table A.14: Total patch hit values for UXC case open to the surface level, 1.5 MW, 14 minutes (840 s), unlimited rebounds.

	1 μm	10 μm	100 μm
Single patch	16,607,213	62,132,433	965,842,382
Multiple patches	2,124,233	18,482,960	178,025,412
Total	18,731,446	80,615,393	1,143,867,794

Table A.15: Patch counts for UXC case open to the surface level, 1.5 MW, 24 minutes (1440 s), unlimited rebounds.

	1 μm	10 μm
0	3627	3154
1	5087	4526
2	1133	1866
3	146	392
4	7	60
5	0	2
6	0	0
7	0	0
8	0	0
9	0	0
10	0	0

Table A.16: Total patch hit values for UXC case open to the surface level, 1.5 MW, 24 minutes (1440 s), unlimited rebounds.

	1 μm	10 μm
Single patch	38,056,306	179,561,772
Multiple patches	10,022,972	91,894,891
Total	480,79,278	271,456,663

Table A.17: Patch counts for UXC case open to the surface level, 1.5 MW, 24 minutes (1440 s), rebounds limited to 100.

	1 μm	10 μm	100 μm
0	3681	3265	126
1	5929	6625	9537
2	380	110	328
3	10	0	9
4	0	0	0
5	0	0	0
6	0	0	0
7	0	0	0
8	0	0	0
9	0	0	0
10	0	0	0

Table A.18: Total patch hit values for UXC case open to the surface level, 1.5 MW, 24 minutes (1440 s), rebounds limited to 100.

	1 μm	10 μm	100 μm
Single patch	551,016	644,295	948,130
Multiple patches	36,836	10,974	33,700
Total	587,852	655,269	981,830

Table A.19: Patch counts for UXC case open to the surface level, 1.5 MW, 24 minutes (1440 s), rebounds limited to 10,000.

	1 μm	10 μm	100 μm
0	3926	3246	134
1	4974	5054	7595
2	990	1414	1807
3	103	252	249
4	6	29	82
5	0	5	63
6	1	0	40
7	0	0	22
8	0	0	7
9	0	0	0
10	0	0	1

Table A.20: Total patch hit values for UXC case open to the surface level, 1.5 MW, 24 minutes (1440 s), rebounds limited to 10,000.

	1 μm	10 μm	100 μm
Single patch	20,164,720	22,192,979	74,333,319
Multiple patches	2,072,002	10,609,129	22,494,848
Total	22,236,722	32,802,108	96,828,167

Table A.21: Release percentages for closed UXC case, 1 MW, 31 minutes (1860 s), rebounds limited to 100.

	1 μm	10 μm	100 μm
Release outside	0.12	0.29	0.16
Release inside	51.39	32.17	0.

Table A.22: Deposition percentages for closed UXC case, 1 MW, 31 minutes (1860 s), rebounds limited to 100.

	1 μm	10 μm	100 μm
Shaft	22.83	32.28	0.74
Floor	0.02	0.61	41.36
Cavern -	9.98	12.25	4.93
Cavern +	2.91	4.21	0.11
Detector	2.38	4.62	50.09
Cavern ceiling	10.37	13.57	2.61
Total	48.49	67.54	99.84

Table A.23: Release percentages for closed UXC case, 1.5 MW, 24 minutes (1440 s), rebounds limited to 100.

	1 μm	10 μm	100 μm
Release outside	0.17	0.25	0.2
Release inside	54.38	33.76	0.05

Table A.24: Deposition percentages for closed UXC case, 1.5 MW, 24 minutes (1440 s), rebounds limited to 100.

	1 μm	10 μm	100 μm
Shaft	21.67	31.04	1.94
Floor	0.07	0.69	42.61
Cavern -	0.03	11.72	6.
Cavern +	2.1	3.96	0.13
Detector	1.94	4.62	45.74
Cavern ceiling	10.7	13.96	3.33
Total	36.51	65.99	99.75

Table A.25: Release percentages for closed UXC case, 1.5 MW, 24 minutes (1440 s), rebounds limited to 100, low extraction mode.

	1 μm	10 μm	100 μm
Release outside	0.	0.	0.
Release inside	43.98	27.91	0.04

Table A.26: Deposition percentages for closed UXC case, 1.5 MW, 24 minutes (1440 s), rebounds limited to 100, low extraction mode.

	1 μm	10 μm	100 μm
Shaft	20.22	28.35	2.02
Floor	0.05	0.24	40.65
Cavern -	8.86	11.49	5.85
Cavern +	1.79	3.13	0.24
Detector	1.69	3.35	46.44
Extraction outlet	13.03	11.5	1.69
Cavern ceiling	10.38	14.03	3.07
Total	56.02	72.09	99.96

Table A.27: Release percentages for closed UXC case, 1.5 MW, 24 minutes (1440 s), rebounds limited to 100, medium extraction mode.

	1 μm	10 μm	100 μm
Release outside	0.	0.	0.
Release inside	36.96	21.69	0.02

Table A.28: Deposition percentages for closed UXC case, 1.5 MW, 24 minutes (1440 s), rebounds limited to 100, medium extraction mode.

	1 μm	10 μm	100 μm
Shaft	17.76	25.02	1.77
Floor	0.25	0.59	39.07
Cavern -	8.77	11.57	6.
Cavern +	1.9	3.45	0.27
Detector	1.56	3.32	44.21
Extraction outlet	22.83	21.26	5.43
Cavern ceiling	9.97	13.1	3.23
Total	63.04	78.31	99.98

Table A.29: Release percentages for closed UXC case, 1.5 MW, 37.5 minutes (2250 s), rebounds limited to 100.

	1 μm	10 μm	100 μm
Release outside	0.49	0.9	0.16
Release inside	39.23	21.53	0.

Table A.30: Deposition percentages for closed UXC case, 1.5 MW, 37.5 minutes (2250 s), rebounds limited to 100.

	1 μm	10 μm	100 μm
Shaft	30.03	37.72	2.09
Floor	0.23	1.35	41.55
Cavern -	11.57	14.12	6.19
Cavern +	3.76	5.01	0.29
Detector	2.79	5.35	46.89
Cavern ceiling	11.9	14.02	2.83
Total	60.28	77.57	99.84

Table A.31: Release percentages for UXC case open to the surface level, 1 MW, 31 minutes (1860 s), rebounds limited to 100.

	1 μm	10 μm	100 μm
Release > 98m	23.37	22.82	0.64
In air < 98m	21.99	9.61	0.

Table A.32: Deposition percentages for UXC case open to the surface level, 1 MW, 31 minutes (1860 s), rebounds limited to 100.

	1 μm	10 μm	100 μm
Shaft	25.6	31.62	2.1
Floor	1.14	2.39	41.24
Cavern -	10.03	12.01	4.9
Cavern +	2.39	3.35	0.12
Detector	2.57	4.19	48.75
Cavern ceiling	12.91	14.01	2.25
Total	54.64	67.57	99.36

Table A.33: Release percentages for UXC case open to the surface level, 1.5 MW, 24 minutes (1440 s), rebounds limited to 100.

	1 μm	10 μm	100 μm
Release > 98m	24.81	23.5	1.33
In air < 98m	21.9	10.74	0.01

Table A.34: Deposition percentages for UXC case open to the surface level, 1.5 MW, 24 minutes (1440 s), rebounds limited to 100.

	1 μm	10 μm	100 μm
Shaft	25.39	31.18	3.9
Floor	0.99	2.19	41.98
Cavern -	9.75	11.26	5.43
Cavern +	2.12	2.99	0.32
Detector	2.57	4.33	44.02
Cavern ceiling	12.47	13.81	3.01
Total	53.29	65.76	98.66

Table A.35: Release percentages for cavern case open to the surface level and neighboring cavern, 1 MW, 31 minutes (1860 s), rebounds limited to 100.

	1 μm	10 μm	100 μm
Release > 98m	55.17	51.67	23.41
In air < 98m	11.93	9.53	1.11

Table A.36: Deposition percentages for UXC case open to the surface level and neighboring cavern, 1 MW, 31 minutes (1860 s), rebounds limited to 100.

	1 μm	10 μm	100 μm
Shaft	29.53	34.54	32.62
Floor	0.05	0.14	27.03
Cavern -	0.09	0.13	0.
Cavern +	1.42	1.75	1.15
Detector	0.57	1.26	12.74
Cavern ceiling	1.24	0.98	1.94
Total	32.9	38.8	75.48

Table A.37: Release percentages for cavern case open to the surface level and neighboring cavern, 1.5 MW, 24 minutes (1440 s), rebounds limited to 100.

	1 μm	10 μm	100 μm
Release > 98m	53.24	51.46	27.24
In air < 98m	12.65	9.64	0.89

Table A.38: Deposition percentages for UXC case open to the surface level and neighboring cavern, 1.5 MW, 24 minutes (1440 s), rebounds limited to 100.

	1 μm	10 μm	100 μm
Shaft	30.41	34.91	36.12
Floor	0.03	0.11	21.5
Cavern -	0.03	0.22	0.01
Cavern +	2.05	2.14	2.12
Detector	0.35	0.63	8.49
Cavern ceiling	1.24	0.89	3.63
Total	34.11	38.9	71.87

Table A.39: Release percentages for cavern case open to the surface level and neighboring cavern, 0.5 MW, 40 minutes (2400 s), rebounds limited to 100.

	1 μm	10 μm	100 μm
Release > 98m	50.85	47.01	15.37
In air < 98m	11.29	8.35	0.4

Table A.40: Deposition percentages for UXC case open to the surface level and neighboring cavern, 0.5 MW, 40 minutes (2400 s), rebounds limited to 100.

	1 μm	10 μm	100 μm
Shaft	33.06	38.87	29.56
Floor	0.02	0.12	36.39
Cavern -	0.18	0.22	0.
Cavern +	1.8	2.43	1.21
Detector	1.05	1.94	15.4
Cavern ceiling	1.75	1.06	1.67
Total	37.86	44.64	84.23

Table A.41: Release percentages for UXC case open to the surface level, 1.5 MW, 24 minutes (1440 s), rebounds limited to 100, 50,000 particles.

	1 μm	10 μm	100 μm
Release > 98m	24.042	23.566	1.058
In air < 98m	24.796	11.152	0.022

Table A.42: Deposition percentages for UXC case open to the surface level, 1.5 MW, 24 minutes (1440 s), rebounds limited to 100, 50,000 particles.

	1 μm	10 μm	100 μm
Shaft	23.618	30.068	2.768
Floor	0.6	1.294	43.594
Cavern -	9.108	11.762	6.048
Cavern +	2.78	3.884	0.378
Detector	2.418	4.212	42.892
Cavern ceiling	12.638	14.062	3.24
Total	51.162	65.282	98.92
Total	51.162	65.282	98.92

Table A.43: Release percentages for UXC case open to the surface level, 1.5 MW, 24 minutes (1440 s), rebounds limited to 100, 100,000 particles.

	1 μm	10 μm	100 μm
Release > 98m	25.859	25.458	2.442
In air < 98m	23.764	10.913	0.052

Table A.44: Deposition percentages for UXC case open to the surface level, 1.5 MW, 24 minutes (1440 s), rebounds limited to 100, 100,000 particles.

	1 μm	10 μm	100 μm
Shaft	25.45	32.258	6.308
Floor	0.13	0.587	40.323
Cavern -	9.114	11.657	5.924
Cavern +	1.67	2.367	0.243
Detector	1.779	3.147	41.468
Cavern ceiling	12.234	13.613	3.24
Total	50.377	63.629	97.506

Table A.45: Release percentages for UXC case open to the surface level and neighboring cavern, 1.5 MW, 24 minutes (1440 s), rebounds limited to 100, aerodynamic diameters of 1, 5, 10, 50, 75 and 100 μm.

	1 μm	5 μm	10 μm	50 μm	75 μm	100 μm
Release > 98m	53.24	51.14	51.46	39.63	32.4	27.24
In air < 98m	12.65	10.66	9.64	7.02	3.22	0.89

Table A.46: Deposition percentages for UXC case open to the surface level and neighboring cavern, 1.5 MW, 24 minutes (1440 s), rebounds limited to 100, aerodynamic diameters of 1, 5, 10, 50, 75 and 100 μm.

	1 μm	5 μm	10 μm	50 μm	75 μm	100 μm
Shaft	30.41	35.14	34.91	39.75	37.9	36.12
Floor	0.03	0.14	0.11	5.53	14.56	21.5
Cavern -	0.03	0.13	0.22	0.01	0.	0.01
Cavern +	2.05	1.52	2.14	2.1	1.91	2.12
Detector	0.35	0.45	0.63	5.1	8.65	8.49
Cavern ceiling	1.24	0.82	0.89	0.86	1.36	3.63
Total	34.11	38.2	38.9	53.35	64.38	71.87

Table A.47: Release percentages for closed UXC case, 1 MW, 31 minutes (1860 s), standard local interaction particle sub model.

	1 μm	10 μm	100 μm
Release outside	0.01	0.02	0.03
Release inside	32.59	28.52	0.01

Table A.48: Deposition percentages for closed UXC case, 1 MW, 31 minutes (1860 s), standard local interaction particle sub model.

	1 μm	10 μm	100 μm
Shaft	28.7675	35.416	1.9665
Floor	0.0475	0.6825	42.0395
Cavern -	11.4705	13.1585	5.299
Cavern +	2.806	3.481	0.1285
Detector	2.151	4.201	46.2415
Cavern ceiling	21.8945	14.2355	4.231
Total	67.137	71.1745	99.906

Table A.49: Release percentages for closed UXC case, 1.5 MW, 24 minutes (1440 s), standard local interaction particle sub model.

	1 μm	10 μm	100 μm
Release outside	0.0075	0.0095	0.032
Release inside	38.914	32.9825	0.003

Table A.50: Deposition percentages for closed UXC case, 1.5 MW, 24 minutes (1440 s), standard local interaction particle sub model.

	1 μm	10 μm	100 μm
Shaft	28.1455	35.438	5.6935
Floor	0.012	0.307	43.1585
Cavern -	10.559	12.349	6.3105
Cavern +	1.1845	1.567	0.1225
Detector	1.344	2.877	38.2145
Cavern ceiling	19.583	14.267	6.338
Total	60.828	66.805	99.8375

Table A.51: Release percentages for UXC case open to the surface level, 1 MW, 31 minutes (1860 s), standard local interaction particle sub model.

	1 μm	10 μm	100 μm
Release > 98m	21.7235	23.414	0.6775
In air < 98m	14.889	8.3005	0.0265

Table A.52: Deposition percentages for UXC case open to the surface level, 1 MW, 31 minutes (1860 s), standard local interaction particle sub model..

	1 μm	10 μm	100 μm
Shaft	26.8655	30.8225	2.045
Floor	1.4965	2.8225	40.6045
Cavern -	11.169	12.3065	4.9215
Cavern +	3.194	3.6515	0.2095
Detector	2.6585	4.3105	47.5625
Cavern ceiling	18.004	14.372	3.953
Total	63.3875	68.2855	99.296

Table A.53: Release percentages for UXC case open to the surface level, 1.5 MW, 24 minutes (1440 s), standard local interaction particle sub model..

	1 μm	10 μm	100 μm
Release > 98m	22.103	23.2875	1.2705
In air < 98m	15.4575	9.0165	0.022

Table A.54: Deposition percentages for UXC case open to the surface level, 1.5 MW, 24 minutes (1440 s), standard local interaction particle sub model.

	1 μm	10 μm	100 μm
Shaft	27.9495	32.2075	4.6915
Floor	0.8355	1.9235	41.461
Cavern -	10.5675	12.0895	5.764
Cavern +	2.566	3.1055	0.308
Detector	2.303	3.789	41.0115
Cavern ceiling	18.218	14.581	5.4715
Total	62.4395	67.696	98.7075

Table A.55: Release percentages for cavern case open to the surface level and neighboring cavern, 1 MW, 31 minutes (1860 s), standard local interaction particle sub model.

	1 μm	10 μm	100 μm
Release > 98m	50.083	48.281	22.084
In air < 98m	9.3545	9.4465	0.553

Table A.56: Deposition percentages for UXC case open to the surface level and neighboring cavern, 1 MW, 31 minutes (1860 s), standard local interaction particle sub model.

	1 μm	10 μm	100 μm
Shaft	35.6645	37.516	36.056
Floor	0.0445	0.121	25.279
Cavern -	0.2315	0.269	0.
Cavern +	2.012	2.1105	1.4985
Detector	0.63	1.142	12.986
Cavern ceiling	1.98	1.114	1.5435
Total	40.5625	42.2725	77.363

Table A.57: Release percentages for cavern case open to the surface level and neighboring cavern, 1.5 MW, 24 minutes (1440 s), standard local interaction particle sub model.

	1 μm	10 μm	100 μm
Release > 98m	52.3615	51.1725	25.332
In air < 98m	8.534	8.765	1.203

Table A.58: Deposition percentages for UXC case open to the surface level and neighboring cavern, 1.5 MW, 24 minutes (1440 s), standard local interaction particle model.

	1 μm	10 μm	100 μm
Shaft	34.726	36.001	37.381
Floor	0.0375	0.109	21.301
Cavern -	0.1965	0.2205	0.0005
Cavern +	1.871	2.0555	2.323
Detector	0.2825	0.5655	10.9275
Cavern ceiling	1.991	1.111	1.532
Total	39.1045	40.0625	73.465

Appendix B

Mathematical model

Following the description on fire modeling in chapter 3, the used equations are described below. For general information on OpenFOAM[1] and fireFoam[2] the reader is referred to the appropriate guides [78, 79] and publications, cf. section 3.1. The solver itself is a modified version of the one available at FM Global's repository [93]. A support contract for OpenFOAM between CERN and Wikki Ltd., London, UK, provided additional external input. Information obtained from these exchanges will be referenced as personal communication.

Each model (case) is initialized by the fireFoam solver as follows:

1. Computational grid (mesh) data
2. Gravity direction and residuals
3. User-defined variable fields such as vector or scalar fields e.g. for thermal radiation and Lagrangian particles
4. User-defined initial and boundary conditions e.g. time step size, Courant number, velocities, temperatures etc.

After the first initialization of the case, its mesh, chosen sub models and user-defined conditions and functions, the solver carries out loops, in which the governing equations for mass, momentum and energy as well as the transport equation for each chemical specie is solved. Each set of equations is solved for every single cell in the following order:

1. Conservation of mass
2. Conservation of momentum
3. Transport of chemical species
4. Conservation of energy
5. Calculation of pressure

[1] Version used: OpenFOAM 2.2.x build 5cc33a23168577c9f91564fe6117f4ec1bde1348
[2] Version used: FM Global build 5f28904ffd7e82a9a55cb3f67fafb32f8f889d58

The last point from the list above is done by combining two commonly known and used techniques for pressure-velocity-coupling, see section B.10.1. This set of equations is solved until a user-defined criterion is reached e.g. a certain end time has been reached.

In the following sections the used governing equations for the conservation of mass, momentum and energy are discussed in detail. The transport of species is addressed, followed by an explanation of the different sub models. Only thesis-relevant sub models are discussed here. Afterwards a general description on the used boundary conditions and chosen numerical solution schemes is given. Pressure will be defined as follows. The total pressure, here denoted p is the sum of the ambient pressure and the hydrostatic pressure, cf. equation B.1. The latter is expressed as the product of $\rho g h$ in which ρ is the density of the gaseous phase, g is the gravity value in gravity direction and h is the height of the hydrostatic column [92].

$$p = p_0 + \rho g h \tag{B.1}$$

B.1 Conservation of mass

For each cell all relevant changes concerning mass due to fluid flow and sink or source terms is expressed as equation B.2. Herein $\bar{\rho}$ is the species averaged density, u_i is the velocity vector and t is the time, cf. section B.8.

$$\frac{\partial \bar{\rho} u_i}{\partial t} + \frac{\partial \bar{\rho} u_i}{\partial x_i} = 0 \tag{B.2}$$

B.2 Conservation of momentum

The conservation of momentum is calculated by solving the Navier-Stokes-equation. A derivation could be found elsewhere [95] and is not repeated here. Assuming that gravity is the only acting body force, the change of momentum in each cell can be expressed as equation B.3:

$$\frac{\partial \bar{\rho} u_i}{\partial t} + \frac{\partial \bar{\rho} u_i u_j}{\partial x_j} + \frac{\partial \tau_{ij}}{\partial x_j} = -\frac{\partial p}{\partial x_i} - g_i \frac{\partial \bar{\rho}}{\partial x_i} \tag{B.3}$$

Its first term on the left side represents the change of flow with time, the second the change of flow through cell surfaces and the third represents the viscous stress tensor τ_{ij} (eq. B.4). On the right hand side the change of pressure is followed by the gravity vector. Throughout this thesis, gravity is always applied in negative y-direction, i.e. $g_i \cdot \partial \bar{\rho} \cdot (\partial x_i)^{-1}$ simplifies to $\rho g_y h$. Herein g_y is the y-component of the gravity vector set to a value of 9.8, and h denotes the height of the model. Thus $\rho g_y h$ is the hydro-static

pressure part [92]. Equation (B.4) defines the viscous stress tensor τ_{ij} in which ν is the laminar part of the kinematic viscosity, while ν_t denotes the turbulent part.

$$\tau_{ij} = \left(\bar{\rho} \left(\nu + \nu_t \right) \left[\frac{\partial u_i}{\partial x_j} + \frac{\partial u_j}{\partial x_i} - \frac{2}{3} \frac{\partial u_k}{\partial x_k} \right] \right) \tag{B.4}$$

B.3 Conservation of energy

Changes in energy are computed according to equation B.5. On the left hand side, the first term denotes the change of energy with time, the second represents convective heat transfer and the third thermal diffusion.

The first term on the right hand side, the total derivatative of pressure, originates from the derivation of the energy equation rearranged to express energy transfer in terms of sensible enthalpy ([55], pages 46-50), the second source term adds the contribution or subtraction based on thermal radiation and the third term adds the increase or decrease in energy due to combustion. In the latter term, χ_{eff} is the combustion efficiency which defaults in this thesis to the value of one.

$$\frac{\partial \bar{\rho} h_s}{\partial t} + \frac{\partial \bar{\rho} u_j h_s}{\partial x_j} - \frac{\partial}{\partial x_j} \left(\frac{\partial \alpha_{\text{eff}} h_s}{\partial x_j} \right) = \frac{\mathrm{D}p}{\mathrm{D}t} + S_{\text{thermrad}} + \chi_{\text{eff}} S_{\text{comb}} \tag{B.5}$$

B.4 Transport of species

For each chemical specie's concentration and its transport is calculated by equation B.6. Therein, on the left hand side, the first term describes the change of specie with time, the second represents the convective mass transfer and the third the diffusive mass transfer. In this thesis only combustion is used to alter the virtual chemical species present (right hand side).

$$\frac{\partial \bar{\rho} Y_k}{\partial t} + \frac{\partial \bar{\rho} u_j Y_k}{\partial x_j} - \frac{\partial}{\partial x_j} \left(\frac{\partial D_{\text{eff}} Y_k}{\partial x_j} \right) = S_{\text{comb}} \tag{B.6}$$

B.5 Turbulence sub models

OpenFOAM includes libraries for LES and RANS based turbulence models. Out of manifold choices, in this thesis only the One-Equation-Eddy-Dissipation-Model for LES is used. The reader is refered to standard books on turbulence modeling for their derivation and further details etc. [88, 92, 94, 95].

B.5.1 One-Equation-Eddy-Dissipation-Model

This sub model is implemented according to the paper of Fureby et al. [111, 112]. It allows to calculate the missing viscosity parameter for the Navier-Stokes-Equation by using a single equation.

In eq. B.7 k is the turbulent kinetic energy, μ_{eff} the effective dynamic viscosity, c_ϵ and Δ are model constants. D and B are tensors, calculated according to equations B.8 and B.9. The expression $B : D$ denotes a double inner product [79]. In eq. B.8 I denotes the identity tensor that is equal to δ_{ij} (Kronecker Delta), ν_{SGS} is the sub-grid scale (SGS) kinematic viscosity.

$$\frac{\partial \bar{\rho} k}{\partial t} + \frac{\partial \bar{\rho} u_i k}{\partial x_i} - \frac{\partial}{\partial x_i}\left(\mu_{\text{eff}} \frac{\partial k}{\partial x_j}\right) = -\bar{\rho} D : B - c_\epsilon \bar{\rho} k^{\frac{3}{2}} \frac{1}{\Delta} \tag{B.7}$$

$$B = \frac{2}{3} k \, \mathrm{I} - 2 \, \nu_{\text{SGS}} \, \mathrm{dev}\,(D) \tag{B.8}$$

$$D = \mathrm{symm}(\mathrm{grad}(u_i)) \tag{B.9}$$

The kinematic and dynamic viscosity for the sub-grid scale part and the effective dynamic viscosity μ_{eff}, that is the sum of its turbulent and laminar part, are calculated according to equations B.10 and B.11. Multiplying the turbulent kinematic viscosity ν_t with the gas phase density $\bar{\rho}$ gives the turbulent dynamic viscosity μ_t. The laminar dynamic viscosity μ is calculated according to eq. B.54, cf. section B.9.1.

$$\nu_{\text{SGS}} = \nu_t = c_k \bar{\rho} \sqrt{k} \tag{B.10}$$

$$\mu_{\text{eff}} = \mu_{\text{SGS}} + \mu = \mu_t + \mu \tag{B.11}$$

Further the LES Δ variable is expressed as shown in eq. B.12, where c_Δ is a constant set by the user and V denotes the Volume.

$$\Delta = \frac{1}{3} c_\Delta V \tag{B.12}$$

The dynamic sub-grid scale viscosity μ_{SGS} divided by the turbulent Prandtl number

$\mathrm{Pr_t}$ results in the thermal diffusivity α_{SGS}, cf. eq. B.13.

$$\alpha_{\mathrm{SGS}} = \alpha_{\mathrm{t}} = \frac{\mu_{\mathrm{t}}}{\mathrm{Pr_t}} \tag{B.13}$$

The turbulent Prandtl number $\mathrm{Pr_t}$ and the constant c_ϵ are user-defined values. The internal OpenFOAM default values are $\mathrm{Pr_t} = 1$ and $\mathrm{c}_\epsilon = 1.048$.

B.6 Combustion sub models

In this thesis only the infinite fast chemistry approach is used to represent combustion. OpenFOAM's combustion framework is discussed below to complement the chosen combustion sub model.

All combustion models follow one or multiple reaction equations. An example is the ideal complete combustion of methane as shown in equation B.14. The reader is referred to [55] for an example of different hydrocarbon reactions as would occur in reality for this kind of fuel.

$$1\,\mathrm{CH_4} + 2\,\mathrm{O_2} + 2 \cdot 3.76\,\mathrm{N_2} \rightarrow 1\,\mathrm{CO_2} + 2\,\mathrm{H_2O} + 2 \cdot 3.76\,\mathrm{N_2} \tag{B.14}$$

One can generalize this towards a uniform reaction equation, valid for all hydrocarbons, cf. equation B.15. Herein f is a placeholder for "fuel" e.g. methane, propane or butane, ν_{i}' denotes the required number of moles for a reactant i and ν_{i}'' the resulting number of moles for a product i.

$$\nu_{\mathrm{f}}'\,\mathrm{f} + \nu_{\mathrm{O_2}}'\,\mathrm{O_2} + \nu_{\mathrm{N_2}}'\,\mathrm{N_2} \rightarrow \nu_{\mathrm{CO_2}}''\,\mathrm{CO_2} + \nu_{\mathrm{H_2O}}''\,\mathrm{H_2O} + \nu_{\mathrm{N_2}}''\,\mathrm{N_2} + \Delta H_c \tag{B.15}$$

Since combustion is an oxidation process, an oxidizer must be present. Here, only the combustion of gaseous hydrocarbons is described. For this case a oxygen-fuel ratio $\mathrm{s_{O_2}}$ as well as an air-fuel ratio $\mathrm{s_{air}}$ can be calculated, cf. equations B.16 and B.17. The former is the amount of pure oxygen necessary to fulfill the idealized reaction, the latter is the amount of air that would be required. If these values are derived from an ideal reaction, these values are also named stoichiometric oxygen-fuel $s_{\mathrm{O_2}}$ and stoichiometric air-fuel ratio s_{air}. For a certain chemical specie i ν_{i}' represents the number of reactant moles and M_i its molar mass.

$$s_{\mathrm{O_2}} = \frac{\nu_{\mathrm{O_2}}' M_{\mathrm{O_2}}}{\nu_{\mathrm{f}}' M_{\mathrm{f}}} \tag{B.16}$$

$$s_{\text{air}} = \frac{\nu'_{\text{O}_2} M_{\text{O}_2} + \nu'_{\text{N}_2} M_{\text{N}_2}}{\nu'_{\text{f}} M_{\text{f}}} \tag{B.17}$$

Nitrogen is used as an inert species. An inert specie is often neglected in terms of transport to save the computational effort of calculating it separately. However, as follows from eq. B.16 and B.17 s_{O_2} and s_{air} will have the same value in this case. To obtain different values for s_{O_2} and s_{air}, one has to include the inert specie in the reaction equation.

Next, the total number of product moles n_{prod} is calculated from the right hand side of the reaction equation, here denoted as n_{prod}, cf. eq. B.18:

$$n_{\text{prod}} = \sum_{i=1}^{n} \nu''_i \tag{B.18}$$

Herein is n the number of products. Then the total number of product moles is used to compute the mole fraction X_i of all products by dividing the number of moles of each single product by the total number of product moles according to eq. B.19

$$X_i = \frac{\nu''_i}{n_{\text{prod}}} \tag{B.19}$$

Next the sum of molecular mass of products M_{prod} is derived by multiplying the mole fraction X_i with the molecular mass M_i for each product (eq. B.20).

$$M_{\text{prod}} = \sum_{i=1}^{n} X_i M_i \tag{B.20}$$

Using the mole fraction X_i of each product, the related product mass fractions $\text{Y}_{\text{prod},i}$, assuming stoichiometric combustion, are derived according to equation B.21.

$$Y_{\text{prod},i} = \frac{M_i}{M_{\text{prod}}} X_i \tag{B.21}$$

For further calculations a mass-based reaction is assumed and mass-based stoichiometric coefficients ν_i are derived for each chemical specie, cf. equation B.22.

$$\nu_i = \frac{\nu^*_i M_i}{\nu'_{\text{f}} M_{\text{f}}} \quad \text{with} \quad \nu^*_i = \nu'_i \text{ or } \nu''_i \tag{B.22}$$

Exothermic reactions produce more energy than would be necessary for their completion. The amount of energy produced in addition is the heat of combustion, ΔH_c. It is based on the chemical enthalpy ΔH_c of all involved species and is expressed as the difference between the sums of all product enthalpies $\Delta H_{c,P}$ and all reactant enthalpies $\Delta H_{c,R}$, cf. eq. B.23:

$$\Delta H_c = \sum \nu_{i,P} \Delta H_{c,P} - \sum \nu_{i,R} \Delta H_{c,R} \tag{B.23}$$

B.6.1 Infinite fast chemistry

A simple approach to describe the combustion of gas mixed with an oxidizer is the infinitely fast chemistry, also named "mixed is burnt". Here, fuel and oxidizer will react immediately without relying on reaction rates or chemical or turbulent time scales. This mixture rate (fuel rate) R_f is described in eq. B.24 as:

$$R_f = \nu'_f \frac{\bar{\rho}}{\tau} \min\left(Y_f, \frac{Y_{O_2}}{s_{air}}\right) \tag{B.24}$$

Here, τ is denoting a user-defined relaxation constant. Multiplying the fuel rate R_f with the heat of combustion ΔH_c and the fuel mass fraction Y_{fuel} results in the combustion source term S_{comb}, cf. eq. B.25;

$$S_{combustion} = \Delta H_c R_f Y_f \tag{B.25}$$

B.7 Thermal radiation sub models

Energy transport due to thermal radiation is one of the three mechanisms usually accounted for in heat transfer (besides convection and conduction). In OpenFOAM it is represented by a source term, provided for the energy transport equation, see section B.3. It is expressed in equation B.26, where R_u and R_p are source term components, T is the temperature, h the enthalpy and c_p is the specific heat capacity of the fluid that interacts with thermal radiation.

$$S_{thermrad} = R_u - \left(4 R_p T^3 \frac{1}{c_p}\right) h - R_p T^3 \left(T - 4h \frac{1}{c_p}\right) \tag{B.26}$$

At this level the source term does not take into account the radiation sub model such as the finite-volume discrete-ordinance-model (fvDOM) or the P1 model. One or none of these must be choosen by the user, defining also several model dependent parameters, see sections B.7.1 and B.7.2. In addition, an absorption and emission sub model has to be selected.

B.7.1 fvDOM

As mentioned above, two source terms are required for the general thermal radiation source term in eq. B.26. The first one, R_u is expressed as sum of the incident radiation G multiplied with the absorption coefficient a minus the emittance E, cf. eq. B.27.

$$R_u = aG - E \tag{B.27}$$

The incident radiation G is calculated by integrating the radiation intensity I over the solid angle Ω, i.e. here in terms of the fvDOM model summing up all products of i radiation intensities I_i and solid angles Ω_i, cf. eq. B.28 (taken from [113]).

$$G = \int_{4\pi} I \, d\Omega = \sum_i I_i \Omega_i \tag{B.28}$$

Each radiation intensity I_i following an average direction vector d_i is calculated following eq. B.29 (adapted from [113]). The vector S_f is a face area vector [79].

$$\nabla \left((d_i S_f) \, I_i \right) + a \Omega_i I_i = \frac{\Omega}{\pi} \left(a I_b + \frac{E_{Cont}}{4} \right) \tag{B.29}$$

The black body emission part named I_b in eq. B.29 is calculated from eq. B.30. Therein σ denotes the Stefan-Boltzmann constant.

$$I_b = \sigma T^4 \tag{B.30}$$

The solid angle Ω_i is depending on the angles Θ and Φ which are set by the user. Every solid angle Ω_i is derived from an individual angle Θ for each ray, cf. eq. B.31.

$$\Omega_i = 2 \sin\Theta_i \sin\left(\frac{\Delta\Theta}{2} \right) \Delta\Phi \tag{B.31}$$

The discrete ordinate model is based on replacing the continuous thermal radiation by discrete rays that are easier to calculate. First, the total number of rays is calculated by eq. B.32 in which n_Θ and n_Φ are the former mentioned user defined numbers. This is followed by computing a pair of angles, $\Delta\Phi, \Delta\Theta$ from the initial values set by the user, cf. eq. B.33 and B.34.

$$n_{ray} = 4 n_\Phi n_\Theta \tag{B.32}$$

$$\Delta\Phi = \frac{\pi}{2n_\Phi} \tag{B.33}$$

$$\Delta\Theta = \frac{\pi}{n_\Theta} \tag{B.34}$$

With these values rays are initialized in form of different value sets for each ray by using two "for" loops. The loops are constrained by the user given numbers for n_Θ and n_Φ. Inside the loops the two angles Θ and Φ are calculated for each ray, cf. equations B.35 and B.36. Please note that n and m in equations B.35 and B.36 are the incremental variables of the loops.

$$\Theta_i = (2n - 1)\frac{\Delta\Theta}{2} \tag{B.35}$$

$$\Phi_i = (2m - 1)\frac{\Delta\Phi}{2} \tag{B.36}$$

Heat produced by a flame is transported to the surrounding environment by convection and thermal radiation. Depending on the material composition that is burning, i.e. the mixture of pyrolysates, the percentage of heat emitted by thermal radiation could vary. To account for the influence of heat loss (due to thermal radiation) on the heat release rate $\dot{Q}$ a fraction value E_{HRR} has to be provided by the user. Mathematically it is expressed as in eq. B.37

$$E = E_{HRR}\dot{Q} \tag{B.37}$$

The second source term R_p depends only on the absorption coefficient a, cf. equation B.38 .

$$R_p = 4a\sigma \tag{B.38}$$

B.7.2 P1

Opposite to the fvDOM model in section B.7.1 above, the P1-Model does not discretize the thermal radiation representing sphere into different rays. Following from the source term (eq. B.26), the component R_u is calculated by equation B.39. The necessary inci-

dent radiation G is then calculated according to equation B.40.

$$\mathrm{R_u} = aG - 4E \tag{B.39}$$

$$G = \int_{4\pi} I \, \mathrm{d}\Omega \tag{B.40}$$

As I is integrated over Ω, [113], without following individual rays as in the fvDOM sub model, only one additional equation for G has to be solved, cf. equation B.41 [113]. Therein is a the absorption coefficient, G the incident radiation, σ is the Stefan-Boltzmann constant and T the temperature.

$$\frac{1}{3a}\nabla^2 G - a\mathrm{G} = -4\left(\sigma T_g^4\right) \tag{B.41}$$

B.7.3 Absorption emission models

In this thesis only two absorption-emission-models are used together with the fvDOM and P1 thermal radiation sub models. For more information the reader is referred to the book of Modest [85] or recent publications with respect to fire modeling e.g. from Lautenberger et al. [114, 115]. Here, the constant absorption-emission model was combined with the P1 thermal radiation sub model and the Grey-Mean-Absorption-Emission model with the fvDOM thermal radiation sub model.

B.7.3.1 Constant-Absorption-Emission

The constant-absorption-emission model allows to set constant values for the absorption coefficient a, the emission coefficient e and the emittance E.

B.7.3.2 Grey-Mean-Absorption-Emission

If the thermal radiation sub model is used with a grey-mean-absorption-emission model to account for optically thin gases, the absorption coefficient a is calculated for every cell according to the mixture of species. In eq. B.42 p is the pressure in a cell, p_{atm} is a conversion factor with a constant value of $1.10325 \cdot 10^5$ Pa·bar^{-1} and b_{ij} are polynomial coefficients, different for each species.

$$a = \frac{p}{p_{\mathrm{atm}}} \sum_i X_i \left(\mathrm{b}_{0,i} + \mathrm{b}_{1,i} T^{\mathrm{s}_i} + \mathrm{b}_{2,i} T^{2\mathrm{s}_i} + \mathrm{b}_{3,i} T^{3\mathrm{s}_i} + \mathrm{b}_{4,i} T^{4\mathrm{s}_i} + \mathrm{b}_{5,i} T^{5\mathrm{s}_i}\right) \tag{B.42}$$

These polynomial coefficients are given for T or for T^{-1} and can be found on the kinetic part of NIST's web site [116]. Therefore the parameter s in eq. (B.42) acts as switch ($s_i = \pm 1$) to obtain a correct absorption factor.

B.8 Lagrangian parcel sub model

OpenFOAM's Lagrangian particles, are injected at a certain position into a gaseous flow originating from a thermal plume. Only two forces have been considered to act on these particles: gravity and drag.

The following equations have been taken from Christ, representing the Lagrangian framework used [113]. Each parcels' velocity is computed according to equation B.43. Herein x_i is the position and $u_{i,\mathrm{p}}$ the velocity of the parcel in question.

$$\frac{\partial x_i}{\partial t} = u_{i,\mathrm{p}} \tag{B.43}$$

A change in particle velocity is depending on the sum of forces acting on it, i.e. $\Sigma_i F_i$. They are either related to the surrounding gas phase ($\Sigma_j S_{F,j}$) or independent ($\Sigma_k F_k$), cf. eq. B.44 and B.45. In eq. B.44 m_p is the mass of a parcel.

$$m_\mathrm{p} \frac{\partial u_{i,\mathrm{p}}}{\partial t} = \Sigma_i F_i \tag{B.44}$$

$$\Sigma_i F_i = \Sigma_j S_{F,j} \left(u_{i,\mathrm{g}} - u_{i,\mathrm{p}} \right) + \Sigma_k F_k \tag{B.45}$$

Sphere drag is calculated according to equation B.46. Therein S_sph denotes the source term for sphere drag, μ_eff is the effective gas phase viscosity, C_d is the drag coefficient, $\mathrm{Re_p}$ is the particle Reynolds number, ρ_p and d_p are the parcel density and aerodynamic diameter (both constant).

$$\Sigma_j S_{F,j} = S_\mathrm{sph} = \frac{0.75 m_\mathrm{p} \mu_\mathrm{eff} \mathrm{C_d Re_p}}{\rho_\mathrm{p} d_\mathrm{p}^2} \tag{B.46}$$

The drag coefficient multiplied with the particle Reynolds number $\mathrm{C_d Re_p}$ depends on the Reynolds number for a parcel, cf. eq. B.47.

$$\mathrm{C_d Re_p} = \begin{cases} 0.424\,\mathrm{Re_p}, & \text{if } \mathrm{Re_p} > 1000 \\ 24\left(1 + \frac{1}{6\mathrm{Re_p}^{0.66}}\right), & \text{if } \mathrm{Re_p} < 1000 \end{cases} \tag{B.47}$$

The Reynolds number noted above is taking into account the difference between parcel velocity and fluid (gas) phase velocity, cf. equation B.48 [80].

$$\mathrm{Re}_\mathrm{p} = \frac{\rho_\mathrm{g} \left| u_{i,\mathrm{g}} - u_{i,\mathrm{p}} \right| d_\mathrm{p}}{\mu_\mathrm{eff}} \tag{B.48}$$

Gravity is acting on a parcel as defined by the product of its mass m_p and the gravity vector g_i, cf. eq. B.49.

$$\Sigma_k F_k = m_\mathrm{p} \mathrm{g}_i \tag{B.49}$$

B.9 Equations of state

To close the equations stated above, several equations of state are discussed below. Most of the following information has been retrieved from Christ [113]. Gas phase density ρ_g is calculated following equation B.50. Therein $\overline{M}$ is the weighted molar mass and $\mathfrak{R}$ is the universal gas constant.

$$\rho_\mathrm{g} = \frac{p\overline{M}}{\mathfrak{R}T} \tag{B.50}$$

To take into accout the dependency of the specific heat capacity c_p on temperature, a polynomial approach is used to calculate the enthalpy h for each specie. Then, a cell-wide c_p is computed by summing up the individual heat capacity values times the molar fraction of each species. In equation B.51 h denotes enthalpy and $a_{1..6}$ are model constants. This approach is based on thermochemical tables [116].

$$\frac{h}{\mathfrak{R}T} = a_1 + a_2 \left(\frac{T}{1\,\mathrm{K}} \right) + a_3 \left(\frac{T}{1\,\mathrm{K}} \right)^2 + a_4 \left(\frac{T}{1\,\mathrm{K}} \right)^3 + a_5 \left(\frac{T}{1\,\mathrm{K}} \right)^4 + a_6 \left(\frac{T}{1\,\mathrm{K}} \right)^{-1} \tag{B.51}$$

Using the correlation $h_\mathrm{s}(T) = h(T) - h(T_\mathrm{ref})$ one can calculate the sensible enthalpy h_s [113]. To obtain the specific heat capacity c_p equation B.52 is used, relying on the same model constants $a_{1..5}$.

$$\frac{c_p}{\mathfrak{R}} = a_1 + a_2 \left(\frac{T}{1\,\mathrm{K}} \right) + a_3 \left(\frac{T}{1\,\mathrm{K}} \right)^2 + a_4 \left(\frac{T}{1\,\mathrm{K}} \right)^3 + a_5 \left(\frac{T}{1\,\mathrm{K}} \right)^4 \tag{B.52}$$

For each cell a sensible enthalpy h_s is calculated. Together with the temperature-depending specific heat capacity c_p, it allows to compute a new temperature cf. equation

B.53.

$$h_\mathrm{s} = \int_{T_\mathrm{ref}}^{T} c_p \,\mathrm{d}T \tag{B.53}$$

B.9.1 Transport coefficients

The transport coefficients for thermal diffusivity α and dynamic viscosity μ have been taken from the publications of Sutherland [117] and Poling et al. [118], respectively. For each cell the dynamic viscosity μ is calculated according to equation B.54 with the initial or calculated temperature T and $A_\mathrm{s} = 1.67212 \cdot 10^{-6}$ s^{-1} and $T_\mathrm{s} = 170.672$ K being model constants.

$$\mu = A_\mathrm{s} \frac{\sqrt{T}}{1 + \frac{T_\mathrm{s}}{T}} \tag{B.54}$$

As for thermal diffusivity equation B.55 is used, in which c_v is the specific heat capacity at constant volume; derived from the relation $c_v = c_p - \mathfrak{R}$.

$$\alpha = \mu \frac{c_v}{c_p} \left(1.22 + 1.77 \frac{\mathfrak{R}}{c_v}\right) \tag{B.55}$$

Similar to eq. B.11, the effective thermal diffusivity and effective species diffusion is derived, cf. equations B.56 and B.58. The laminar and turbulent mass diffusion coefficients are derived "from the analogy between momentum and mass transfer" [113], cf. equation B.57.

$$\alpha_\mathrm{eff} = \alpha_\mathrm{SGS} + \alpha = \alpha_\mathrm{t} + \alpha \tag{B.56}$$

$$\mathrm{Sc} = \frac{\mu}{\rho D} \tag{B.57}$$

If not otherwise noted, in all simulations $\mathrm{Sc}=\mathrm{Sc}_\mathrm{t}=1$ is assumed. Due to this constraint, the effective diffusion coefficient equals the effective kinematic viscosity ν_eff, cf. B.58.

$$D_\mathrm{eff} = D_\mathrm{t} + D = \nu_\mathrm{eff} \tag{B.58}$$

B.10 Initial and boundary conditions

To be able to start any numerical solver, a set of initial conditions has to be provided by the user. In OpenFOAM this is done by creating a text file with conditions for each variable in a dedicated folder. Each file follows the same structure:

1. Dimensions
2. Initial value
3. List of boundaries and their individual conditions

Table B.1 provides exemplary a full set of initial conditions for a model of the CMS underground experimental cavern open to the neighboring cavern and to the surface level. Initial conditions are set uniformly throughout the model geometry.

Table B.1: Initial conditions for a model of the CMS experimental cavern open to the the surface level and neighboring cavern.

Variable	Value	Unit
T	293	K
p	102,479	Pa
u_i	(0 0 0)	$\mathrm{m{\cdot}s^{-1}}$
CH_4	0	-
CO_2	0	-
H_2O	0	-
O_2	0.23301	-
N_2	0.76699	-
α_t	0	$\mathrm{kg{\cdot}(m{\cdot}s)^{-1}}$
μ_t	0	$\mathrm{kg{\cdot}(m{\cdot}s)^{-1}}$
k	10^{-4}	$\mathrm{m^2{\cdot}s^{-2}}$

At the boundaries of the computational grid, conditions have to be applied for every single user-defined variable e.g. temperature, pressure or velocity. Depending on the variable different conditions might be used. In the following parts all conditions used in this thesis work are explained in detail. Beside the mathematical formulas code listings provide the exact setup of each condition.

Table B.2 gives an example for three groups of boundary conditions: wall, burner inlet and ambient. In a full model of the CMS experimental cavern about 40 different surfaces are defined as wall type. Only two patches connect the internal volume of the computational grid to the ambient environment, i.e. allow exchange of gaseous fluid into and out of the computational domain. Similarities exist also between the boundary condition configuration given for a burner inlet in table B.2 and a ventilation extraction outlet. Here, only the velocity vector changes.

Table B.2: Boundary conditions for a model of the CMS underground experimental cavern open to the surface level and neighboring cavern.

Surface	Variable	Condition	Value	Unit
Wall	T	zeroGradient	-	-
	p	buoyantPressure	-	-
	u_i	fixedValue	(0 0 0)	$\mathrm{m{\cdot}s^{-1}}$
	CH_4	zeroGradient	-	-
	CO_2	zeroGradient	-	-
	H_2O	zeroGradient	-	-
	O_2	zeroGradient	-	-
	N_2	zeroGradient	-	-
	α_t	compressible::alphatWallFunction	-	-
	μ_t	mutUSpaldingWallFunction	-	-
	k	compressible::kqRWallFunction	-	-
Burner inlet	T	fixedValue	293	K
	p	buoyantPressure	-	-
	u_i	fixedValue	(0 0.28 0)	$\mathrm{m{\cdot}s^{-1}}$
	CH_4	totalFlowRateAdvectiveDiffusive	1	-
	CO_2	totalFlowRateAdvectiveDiffusive	0	-
	H_2O	totalFlowRateAdvectiveDiffusive	0	-
	O_2	totalFlowRateAdvectiveDiffusive	0	-
	N_2	totalFlowRateAdvectiveDiffusive	0	-
	α_t	calculated	-	-
	μ_t	calculated	-	-
	k	zeroGradient	-	-
Ambient	T	inletOutlet	293	K
	p	totalPressure	102,479	Pa
	u_i	pressureInletOutletVelocity	-	-
	CH_4	inletOutlet	0	-
	CO_2	inletOutlet	0	-
	H_2O	inletOutlet	0	-
	O_2	inletOutlet	0.23	-
	N_2	inletOutlet	0.77	-
	α_t	zeroGradient	-	-
	μ_t	zeroGradient	-	-
	k	zeroGradient	-	-

B.10.1 Pressure and Velocity

To solve for pressure and velocity and then later for all other parameters, the simulations carried out in this thesis used pressure implicit splitting of operators (PISO), initially

developed by Issa [119]. It follows the semi-implicit method for pressure-linked equations (SIMPLE) by Patankar [120], with some enhancements. Detailed explanations and flow charts can be found in [90, 92, 94, 95, 113] and are not repeated here. Only certain combinations of boundary conditions for $p - \rho gh$ and u_i are used:

- buoyantPressure for $p - \rho gh$ and fixedValue for u_i
- totalPressure for $p - \rho gh$ and pressureInletOutletVelocity for u_i

For the chosen geometry about 98 m difference between the surface and the floor level of the experimental cavern has to be taken into account. Assuming 101,325 Pa at the surface results in about 102,479 Pa at floor level using ambient conditions for air cf. equation B.1. This value has been used to set pressure boundary conditions.

As noted at the beginning of appendix B, the pressure p is split into two parts to simplify solving the momentum equation, cf. eq. B.1. For each case two pressure-related boundary conditions exist, one for p and one for $p - \rho gh$. The latter represents the pressure without the hydrodynamic part. Only for $p - \rho gh$ boundary conditions are actually set by the user, as this pressure is used for iteration. Therefore, the setting for the pressure p is always set to *calculated*, cf. listing B.1.

```
floor
{
type            calculated;
value           uniform 102479;
}
```

Listing B.1: Boundary conditions for pressure

For walls, the pressure gradient for $p - \rho gh$ at a wall is derived for buoyant flow according to equation B.59 [121]:

$$\nabla p = -\nabla \perp (\rho)\,(g \cdot h) \tag{B.59}$$

in which ρ is the density, g is the acceleration due to gravity and h is the patch face center. Equally for walls, the wall velocity vector $u_i|_{\mathrm{w}}$ is defined as zero vector, cf. eq. B.60:

$$u_i|_{\mathrm{w}} = (0\,0\,0)^{\mathsf{T}} \tag{B.60}$$

Listings B.3 and B.2 show the applications of equations B.59 and B.60 in OpenFOAM.

```
floor
{
type                buoyantPressure;
value               uniform 102479;
}
```

Listing B.2: Buoyant pressure boundary condition for $p - \rho g h$

```
floor
{
type                fixedValue;
value               uniform (0 0 0);
}
```

Listing B.3: Fixed value boundary condition for velocity

At cross-sections open to the ambient, a total pressure condition is applied. In equation B.61 p_T is the total pressure and p_0 a user-defined ambient pressure. To calculate p_T the velocity u_i must be known. Its value is derived by applying a direction-dependent boundary condition (pressureInletOutletVelocity). For outflow a zero gradient condition is applied, i.e. the second last velocity vector is copied to the wall cell. If an inflow occurs, the wall velocity vector is based on the patch-face normal value of the next internal cell [121].

$$p_T = p_0 + 0.5\rho|u_i|^2 \tag{B.61}$$

Listings B.4 and B.5 show the OpenFOAM equivalent of the boundary treatment for cross-sections open to the ambient discussed above, such as the connection of the CMS experimental cavern to its neighboring cavern (denoted TX56 in the listings below). Based on the velocity value derived from the flow direction, the total pressure is calculated according to equation B.61.

```
TX56
{
type          pressureInletOutletVelocity;
value         uniform (0 0 0);
}
```

Listing B.4: Direction-depending boundary condition for velocity

```
TX56
{
type          totalPressure;
rho           rho;
psi           none;
gamma         0;
p0            uniform 102479;
value         uniform 102479;
}
```

Listing B.5: Total pressure boundary condition for $p - \rho g h$

B.10.2 Temperature

For temperature three different conditions are used. Wall surfaces are treated by a zero gradient condition, cf. listing B.6. While mathematically, the gradient between the temperature in the second last cell $T_{\text{w-1}}$ in front of a wall and the temperature T_{w} in the last cell (wall cell) is set to zero, cf. equation B.62, this is easily solved on the programming side by simply copying the second last temperature value to the wall cell.

```
floor
{
type            zeroGradient;
}
```

Listing B.6: Wall boundary condition for temperature T

$$\left.\frac{\partial T}{\partial x_i}\right|_{\text{w,w-1}} = 0 \tag{B.62}$$

A constant inflow temperature is always kept at the burner inlet (293 K) by applying a fixed value condition similar to the one for velocity at a wall as discussed above for velocity (section B.10.1), cf. listing B.7.

```
inlet
{
type                fixedValue;
value               uniform 293;
}
```

Listing B.7: Fuel inlet boundary condition for temperature T

Cross-sections open to the ambient are conditioned to let go out-flowing fluid by applying a zero gradient condition. In-flowing fluid, here fresh air is assumed, is predefined by temperature and oxygen and nitrogen mass fractions. Listing B.8 shows such a condition, with a user-defined inflow temperature of 293 K.

```
TX56
{
type            inletOutlet;
inletValue      uniform 293;
value           uniform 293;
}
```

Listing B.8: Fuel inlet boundary condition for temperature T

B.10.3 Concentrations of chemical reactants and products

Concentrations of gaseous chemical species in the gas phase are computed by multiplying the individual mass fractions Y_i with the gas density ρ_g. For each specie boundary conditions are defined for its individual mass fraction.

All walls are treated as impermeable, thus all mass fractions employ a zero gradient condition such as for temperature, cf. listing B.6. Cross-sections used for the ventilation extraction mode discussed in section 5.1.1 use a fixed value condition set to zero to avoid an unrealistic entrainment of combustion products (here CO_2 and H_2O only). For openings to the ambient, the mass fractions for O_2 and N_2 are defined by using the inletOutlet condition explained in section B.10.2 above.

To neglect the diffusion term in eq. B.6 between the mass fraction of fuel for the burner $Y_{\text{fuel,b}}$ and the mass fraction $Y_{\text{fuel,b-1}}$ in each cell around the burner inlet, a dedicated boundary condition sets the corresponding gradient to zero, cf. equation B.63 and listing B.9.

$$\left.\frac{\partial D_{\text{eff}} Y_{\text{fuel}}}{\partial x_j}\right|_{\text{b,b-1}} = 0 \tag{B.63}$$

```
inlet
{
type            totalFlowRateAdvectiveDiffusive;
massFluxFraction 1;
phi             phi;
rho             rho;
value           uniform 1;
}
```

Listing B.9: Burner boundary condition for the mass fraction of fuel

B.10.4 Turbulent kinetic energy, viscosity and diffusivity

Wall functions have been used for the turbulent kinetic energy k, dynamic viscosity μ_t and thermal diffusivity α. For the turbulent kinetic energy k the wall function shown in

listing B.10 enforces a zero gradient condition at a wall [121].

```
floor
{
type            compressible::kqRWallFunction;
value           uniform 0.1;
}
```

Listing B.10: Boundary conditions: k

The wall values for the sub-grid scale thermal diffusivity in listing B.11 are calculated following equation B.13, i.e. are depending on the dynamic sub-grid scale viscosity μ_t and the turbulent Prandtl number Pr_t. From $\mathrm{Pr}_t = 1$ follows $\alpha_\mathrm{t} = \mu_t$. Thus at all walls the same values are used for dynamic sub-grid scale viscosity and thermal sub-grid scale diffusivity assuming isotropic conditions.

```
floor
{
type            compressible::alphatWallFunction;
mut             muSgs;
value           uniform 0;
}
```

Listing B.11: Boundary conditions: α_SGS

To obtain a continous viscosity profile next to a wall Spaldings's law is applied [89, 121], cf. equation B.64. A non-dimensional position y^+ is calculated based on a non-dimensional velocity u^+, a wall function constant $E = 9.8$ and the von Karman constant $\kappa = 0.41$. Both constants are dimensionless. For each wall surface the corresponding condition is applied, cf. listing B.12.

$$y^+ = u^+ + \frac{1}{E}\left[\exp(\kappa u^+) - 1 - \kappa u^+ - 0.5(\kappa u^+)^2 - \frac{1}{6}(\kappa u^+)^3\right] \tag{B.64}$$

```
floor
{
type            mutUSpaldingWallFunction;
value           uniform 0;
}
```

Listing B.12: Boundary conditions: μ_SGS

B.10.5 Incident radiation and radiative intensity

All cases using a thermal radiation sub model have been run with boundary conditions for the incident radiation G and the radiative intensity I , cf. listings B.13 and B.14.

```
floor
{
type              MarshakRadiation;
T                 T;
emissivityMode    lookup;
emissivity        uniform 1;
value             uniform 0;
}
```

Listing B.13: Boundary conditions: G

```
floor
{
type              greyDiffusiveRadiation;
T                 T;
emissivityMode    lookup;
emissivity        uniform 1;
value             uniform 0;
}
```

Listing B.14: Boundary conditions: I